**Università degli Studi di Genova**

DIPARTIMENTO DI INFORMATICA, BIOINGEGNERIA, ROBOTICA E INGEGNERIA DEI SISTEMI
ISTITUTO ITALIANO DI TECNOLOGIA
Doctor of Philosophy in Bioengineering and Robotics
Curriculum: Bionanotechnology

PhD Thesis

# Vibrational Strong Coupling in THz Plasmonic Nanocavities

Candidate:
**Andrea Cerea**

Tutors:
**Dr. Andrea Toma**
**Dr. Francesco De Angelis**

Reviewers:
**Prof. Stefano Lupi**
**Prof. Emanuele Orgiu**

**XXX Ciclo**
**Anno Accademico 2014–2017**

# Index

# Introduction

Since the early stages of scientific research the investigation of how light and matter interact has been both an intrinsic and a non-trivial issue. Across the years, scientists have succeeded in the explanation of many fundamental phenomena and new discoveries have raised a plethora of questions, most of which still remain unanswered. Nowadays, the study of the basic mechanisms of light-matter interaction is an interdisciplinary topic addressed in the fields of optical and atomic physics, condensed matter physics, optoelectronics, communication, molecular biology and medicine. Interaction occurs across a frequency range that spans many orders of magnitude, from the few tens of Hz of deep earth and sea communications to the hundreds of petaHz of X-ray imaging, and over length scales that ranges from thousands of meters to few hundreds picometers.

In this vast framework, the present study focuses with particular attention on the investigation of light-matter interactions at the micro- and nanoscale level, a topic of rapidly increasing scientific interest and technological relevance, with great impact in light harvesting applications, cancer therapy, water splitting and single molecule detection, just to mention a few. Within this context, plasmonics offers a viable route for the manipulation of the electromagnetic field through the resonant interaction between metallic nanostructures and incident radiation. In fact, coupling of light with the free-electron motion leads to enhanced optical near fields, confined in subwavelength regions and localized in close proximity of the nanoparticles (localized surface plasmon resonances – LSPRs) or propagating along patterned metal/dielectric interfaces (surface plasmon polaritons – SPPs). The near-field characteristics of plasmon based devices and the straightforward tunability of their plasmonic properties across a wide spectral range make them particularly suitable for the investigation of light-matter interactions at the nanoscale level. Recent advances in nanofabrication have paved the way towards the realization of designs that boost light-matter interactions with the creation of new hybrid systems, enabling strong coupling phenomena to be established. This regime has been the subject of extensive research in the last decades and has led to fundamental discoveries, such as threshold-less nano-lasers, single-photon optical transistors and modification of the electronic properties of nanomaterials. Through the formation of hybrid states, light-matter strong coupling offers challenging perspectives by inducing significant modifications in the intrinsic properties of each constituent. Very recently, this concept has been extended from the visible spectral range, where emitting materials operate, to the infrared and

terahertz spectral range, where most of the vibrational and dissipative properties lie, offering the possibility to engineer the nanoscale phononic characteristics of hybrid materials and enhance the performance of solid-state devices.

In this work we address this issue and we exploit vibrational strong coupling to modify the phononic properties of materials, showing that the dipole-active phonon resonance of semiconducting nanocrystals can be drastically reshaped. This is achieved by exploiting the phonon strong coupling with the vacuum electromagnetic field confined and enhanced in terahertz plasmonic nanocavities. A Raman characterization of the vibrational properties of the employed nanocrystals unveils the quantum nature of the investigated phenomena, demonstrating that strong hybridization occurs even in dark conditions, i.e. no terahertz photons pumped into the system.

Chapter 1 reports a brief overview light-matter interaction regimes, i.e. from the weak to the strong coupling, addressing this topic from a theoretical point of view. Basic concepts of cavity-quantum electrodynamics (QED) are developed considering the general case of a two-level atom in an external electromagnetic field. A classical description is firstly employed and the fundamental conditions for the establishment of strong coupling are analytically derived. In the second part of the chapter, we abandon the classical view and introduce quantistic terms, therefore highlighting the quantum nature of the studied system.

Chapter 2 deals with strong coupling between plasmon modes and molecular excitonic transitions. In the first part of the chapter, fundamentals of surface plasmon polariton resonances are given, together with a brief explanation of crystal excitons. In the second part, the plasmon-exciton interaction is reviewed from a classical perspective and the state-of-the-art in the field, together with some applications, is discussed.

In chapter 3 we adapt the concepts described in chapter 2 to the terahertz spectral range, in order to achieve vibrational strong coupling between nanocavity plasmonic modes and the optical phonon resonance of semiconductor nanocrystals. Fabrication of the plasmonic elements and the numerical characterization of both their far-field and near-field properties are described in details, together with the numerical calculation of the mode volume and the expected vacuum electric field in the nanocavity regions. In the second half, we describe the nanocrystal synthesis and the realization of the overall coupled system, overviewing similar applications of the same design.

Chapter 4 presents the results demonstrating plasmon-phonon hybridization in the terahertz range. To do this, we firstly report the THz characterization of the fabricated sample that was carried out in the synchrotron facility at ELETTRA, Trieste on the SISSI beamline dedicated to material science.

Transmission measurements features the typical anti-crossing behaviour of strongly coupled oscillators and evidence the measured Rabi splitting dependence of the concentration of hybridized nano-objects. In the second part, the key principle of the present work is extensively explained. In fact, a Raman characterization shows how hybridization occurs only in the nanocavity regions even in dark conditions, without the need for terahertz excitation to be employed. These results further corroborate the nanoscale behaviour of the phonon resonance reshaping.

Chapter 5 reports preliminary results obtained with a different geometry, where the nanoantennas are replaced with plasmonic nanoslits. The new hybrid system, despite the lower field enhancement of the plasmonic elements, is endowed with higher Rabi splittings and the induced perturbations are a significant fraction of the unperturbed transition energies, hinting for the establishment of an ultra-strong coupling regime. A terahertz characterization confirms the expected results and future Raman characterization of the vibrational properties of the hybridized nanocrystals will help validating these findings.

Finally, a brief conclusion of the overall work is given with few perspectives for future developments.

# Chapter 1

# Light-matter interactions: a theoretical overview

## 1.1 Weak coupling regime

Light-matter interaction is one of the fundamental processes occurring in nature. The typical situation involves the interaction between a photon emitter (dye molecules, quantum dots, organic or inorganic semiconductors, etc.) with an external electromagnetic (EM) field. Usually, the interaction between the emitter and its local optical environment is rather weak and such that only the spontaneous emission rate is modified (the emission frequency remaining unaltered), like in the case of spontaneous emission of molecules in an optical cavity[1]. In such a situation (see Figure 1.1), we are in the so-called "weak coupling" regime and the wave functions of the emitter and the light field can be treated as unperturbed.

Let us consider the general case of a two-level atom with transition frequency $\omega_0$ interacting with the electromagnetic vacuum field. At time $t = 0$, the atom is prepared in its excited state, denoted in Dirac's notation as $|1\rangle$, and the field is in a vacuum state $|\{0\}\rangle$. In this notation, the initial overall state is then

$$|\psi(0)\rangle = |1, \{0\}\rangle \tag{1}$$

Since the atom is not in a stable configuration, it will spontaneously decay to its ground level $|0\rangle$ by means of an electric dipole transition $\mu$ and emit a photon in mode ($\boldsymbol{k}$,$s$). The state of the system after the decay will become $|0, 1_{\boldsymbol{k}s}\rangle$, which form a complete set for expanding the time-dependent wavefunction[2]:

$$\big|\psi(t)\rangle = a(t)e^{-i\omega_0 t}\big|1, \{0\}\rangle + \sum_{\boldsymbol{k},s} b_{\boldsymbol{k}s}(t)e^{-i\omega_k t}\,|0, 1_{\boldsymbol{k}s}\rangle \tag{2}$$

where $\omega_k = ck$ is the frequency of the photon. The total Hamiltonian can be expressed as the sum of three terms, $H = H_{atom} + H_{vac} + H_{int}$, and expanded as

$$H = \frac{1}{2}\hbar\omega_0\hat{\sigma}_z + \sum_{\boldsymbol{k},s}\hbar\omega_k\hat{a}^{\dagger}_{\boldsymbol{k}s}\hat{a}_{\boldsymbol{k}s} - \sum_{\boldsymbol{k},s}\hbar g_{\boldsymbol{k}s}(\hat{\sigma}_+\hat{a}_{\boldsymbol{k}s} + \hat{\sigma}_-\hat{a}^{\dagger}_{\boldsymbol{k}s}) \tag{3}$$

where $g_{\boldsymbol{k}s}$ is the atom-field coupling coefficient and $\hat{\sigma}_z$, $\hat{\sigma}_{\pm}$, $\hat{a}_{\boldsymbol{k}s}$ are linear operators acting on the states of the system. Solving the time-dependent Schrödinger equation $H|\psi(t)\rangle$ for the excited state amplitude $a(t)$, we can compute the atom transition rate to the ground state using Fermi's golden rule[3]:

$$\frac{dP_1(t)}{dt} = \left(\frac{2\pi}{\hbar}\right)|\langle 1|H_{int}|0\rangle|^2 D_{free}(\omega) \tag{4}$$

where $D_{free}(\omega) = \frac{\omega^2 V}{\pi^2 c^3}$ is the free-space density of states in the mode volume *V* occupied by the atom and $P_1$ is the probability of the atom to be in the excited state. Calculation of the interaction terms[4] finally yields the spontaneous emission in free space:

$$\Gamma_{free} = \frac{\omega_0^3\mu_{10}^2}{3\pi\varepsilon_0\hbar c^3} \tag{5}$$

where $\mu_{10}$ is the atomic transition dipole moment. If the atom is placed inside a cavity supporting a normal mode oscillating at a frequency $\omega_{cav}$, the system Hamiltonian in Eq. (3) will change by substituting the vacuum field with the quantized field of the cavity. Concurrently, the density states for free space $D_{free}(\omega)$ has to be replaced with a cavity modified density of states $D_{cav}(\omega)$:

$$D_{cav}(\omega) = \frac{\kappa}{2\pi V}\frac{1}{(\kappa/2)^2 + (\omega_{cav} - \omega)^2} \tag{6}$$

where V is the cavity mode volume and κ is the cavity dissipation rate, which takes into account the cavity losses per optical cycle.

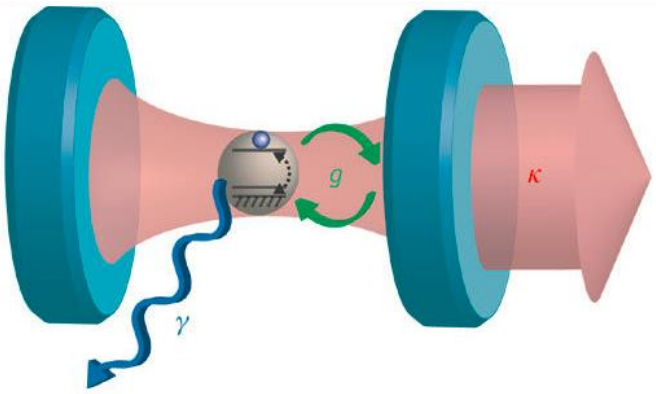


**Figure 1.1:** Schematic of a two-level atom in a cavity, whose stored energy is lost at a rate κ due to imperfectly reflective mirrors or absorption in the material. Coherent exchange of excitation between the atom and the cavity field depends on the coupling strength *g*, as indicated by the dashed arrow for the atom and the green arrows for the cavity field[5].

Depending on the detuning of the atom transition frequency $\omega_0$ from the cavity normal mode frequency, two opposite situations arise. In resonance conditions, i.e. in the case of $\omega = \omega_0 = \omega_{cav}$, and perfect matching of dipole orientation, there is enhancement of the atom spontaneous emission rate, as represented in the following equation:

$$\Gamma_{cav} = \frac{3}{4\pi^2}\left(\frac{\lambda_0^3}{V}\right) Q\Gamma_{free} \tag{7}$$

where $Q = \omega_{cav}/\kappa$ denotes the cavity quality factor. In off-resonance conditions (i.e. $\omega_0 \neq \omega_{cav}$), instead, there is inhibition of spontaneous emission, as given by:

$$\Gamma_{cav} = \frac{3}{16\pi^2}\left(\frac{\lambda_0^3}{V}\right) Q^{-1}\Gamma_{free} \tag{8}$$

This results suggests how in the weak-coupling regime the spontaneous emission, and therefore the natural lifetime of the excited emitter, can be modified leaving the energy spectrum of the total system unchanged. When the cavity photon and the atom transition energies are degenerate, the atomic decay rate can be increased considerably as quantified by the so-called *Purcell-factor*[6]:

$$\frac{\Gamma_{cav}}{\Gamma_{free}} = \frac{3Q\lambda^3}{4\pi^2 V} \tag{9}$$

In a simplified interpretation, the cavity can be thought as a spectrally narrow reservoir of states with a large density around the cavity mode frequency. The number of final states in which the excited atom can decay is therefore increased and the effect is amplified with high *Q* cavities and small mode volumes *V*.

Another interesting example of weak coupling is Förster resonance energy transfer (FRET)[7] from an excited "donor" to an "acceptor" molecule thorough resonant dipole-dipole interaction. In the classical description of this phenomenon, the two interacting molecules can be viewed as oscillating dipoles, with the donor dipole initially in oscillation and the acceptor one at rest. Owing to a resonance condition, which can be established provided that the emission spectrum of the donor partially overlaps with the absorption spectrum of the acceptor (see Figure 1.2a-b), the excitation energy is partially transferred from the first dipole to the second one. Interaction between the dipoles is non-radiative, but it is mediated electromagnetically by a virtual photon which is emitted and immediately absorbed.

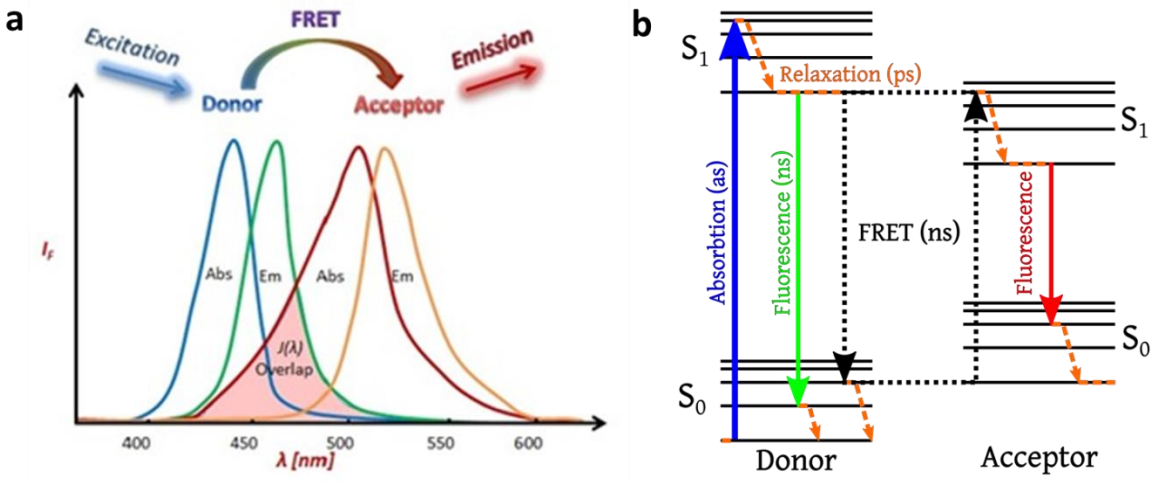


**Figure 1.2: a)** Absorption and emission spectrum for a donor and an acceptor molecule; the shaded area represents their spectral overlap. **b)** Jablonski diagram of FRET and typical timescales of each transition.

In addition to the spectral overlap and the relative orientation of the donor emission and acceptor absorption dipole moments, the FRET efficiency also depends on the relative distance between the interacting molecules. By calculating the power emitted by the donor dipole and the power absorbed by

the acceptor dipole, it is possible to obtain the transfer rate constant as a function of molecule separation[8]:

$$k_T = k_D \left[\frac{R_0}{r}\right]^6 = \frac{1}{\tau_D^0}\left[\frac{R_0}{r}\right]^6 \tag{10}$$

where $k_D$ is the emission rate constant of the donor and $\tau_D^0$ its lifetime in the absence of transfer, r is the intermolecular distance and $R_0$ is the critical distance or Förster radius. When the molecule separation is identical to the Förster radius, resonant energy transfer to the acceptor and spontaneous decay of the excited donor to its ground state are equally probable ($k_T = k_D$). As it can be noted from the relation above, the transfer rate goes with the inverse of the sixth power of molecule separation and the critical distance represents a threshold between radiative and non-radiative energy transfer (usually occurring for r < 10 nm).

Even in the case of FRET, a modification of the local optical environment can be used to control and enhance the energy transfer rate[9], similarly to the case of an atom-cavity system previously described, and leaving the energy spectrum of the system unaltered. In this regime, the transfer rate is smaller than the relaxation rate of the uncoupled molecules, meaning that once the energy is transferred from the donor to the acceptor, there is very little chance of an energy back transfer. This process can be reversed and completely modified by further increasing the molecules coupling strength towards the "strong coupling" regime, as it will be discussed in the next section.

## 1.2 Strong coupling regime

In order to continue along the leitmotiv of the previous section, let us consider again the case of a two-level atom in an electromagnetic field. Upon excitation in the weak coupling regime, the energy levels of the atom remain essentially unchanged. If the interaction energy with the external field becomes sufficiently large, energy is exchanged at a rate faster than any relaxation rate and the overall system enters the so-called strong coupling regime. In this limit, it is no longer possible to distinguish between the emitting atom and the exciting field, but they must be thought as a single system where the atomic states are inextricably linked with the modes of the local optical environment. The energy spectrum of the coupled pair is profoundly modified and new hybrid light-matter states are formed by very rapid photon exchange. These energy states are usually denoted as upper ($P_+$) and lower ($P_-$) polariton bands

and are separated by a characteristic energy splitting, also called *Rabi splitting*, whose magnitude depends on the interaction strength. The origin and interpretation of the new hybrid system can be understood both in a classical and quantum picture, as briefly highlighted below.

## 1.3 Strong coupling: classical description

In the following, we will describe a two-coupled oscillator model and derive classically the conditions for strong coupling. The interacting systems (A and B) are represented as two harmonic oscillators, respectively of masses $m_A$ and $m_B$ and spring constants $k_A$ and $k_B$ (see Figure 1.3). This ideal situation corresponds to the case of two coupled pendula (oscillating at small frequencies), an optical field coupled to a dipolar two-level transition of an atom/molecule or to a microwave field coupled to a resonating circuit.

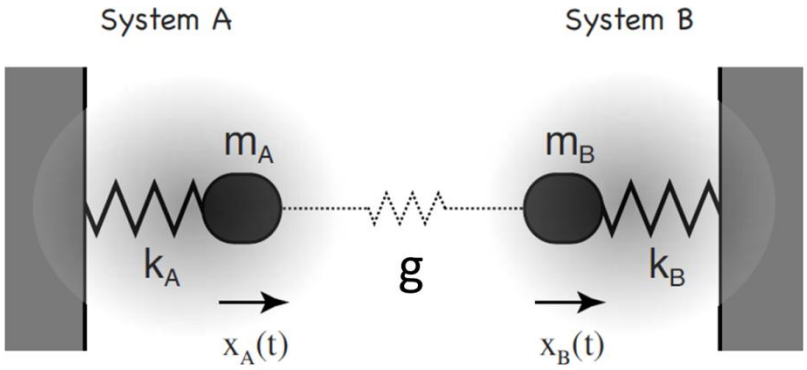


**Figure 1.3:** Coupled system illustrated by mechanical harmonic oscillators. The coupling *g* of the two oscillators leads to a shift of the eigenfrequencies and a characteristic frequency splitting[10].

In the absence of coupling ($g = 0$) and solving the equation of simple harmonic motion for each isolated oscillator, the eigenfrequencies of the systems are the standard $\omega_A^0 = \sqrt{\frac{k_A}{m_A}}$ and $\omega_B^0 = \sqrt{\frac{k_B}{m_B}}$ respectively. If we now introduce coupling ($g \neq 0$), the equations of motion of the total system become:

$$m_A\ddot{x}_A + k_A x_A + g(x_A - x_B) = 0 \quad (11)$$

$$m_B\ddot{x}_B + k_B x_B - g(x_A - x_B) = 0 \quad (12)$$

Since in the strong coupling regime we expect to observe the arising of two hybrid energy levels, we seek solutions of the form $x_i(t) = x_i^0 exp[-i\omega_{\pm}t]$ , where $\omega_{\pm}$ are the new eigenfrequencies of the coupled system. By inserting this ansatz in the homogeneous system of equations above and solving for the new eigenfrequencies, we obtain:

$$\omega_{\pm}^2 = \frac{1}{2}\left[\omega_A^2+\omega_B^2 \pm \sqrt{(\omega_A^2 - \omega_B^2)^2 + 4\Gamma^2\omega_A\omega_B}\right] \tag{13}$$

where $\omega_A = \sqrt{\frac{k_A+g}{m_A}}$ , $\omega_B = \sqrt{\frac{k_B+g}{m_B}}$ and $\Gamma = \frac{\sqrt{g/m_A}\sqrt{g/m_B}}{\sqrt{\omega_A\omega_B}}$. The new frequencies $\omega_{\pm}$ represent the normal modes of the coupled oscillator system and are different from those of the original oscillator modes.

In order to illustrate the solutions of Eq. (13), we set $k_A = k_0$, $k_B = k_0 + \Delta k$ and $m_A = m_B = m_0$, which results in a frequency detuning between the two oscillators. In this simplified picture, one of the oscillator frequency can vary while the other one is not tunable: this resembles the case of an atom interacting with an electromagnetic field, where the energy of the electronic transition is fixed (system A) while the irradiation frequency can be changed (system B).

In the absence of coupling ($g$ = 0) the two oscillators system behaves as depicted in Figure 1.4a. As Δk is increased from $-k_0$ to $k_0$, the frequency of system B increases from zero to the maximum value of $\sqrt{2}\omega_0$, while the frequency of oscillator A stays constant. The two frequency curves intersect at $\Delta k = 0$. Once we introduce coupling ($g \neq 0$), the two curves no longer intersect at the resonance condition, i.e. when the frequency of the two oscillators coincide (see Figure 1.4b).

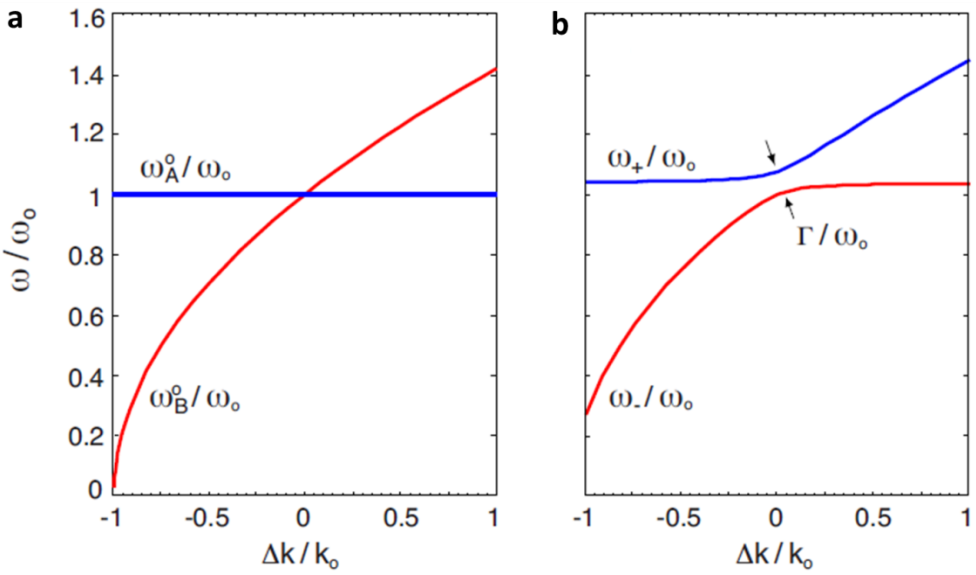


**Figure 1.4: a)** Eigenfrequencies of the uncoupled oscillators (g = 0). **b)** Frequency anticrossing as a result of coupling (g ≠ 0). The frequency splitting $(\omega_+ - \omega_-)$ scales linearly with the coupling strength $g$[10].

Far away from resonance the coupled oscillators behave as the original ones and their frequencies are practically unaltered from the uncoupled case. Near the crossing point of the uncoupled case, two new normal modes appear and a characteristic *anticrossing* behaviour is observed. The energy separation between the new eigenfrequencies at the resonance spectral position is called *normal mode* or equivalently, *Rabi splitting*, and it is given simply by

$$\Gamma = \hbar(\omega_+ - \omega_-) \tag{14}$$

Since $\Gamma \propto g$, as obtained from the equations above, the energy splitting increases with increasing coupling strength and together with the energy exchange rate between the new normal modes, the so-called *Rabi frequency*, $\Omega = (\omega_+ - \omega_-)$. This situation corresponds to an ideal case where we have ignored any damping in the oscillations from external forces. Damping can be introduced in the equations of motion (11-12) in the form of frictional terms $\gamma_A \dot{x}_A$ and $\gamma_B \dot{x}_B$ and this gives rise to complex frequency eigenvalues, whose imaginary part represents the linewidths. In the frequency vs. wavenumber plot this effect appears as a smearing of the frequency curves, as it is pictorially represented in Figure 1.5.

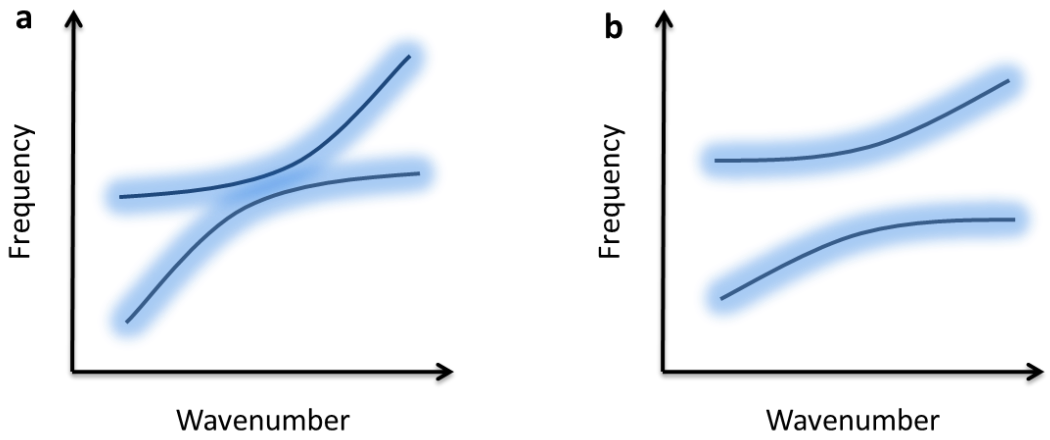


**Figure 1.5: a)** Schematic view of the weak coupling regime: the splitting is hidden under the linewidths. **b)** Schematic view of the strong coupling regime: the energy splitting between the hybrid modes is large enough compared to the linewidth and it is experimentally visible.

Here, the continuous lines depict the undamped oscillators frequencies, while the surrounding shade schematically represents the linewidth. Although the hybrid modes always appear in the coupled system, whether they are experimentally visible or not depends on the coupling strength. For mechanical oscillators, the system is said to be in the strong coupling regime when the relation $g > \omega$ is satisfied: this means that the coupling modifies the oscillation frequency considerably when it is of the order of the frequency itself. However, this relation does not hold anymore in other contexts, like in the case of light fields ($10^{15}$ Hz or more). A much more useful and extensive comparison can be made by taking into consideration the transitions linewidths, and this concept is well exemplified in the two cases of Figure 1.5. For very strong damping it is no more possible to distinguish the hybrid modes and their frequency splitting (see Figure 1.5a): we are in the weak coupling regime. The Rabi splitting becomes significant only when the coupling is large compared to the linewidths, which means that the dissipation in each original system is smaller than the coupling strength (see figure 1.5b). In other words, to observe strong coupling the frequency splitting has to be larger than the sum of the linewidths[10]:

$$\frac{\Gamma}{\gamma_A/m_A + \gamma_B/m_B} > 1 \tag{15}$$

This condition is clearly observable in the schematic representation of Figure 1.5b.

## 1.4 Strong coupling: semi-classical description

Following the works of Grynberg[11] and Törmä[12], we report here the strong-coupling derivation in the semi-classical limit, where the interacting field is a classical electromagnetic wave and the emitter (an atom/molecule/quantum dot) has a quantum nature, which means that it is described as a two-level system governed by the Schrödinger equation.

Within this representation, we can neglect the magnetic term of the field and express the exciting light in the form of a time-varying plane wave $\boldsymbol{E}\cos(\omega t)\, e^{i\boldsymbol{k}\cdot\boldsymbol{r}}$, where ω and $\boldsymbol{k}$ are the frequency and the wavevector and **E** contains the field amplitude and the polarization vector of the field. In order to simplify the electromagnetic part we apply the standard *dipole approximation*[11], which allows us to get rid of the space dependence of the field. This approximation assumes that the displacements of the emitter electrons due to the field are small compared to the inverse of the wavevector.

The two-level emitter interacting with the light field has an excited $|e\rangle$ and a ground $|g\rangle$ state with energies $E_e$ and $E_g$ respectively. In a vectorial basis the two energy levels can be written in the form $|g\rangle = \begin{pmatrix}0\\1\end{pmatrix}$ and $|e\rangle = \begin{pmatrix}1\\0\end{pmatrix}$. Transition from the ground to the excited state and viceversa are provided by the operators

$$\sigma_+ = \begin{pmatrix}0 & 1\\ 0 & 0\end{pmatrix}, \quad \sigma_- = \begin{pmatrix}0 & 0\\ 1 & 0\end{pmatrix}, \tag{16}$$

meaning that $\sigma_+|g\rangle = |e\rangle$ and $\sigma_-|e\rangle = |g\rangle$. In this two-dimensional space four independent linear operators form a complete base. Therefore, we can add

$$\sigma_z = \begin{pmatrix}1 & 0\\ 0 & -1\end{pmatrix}, \quad I = \begin{pmatrix}1 & 0\\ 0 & 1\end{pmatrix}, \tag{17}$$

in order to fulfill this requirement. The overall Hamiltonian can be written in the form[11]

$$H = \frac{1}{2}E_e(I+\sigma_z) + \frac{1}{2}E_g(I-\sigma_z) + \hbar\Omega_0(\sigma_+ + \sigma_-)\cos(\omega t) \tag{18}$$

where $\Omega_0$ is the semi-classical Rabi frequency, which is proportional to the emitter dipole moment μ and the field amplitude E**,** $\Omega_0 = -\frac{\boldsymbol{\mu}\cdot\boldsymbol{E}}{\hbar}$. Performing a change of basis in the so-called rotating wave approximation (RWA) (for details see the work of Törmä et al.[12]), that is reliable if we are quite close

to resonance $\omega \sim \omega_0$ and the Rabi frequency is not in the order of the field frequency, we obtain a more convenient form of the system Hamiltonian

$$H = -\frac{\hbar\delta}{2}\sigma_z + \frac{\hbar\Omega_0}{2}(\sigma_+ + \sigma_-) \tag{19}$$

where $\delta = \omega - \frac{(E_e - E_g)}{\hbar} = \omega - \omega_0$ is the detuning of the EM field from the emitter transition. Diagonalization of this Hamiltonian yields the eigenvalues of the coupled system,

$$E_1 = -\frac{1}{2}\hbar\sqrt{\delta^2 + \Omega_0^2}\ ,\ \ E_2 = \frac{1}{2}\hbar\sqrt{\delta^2 + \Omega_0^2} \tag{20}$$

where appears the so-called generalized Rabi frequency $\Omega = \sqrt{\delta^2 + \Omega_0^2}$. The corresponding eigenstates can then be written in the form

$$|1\rangle = -\sin\theta\,|e\rangle + \cos\theta\,|g\rangle \tag{21}$$

$$|2\rangle = \cos\theta|e\rangle + \sin\theta\,|g\rangle \tag{22}$$

where

$$\cos\theta = \frac{\Omega - \delta}{\sqrt{(\Omega - \delta)^2 + \Omega_0^2}}\ ,\ \ \sin\theta = \frac{\Omega_0}{\sqrt{(\Omega - \delta)^2 + \Omega_0^2}} \tag{23}$$

In order to interpret these results, it is interesting to consider the system in a resonance situation, that is when the field and the emitter transition have the same energy, $\delta = 0$. We can then rewrite the eigenstates and the eigenenergies for this specific case finding

$$|1\rangle = \frac{1}{\sqrt{2}}(|g\rangle - |e\rangle)\ ,\ \ |2\rangle = \frac{1}{\sqrt{2}}(|g\rangle + |e\rangle) \tag{24}$$

$$E_1 = -\frac{\hbar\Omega_0}{2}\ \ ,\ \ E_2 = \frac{\hbar\Omega_0}{2} \tag{25}$$

This is an important result, meaning that the eigenstates of the system are an equal superposition of the ground and the excited states. Moreover, the time-evolution of the system initially in the ground state can be written as[12]

$$|\Psi(t)\rangle = \cos(\Omega_0 t/2)\,|g\rangle - i\sin(\Omega_0 t/2)\,|e\rangle \tag{26}$$

that is, the system performs *Rabi oscillations* between the ground and the excited states. At resonance the frequency of these oscillations corresponds to the *Rabi frequency* $\Omega_0$, while away from it, Rabi oscillations take place at the generalized Rabi frequency $\Omega$ and are smaller in amplitude.

So far, we have considered the case of a single two-level quantum emitter interacting with an EM field. If we now extend the semi-classical model to the case of many emitters in a cavity, with their transition energy tuned with the energy of the cavity normal mode, the dynamics of the coupled system is quite different (for details see the work of Zhu et al.[13]). As it was theoretically predicted and also found experimentally, the Rabi splitting for N oscillators in a modal volume V is proportional to the transition dipole moment (as in the N = 1 emitter case) and also to the concentration of the emitters in the cavity:

$$\Gamma \propto \mu\sqrt{\frac{N}{V}} \tag{27}$$

This does not mean that the strongly coupled emitters perform Rabi oscillations with a frequency proportional to the concentration, which is valid for the special case N = 1. However, the overall system can be thought as a collection of emitters individually performing Rabi oscillations with frequency $\Omega_0 = -\mu\frac{E_0}{\hbar}$ and driven by a coherent field, i.e. all emitters that start their oscillation simultaneously keep oscillating in phase. If N emitters perform such oscillations in phase, the contribution of each oscillator sums up and the linear absorption shows a splitting proportional to the square root of their concentration and dipole moment, as expressed in the relation above.

## 1.5 Strong coupling: fully quantum description

In the fully quantum description both the two-level emitter and the interacting EM field are quantized. In this picture, the system is described by the so-called Jaynes-Cummings Hamiltonian[14]

$$H = \frac{1}{2}\hbar\omega_0\sigma_z + \hbar\omega\hat{a}^\dagger\hat{a} + \hbar g(\sigma_+\hat{a} + \sigma_-\hat{a}^\dagger) \tag{28}$$

where g is the coupling constant, $\hat{a}$ is the annihilation operator which corresponds to the destruction of a photon and $\hat{a}^\dagger$ is the creation operator that corresponds to the creation of a photon. This Hamiltonian only couples the states $|e\rangle|n\rangle$ and $|g\rangle|n+1\rangle$ where *n* refers to the photon number (one photon is emitted/absorbed after a transition between the ground and the excited state. The Hamiltonian can then be expressed in terms of the photon number

$$H = \sum_n H_n \tag{29}$$

and in the basis $\binom{1}{0} = |e\rangle|n\rangle$, $\binom{0}{1} = |g\rangle|n+1\rangle$ the summation element $H_n$ can be rewritten as

$$H_n = \hbar\left(n + \frac{1}{2}\right)\omega\begin{pmatrix}1 & 0\\ 0 & 1\end{pmatrix} + \frac{\hbar}{2}\begin{pmatrix}-\delta & 2g\sqrt{n+1}\\ 2g\sqrt{n+1} & \delta\end{pmatrix} \tag{30}$$

with $\delta$ being the detuning defined in the previous sections. Diagonalization of this Hamiltonian yields the eigenvalues:

$$E_{1n} = \hbar\left(n + \frac{1}{2}\right)\omega - \frac{1}{2}\hbar\sqrt{\delta^2 + 4g^2(n+1)}$$

$$E_{2n} = \hbar\left(n + \frac{1}{2}\right)\omega + \frac{1}{2}\hbar\sqrt{\delta^2 + 4g^2(n+1)} \tag{31}$$

where the generalized Rabi frequency appears $\Omega_n = \sqrt{\delta^2 + 4g^2(n+1)}$. As in the semi-classical case, the eigenstates can be written in terms of *sine* and *cosine* functions (for details see the work of Törmä et al.[12]) and become

$$|1n\rangle = -\sin\theta_n\,|e\rangle|n\rangle + \cos\theta_n|g\rangle|n+1\rangle$$

$$|2n\rangle = \cos\theta_n\,|e\rangle|n\rangle + \sin\theta_n\,|g\rangle|n+1\rangle \tag{32}$$

When the detuning vanishes and we are in a resonance condition, the eigenstates for the system with *n* photons take the form:

$$|1n\rangle = \frac{1}{\sqrt{2}}(-|e\rangle|n\rangle + |g\rangle|n+1\rangle)$$
$$|2n\rangle = \frac{1}{\sqrt{2}}(|e\rangle|n\rangle + |g\rangle|n+1\rangle) \tag{33}$$

This means that the eigenstates of the coupled system are an equal superposition of the excited state with no extra photons and the ground state with an additional extra photon. Surprisingly, the quantum description gives a results which is in the contrast with the classical and semi-classical description: the energy splitting takes discrete values depending on the photon number *n* and does not vanish even in the case of $n = 0$, i.e. zero photons when the emitter is the excited state and one photon when it is in the ground state. The energy splitting in this special case is called ***vacuum Rabi splitting***[15] and its existence is attributed to quantum vacuum fluctuations. The system now performs Rabi oscillations as in the semi-classical two-level emitter, but with a non-vanishing frequency also with zero photon number. In the specific case of an atom-cavity system, under zero photon conditions, the atom-field coupling strength *g* is given by

$$\mathrm{g} = -\mu\frac{E_{vac}}{\hbar} \tag{34}$$

where μ is the atom dipole moment and the vacuum electromagnetic field amplitude is $E_{vac} = \sqrt{\hbar\omega/2\varepsilon_r\varepsilon_0 V}$. The field amplitude depends on the photon energy $\hbar\omega$, at which resonance occurs, and the cavity-mode volume V. As $E_{vac}$ scales with $1/\sqrt{V}$, careful engineering of cavity systems is thus needed in order to achieve the strong coupling regime even under no illumination condition (this issue will be developed in chapter 3).

Generalization to the many emitter case gives similar results to the semi-classical description in terms of expected Rabi splitting (for details see the work of Agranovich et al.[16]). The overall system can now be viewed as a collection of two-level oscillators acting as a *giant quantum oscillator*[12] with a large

dipole moment. In this picture, we can assume that the photon field and the giant oscillator composed of N emitters interact with a coupling strength proportional to $\mu\sqrt{N/V}$ and perform Rabi oscillations between the normal modes at this frequency.

**References**


[1] Glauber, R. J.., Lewenstein, M., "Quantum optics of dielectric media," Phys. Rev. A **43**(1), 467–491, American Physical Society (1991).

[2] Weisskopf, V. F.., Wigner, E. P., "Calculation of the natural brightness of spectral lines on the basis of Dirac's theory," Z. Phys. **63**, 54–73 (1930).

[3] Fermi, E., "High Energy Nuclear Events," Prog. Theor. Phys. **5**(4), 570–583 (1950).

[4] Walther, H., Varcoe, B. T. H., Englert, B.-G.., Becker, T., "Cavity quantum electrodynamics," Reports Prog. Phys. **69**(5), 1325–1382 (2006).

[5] Kimble, H. J., "The Quantum Internet" (2008).

[6] Purcell, E. M., "Spontaneous Emission Probabilities at Radio Frequencies BT - Confined Electrons and Photons: New Physics and Applications," E. Burstein and C. Weisbuch, Eds., Springer US, Boston, MA, 839 (1995).

[7] Andrew, P.., Barnes, W. L., "Förster Energy Transfer in an Optical Microcavity," Science (80-. ). **290**(5492), 785 LP-788 (2000).

[8] Andrews, D. L.., Bradshaw, D. S., "Virtual photons, dipole fields and energy transfer: a quantum electrodynamical approach," Eur. J. Phys. **25**(6), 845–858 (2004).

[9] Blum, C., Zijlstra, N., Lagendijk, A., Wubs, M., Mosk, A. P., Subramaniam, V.., Vos, W. L., "Nanophotonic Control of the Förster Resonance Energy Transfer Efficiency," Phys. Rev. Lett. **109**(20), 203601, American Physical Society (2012).

[10] Novotny, L., "Strong coupling, energy splitting, and level crossings: A classical perspective," Am. J. Phys. **78**(11), 1199–1202, American Association of Physics Teachers (2010).

[11] Grynberg, Gilbert; Aspect, Alain; Fabre, Claude; Cohen-Tannoudji, F. by C., Introduction to quantum optics: from the semi-classical approach to quantized light (2010).

[12] Törmä, P.., Barnes, W. L., "Strong coupling between surface plasmon polaritons and emitters: a review," Reports Prog. Phys. **78**(1), 13901 (2015).

[13] Zhu, Y., Gauthier, D. J., Morin, S. E., Wu, Q., Carmichael, H. J.., Mossberg, T. W., "Vacuum

Rabi splitting as a feature of linear-dispersion theory: Analysis and experimental observations," Phys. Rev. Lett. **64**(21), 2499–2502, American Physical Society (1990).

[14] Meystre, P.; Sargent, M. III; Claus, A. C. ., Elements of quantum optics (1991).

[15] Khitrova, G., Gibbs, H. M., Kira, M., Koch, S. W.., Scherer, A., "Vacuum Rabi splitting in semiconductors," 81, Nature Publishing Group (2006).

[16] Agranovich, V. M., Litinskaia, M.., Lidzey, D. G., "Cavity polaritons in microcavities containing disordered organic semiconductors," Phys. Rev. B **67**(8), 85311, American Physical Society (2003).

# Chapter 2

# Plasmon-excitons strong coupling

## 2.1 Surface plasmon polaritons: a brief overview

Plasmonics is an emerging area of research in the field of nanophotonics, which has found many applications in spectroscopy[1–3], metamaterials engineering[4–6], biosensing[7,8], lasing[9,10], non-linear[11,12] and quantum optics[13,14]. It is based on interaction processes between electromagnetic radiation and conduction electrons at metallic interfaces leading to enhanced optical near-fields confined in subwavelength dimensions. Under appropriate conditions, collective oscillations of the electron plasma can be resonantly excited in close proximity of metallic nanoparticles (localized surface plasmon resonances – LSPRs) or propagating along metal/dielectric interfaces (surface plasmon polaritons – SPPs). Owing to their bound nature, surface plasmons are endowed with interesting attributes that make them suitable for light-matter interactions in the strong coupling regime: optical field confinement, optical field enhancement and near-field character.

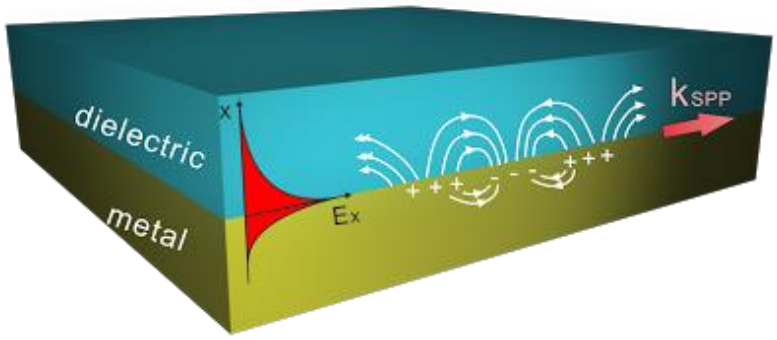


**Figure 2.1:** Schematic of the electric field and charge distribution associated with the surface plasmon polariton mode on a planar surface, at the interface between a metal and a dielectric medium. In the out-of-plane direction (x direction in the sketch) the strength of the field associated with the SPP mode decays exponentially with distance from the metallic surface.

The strength of the electric field associated with the bound SPP mode decays exponentially with distance away from the metal surface (the spatial distribution of the electric field is shown in Figure 2.1). In the dielectric medium the decay length is approximately $\lambda/2n_r$, where $n_r$ is the refractive

index of the dielectric, while inside the metal corresponds to the skin depth (typically ~ 20nm for noble metals in the visible spectrum).

The considerations taken above can be explained by solving Maxwell equations under appropriate boundary conditions and looking for a solution in the form of a surface wave. The dispersion relation of SPPs propagating at the metal-dielectric interface is then found to be[15]:

$$k_{SPP} = \frac{\omega}{c}\sqrt{\frac{\varepsilon_1 \varepsilon_2}{\varepsilon_1 + \varepsilon_2}} \tag{35}$$

where $\varepsilon_1$ and $\varepsilon_2$ are the frequency dependent relative permittivities of the two media. For conductors described by Drude dispersion law, i.e. $\varepsilon_m(\omega) = 1 - \omega_p^2/\omega^2$ ($\omega_p$ is the plasma frequency of the metal), equation (35) takes the form depicted in Figure 2.2.

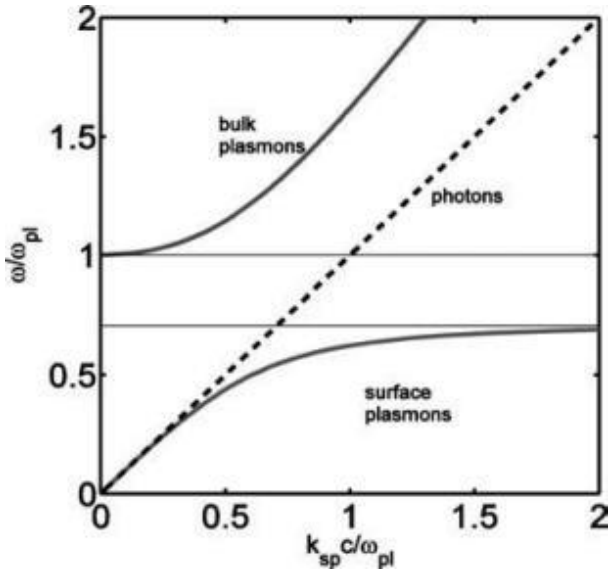


**Figure 2.2:** Dispersion law of plasmon oscillations in a metal-dielectric system, equation (35), in the case of Drude dispersion. The lower branch corresponds to bound surface plasmons, while the upper curve corresponds to bulk plasmons; the dashed line is the light line and corresponds to dispersion of photons in free space[16].

The branch related to frequencies $\omega > \omega_{pl}$ corresponds to bulk plasmons, while the lower energy branch with $\omega < \omega_{pl}$ corresponds to surface plasmons. Regarding the latter, for a given frequency the in-plane wavevector (and hence the momentum) of the SPP mode is always greater than that of light propagating in the same plane. As a consequence, freely propagating light in the dielectric medium

cannot couple to SPPs, but other momentum-matching schemes are required, e.g. prism or grating coupling, near-field or non-linear coupling[17–20].

The situation is different in the case of subwavelength metallic nanostructures, since incident light can promote collective oscillations of the conduction electrons with no momentum mismatch to overcome. When electrons are displaced relative to the opposite charge distribution of the static cores, a net amount of opposite charges will build up at opposite sides of the nanostructure (see Figure 2.3). Coulomb interaction between the charges will provide a restoring force, leading to a natural frequency of oscillation. If the incident light is of the same frequency, energy can be coupled into a localized surface plasmon mode (LSPR), the frequency of which can be tuned by modification of the nanostructure shape and composition. As with the planar surface, the fields associated with the plasmon mode are confined to the vicinity of the nanostructure, typically on a length scale comparable to its radius of curvature.

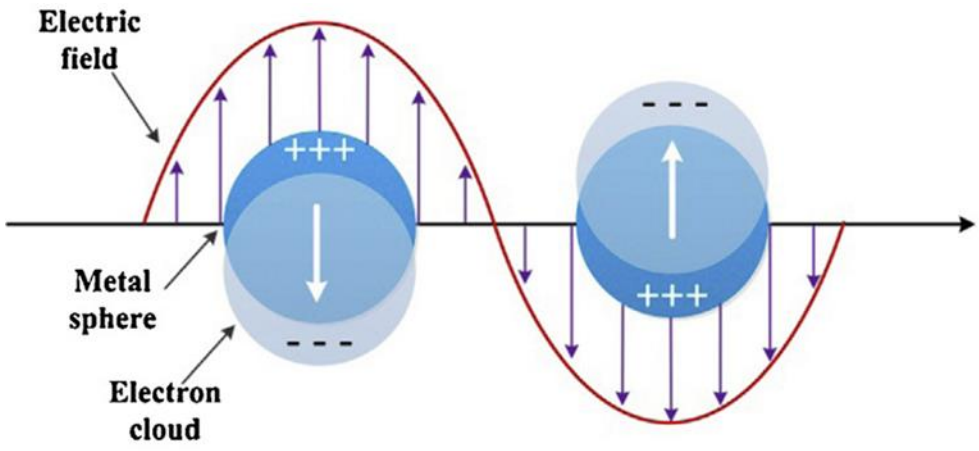


**Figure 2.3:** Illustration of the excitation of localized surface plasmon resonance around a metal nanoparticle.

The response of a spheroidal object of subwavelength dimension to plane-wave illumination, giving rise to a LSPR mode around the nanoparticle, is well described in the framework of the quasistatic approximation of Mie theory[21]. In the case of elongated particles, as our nanoantenna design (see chapter 3), a better physical insight is provided by a simple mass-and-spring model[22]. In this picture, the plasmon resonance frequency of the nanoparticle is given by $\omega_{res} = \sqrt{D/m}$, where $D$ and $m$ are the elastic constant of the restoring force and the total effective mass of the electron system, respectively. To estimate the resonance frequency, we assume a particle of cylindrical shape as depicted in Figure 2.4a. When the electron cloud in the particle is displaced by $\Delta x$, opposite point charges $\pm q$ build up at

both ends and their magnitude depends on the charge carrier density ρ and the cross-sectional area $A$ of the cylinder as $q = \rho e A \Delta x$, where $e$ is the elementary charge. The Coulomb potential energy of the two charges is then

$$W(\Delta x) = \frac{1}{4\pi\varepsilon_0}\frac{q^2}{d} = \frac{1}{4\pi\varepsilon_0}\frac{(\rho e A)^2}{d}\Delta x^2 \tag{36}$$

The restoring force acting on the opposite charges can now be determined as

$$F(\Delta x) = -\frac{\partial W(\Delta x)}{\partial \Delta x} = -\frac{1}{2\pi\varepsilon_0}(\rho e)^2\frac{A^2}{d}\Delta x = -D\Delta x \tag{37}$$

from which the spring constant $D$ is obtained. The linear relationship between displacement and restoring force leads to harmonic oscillations of the system. The mass of the whole electron cloud involved in the motion is given by $m = \rho m_e A d$, where $m_e$ is the effective electron mass. We therefore obtain a relation of the plasmon resonance frequency as a function of the aspect ratio $R$ of the elongated particle:

$$\omega_{res} = \frac{\omega_p}{2\sqrt{2}}\frac{1}{R} \tag{38}$$

where we have substituted the plasma frequency $\omega_p^2 = \rho e^2/(\varepsilon_0 m_e)$ as well as $A = \pi r^2$. Even if approximate, Eq. (38) provides a good estimate of $\omega_{res}$ and highlights its proportionality relationship with $1/R$.

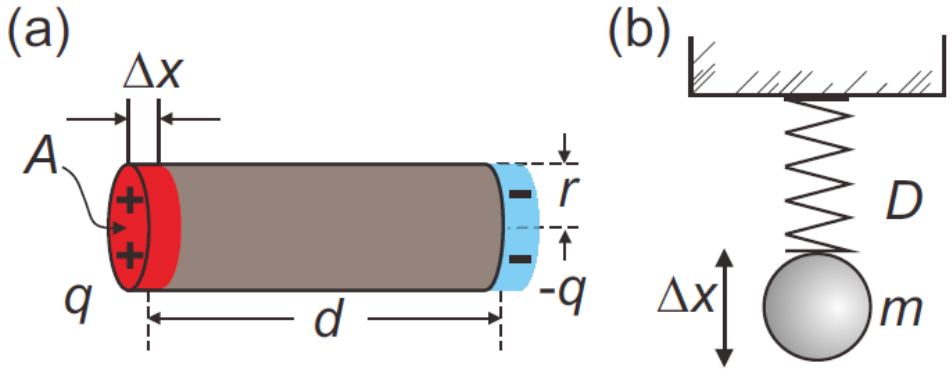


**Figure 2.4: a)** Sketch of a plasmonic particle whose electron cloud has been displaced by $\Delta x$. The resulting positive and negative charge distributions at both ends are treated as point-like charges. **b)** The resulting oscillation can be modeled by

an effective spring constant *D* and the effective mass *m* of the moving electron cloud.

Recent advances in nanofabrication techniques have allowed nanoscale engineering of the optical properties of metallic nanostructures from the UV to the far-infrared, enabling a huge variety of applications in many interdisciplinary fields[23–25]. Through the exploitation of both top-down[26,27] (ion beam milling, electron beam lithography, etc.) and bottom-up[28,29] approaches (chemical synthesis, electroplating, etc.) many different nanostructure design have been realized with different shape, material composition and extremely well-controlled size.

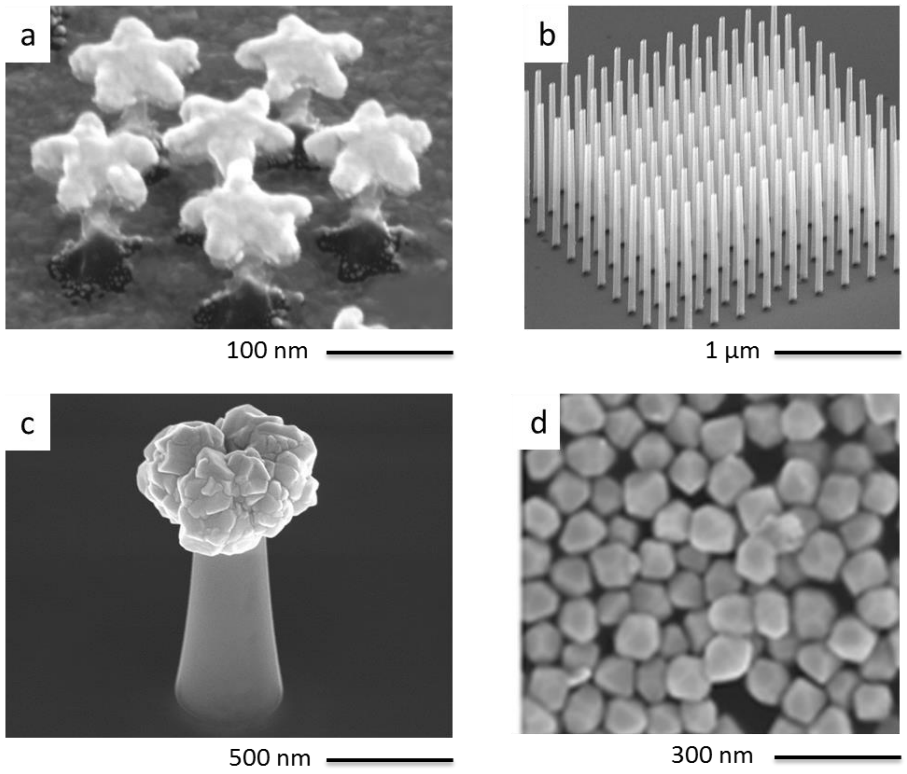


**Figure 2.5: a)** SEM tilted view of nanostars on silicon pillars with sub-10 nm inter particle separation and 150 nm pillar height realized through Electron Beam Lithography (EBL) plus Reactive-Ion Etching (RIE)[30]. **b)** Hollow nanoantenna array with 1.5 µm in height and 300 nm separation realized by means of Focused Ion Beam (FIB) technique[26]. **c)** 3D nanoantenna with electroplated gold on top realized with FIB plus an electroplating technique[28]. **d)** Au nanorods with controlled morphology chemically synthesized from aqueous-based solutions[29].

In Figure 2.5 various examples of recently published plasmonic architectures are reported; the first one (a) shows three-dimensional nanostars on silicon pillars fabricated with the combination of Electron Beam Lithography (EBL) and Reactive-Ion Etching (RIE) techniques, resulting in small inter-particle

separation (IPS), well-controlled shape and dimension and sharp edges. Figure 2.5b instead, shows three-dimensional nanoantennas for IR applications realized through Focused Ion Beam (FIB), while Figure 2.5c represents a nanoantenna with a bulky gold-palladium head for hydrogen detection realized with the combination of FIB and a galvanic electroplating technique. On the contrary, Figure 2.5d shows gold nanorods for SERS applications, which are chemically synthesized from aqueous solutions.

By changing size and shape[31] of the plasmonic nanoparticles and their IPS[32], the LSPR spectral position can be finely tuned/manipulated across a wide spectral range, as it is shown in Figure 2.6. Here, by varying the height of vertical hollow nanotubes and the inter-antenna distance the far-field response of plasmonic arrays can be varied across the near-infrared (NIR) to match the desired spectral requirements.

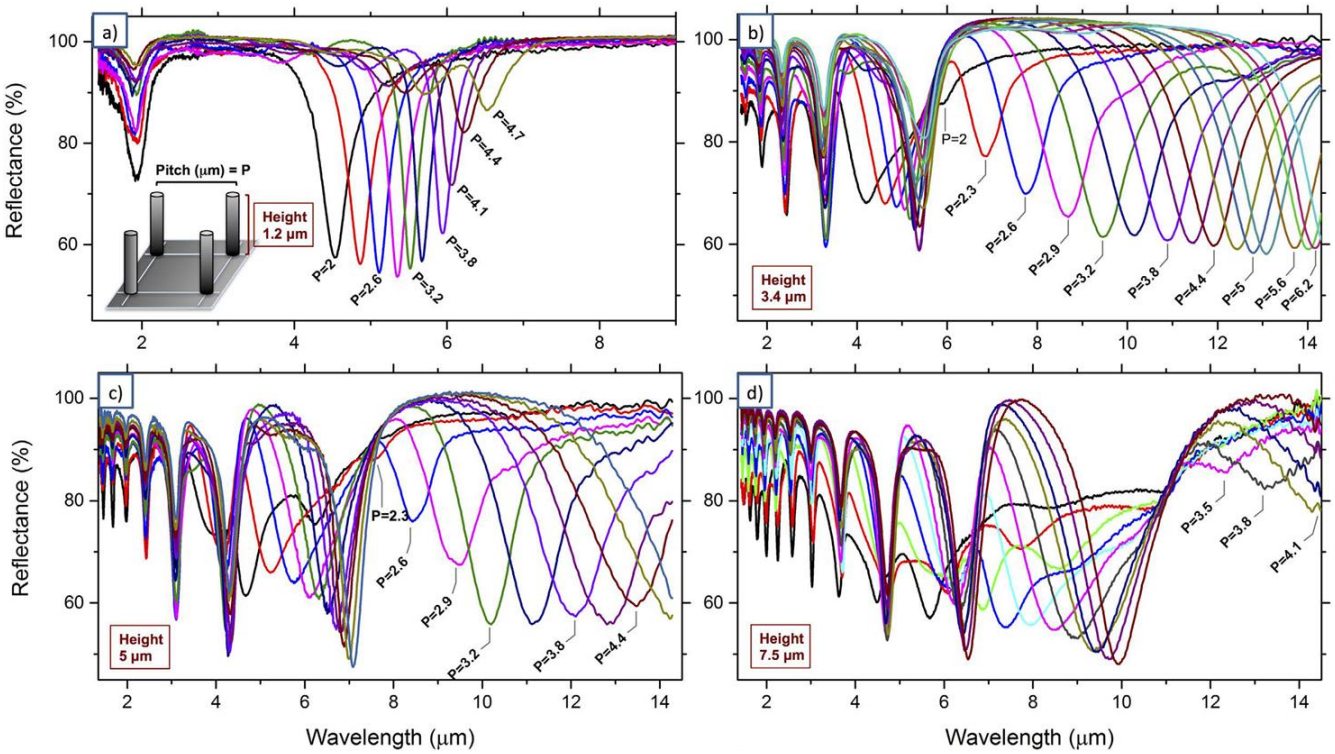


**Figure 2.6: a) – d)** FTIR spectroscopy characterization of ordered arrays of vertical hollow nanotubes, for different heights (h = 1.2 – 3.4 – 5.0 – 7.5 μm) and different inter-antenna distances p. Among the most evident traits of 3D arrays of nanoantennas is the extraordinarily high number of resonance modes.

Associated to the LSPR, there is a resonant enhancement of both the polarizability and the near-field intensity in the vicinity of the nanoparticle[21]. Nanostructures endowed with sharp tip/edges and very

narrow IPS are ideal candidates for nanoscale manipulation of optical energy, promoting nanofocusing and enhancement of electromagnetic radiation in subwavelength regions, the so-called "hot-spots". In this respect, ultra-high resolution fabrication methods as EBL have enabled the realization of planar architectures characterized by local enhancement factors, i.e. defined as the ratio between the near-field intensity and the incident field $E/E_{inc}$, of many orders of magnitude. This capability is an essential requirement for the realization of ultrasensitive devices[33,34], where high hot-spot densities can promote the identification of probe molecules with high contrast and spatial resolution. The hot-spot concept is well exemplified in Figure 2.7, where the case of a planar nanoantenna dimer is shown.

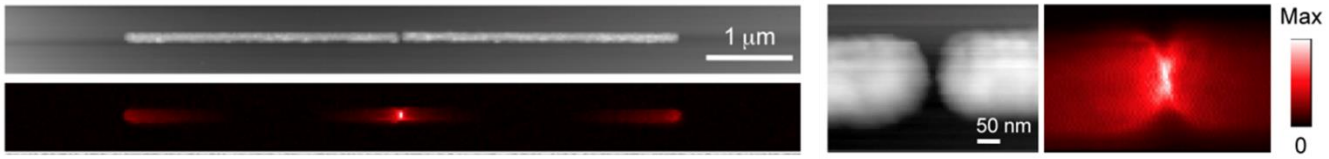


**Figure 2.7:** SEM image and near-field characteristics of a nanoantenna dimer (left). Detail of the nanogap region (right).

As it can be observed stronger electromagnetic enhancement and squeezing is expected in the nanogap region with respect to the dimer edges, thanks to induced in-phase dipole moments that guarantee very good coupling between the neighbouring nanoantennas. This result is further confirmed by the electric field enhancement distribution in the gap area, which shows of the EM field is squeezed in a nanoscale volume much smaller than $\lambda^3$. Thanks to this promising characteristics, the nanogap region can be exploited as a nanocavity region, where light-matter interactions can be strongly boosted, as it is shown in the following chapters.

All the interesting properties presented so far can be employed to enhance strong coupling phenomena at the nanoscale. As it was evidenced in Chapter 1, the strength of the coupling in light-matter interactions can be increased in two ways: by enhancing the dipole moment of the matter part, or by confining light into smaller volumes. Therefore, either very high finesse cavities are required, with non-trivial fabrication issues to overcome, or samples need to be cooled down at cryogenic temperatures and ultrahigh vacuum, in order to decrease the linewidth of the emitters. In the case of surface plasmons, instead, the mode volumes are extremely small since light is intrinsically confined at the nanoscale and the field intensity is enhanced due to the resonant character of SPP excitation. Another important characteristic is that the SPP-emitter conjugated system allows to probe strong

coupling at the nanoscale, in the sense that both the light and matter of the strongly coupled hybrid states can be confined to the nano-level. Thanks to these advantages, it is possible to observe large Rabi splittings in the case of SPP-emitters coupling at ambient conditions (room temperature and atmospheric pressure) and without the need for a closed cavity, thus bypassing the technical limitations of other approaches.

## 2.2 Excitons

Research on semiconductor quantum electrodynamics (QED) can be traced back to 1946, thanks to the pioneering work of E. M. Purcell[35]. The study of atom-vacuum field interactions in cavities and of modified spontaneous emission of molecules have produced numerous interesting results in fundamental science from Bose-Einstein condensates of polaritons[36], to single-photon switches[37] and lasing phenomena[38]. Research in these directions was encouraged by the discoveries made a few years earlier by Frenkel, Peiers and Wannier[39–41] on electronic excitations in crystals, which are still a "hot" topic in today's science. Frenkel and Peiers introduced the concept of *exciton*, a quantum of electronic excitation energy travelling in the periodic structure of a crystal. The exciton can be regarded as a bound state of an electron and an electron hole, attracted to each other by the electrostatic Coulomb force, forming an electrically neutral quasi particle and hence its movement through the crystal gives rise to the transportation of energy without charge. An exciton can form when a quantum of light is absorbed in a semiconductor (solid or molecule): the transferred energy promotes an electron from its closed shell in the valence band to an excited state, leaving behind a vacancy, or in other words a positively charged electron hole. The coupled system can be viewed as an hydrogen atom and the excited electron moves in space influenced by the positive charge field created by its own absence (see Figure 2.8a). Quantum theory predicts that there is not just one but a series of bound stationary states (see Figure 2.8b) and the upper limit of the series is endowed with an energy equivalent to that required to produce a free electron and a hole in the solid.

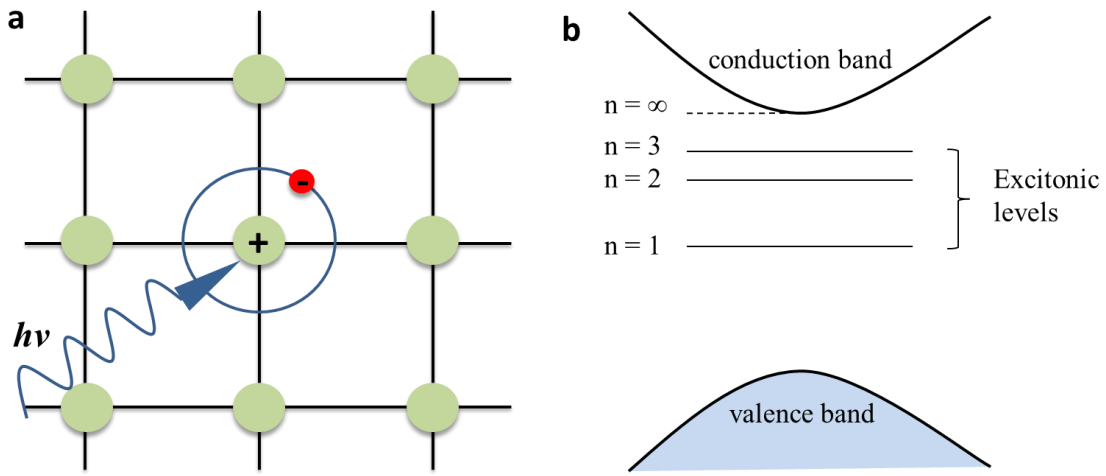


**Figure 2.8: a)** Electron-hole bound state forming in a crystal after absorption of an incident photon of energy $h\nu$. **b)** Energy level scheme of the excitonic bound stationary states.

The corresponding energies are not bound to any particular ion in the lattice, but they are able of passing from one atom to the neighbor and so on through the crystal, constituting what Frenkel called "*excitation waves*" or excitons.

The Coulombic interaction energy between the electron and the hole is simply given by

$$U = -\frac{e^2}{\varepsilon r} \tag{39}$$

where $r$ is their relative distance and ε is the dielectric constant of the surrounding medium, which determines the screening effect on the potential energy of the background atoms and free electrons. For an hydrogen atom in free space ε corresponds to unity, but in solids it can be quite large (of the order of 10 for semiconductors).

Depending on the strength of the Coulomb interaction, we can distinguish between two different kinds of excitons: *Frenkel* and *Mott-Wannier*, which differ physically in their "radii", i.e. in the degree of separation of the electron and hole[42].

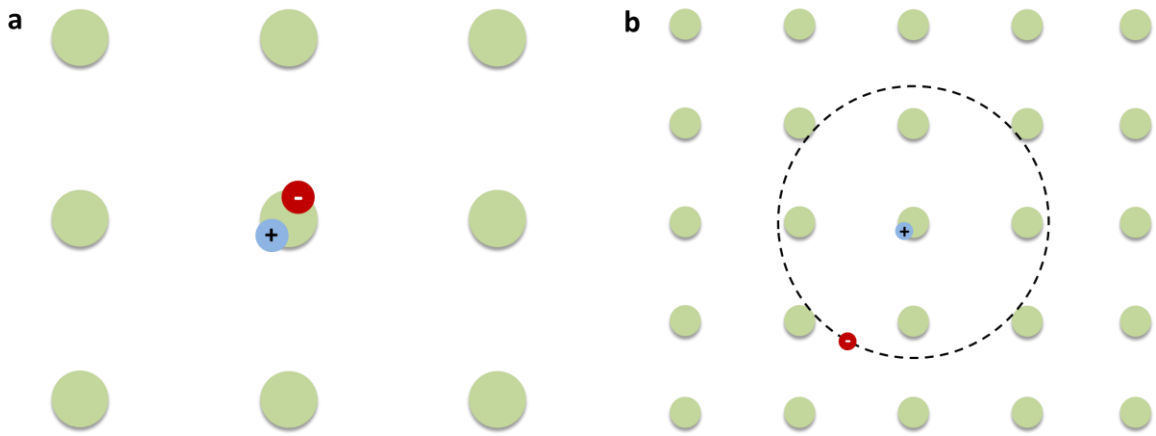


**Figure 2.9: a)** Frenkel exciton highly localized on a crystal lattice site; in this situation the electron feels both the hole and the surrounding lattice potential. **b)** Mott-Wannier exciton with radius extended over few lattice sites; in this situation the electron feels only the hole and an average lattice potential.

In materials with a small dielectric constant, the Coulomb interaction (given by equation 39) between an electron and its corresponding hole can be very strong and the radius of the lowest energy exciton is often comparable or less than the inter-atomic distance (see Figure 2.9a). Consequently, we have a very large potential and a somewhat localized excitation. Being the pair tightly bound, a large amount of energy will be needed to ionize the exciton to produce a free electron and hole. The Frenkel exciton has a typical binding energy of the order of 0.1 to 1 eV and are characteristic of alkali halide crystals and organic molecular crystals, where the constituting molecules are not densely packed.

When the exciton radius is larger than the lattice spacing we are in the Mott-Wannier case (see Figure 2.9b). In this situation the interaction between neighboring atoms is significantly increased and the valence electrons are no longer identifiable with any atom but are usually shared by more than one atom to form bonds. Therefore, the electrons have an increased spatial volume in which they can move, although without being free to contribute to an electric current when the solid is subject to an external electric field. Due to the increased electric field screening, the Coulomb potential energy which binds the electron and hole together is much weaker than the Frenkel exciton case, with binding energies typically of the order of 0.01 eV. Recalling Bohr's quantum theory, we can derive a formula for the energy $E_n$ of the exciton series:

$$E_n = E_\infty - \frac{R}{n^2} \tag{40}$$

where $E_\infty$ is the series limit, $n = 1,2$ ... is a quantum number and $R$ is the binding energy (also known as Rydberg constant). $R$ represents the energy required to ionize an exciton in its lowest energy state, that is the energy separation between the lowest bound state ($n = 1$) and the series limit. Experimentally, these exciton states can be seen as a series of absorption lines, leading up to a continuum in many substances (see Figure 2.10), and constitute one of the main mechanisms for light emission. Mott-Wannier excitons are typical of materials with a relatively large ε, as in the case of many semiconductor crystals, particularly the so-called covalent solids such as germanium, silicon and gallium arsenide.

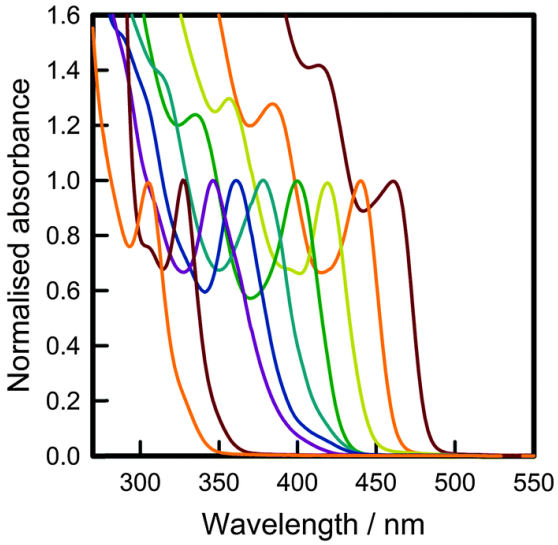


**Figure 2.10:** Absorbance spectra of CdS quantum dots as a function of their diameter. The peaks in the measured curves correspond to different exciton states[43].

There is indeed a third type of exciton known as the *Davydov* exciton[44]. It is found in organic compounds composed of aromatic molecules, such as benzene or anthracene. The aromatic rings can be excited by the absorption of light and the excitation energy can be transferred from one ring to another. Since the interaction between them is small compared to the inter-atomic forces within the ring itself, Davydov excitons are localized and resemble the Frenkel ones.

A particular kind of exciton is found in molecules and is known as molecular exciton[45]. When the absorbed energy corresponds to a transition from one molecular orbital to another one, the resulting electronic excited state can be described as an exciton. Molecular excitons have characteristic lifetimes of nanoseconds, after which the ground electronic state is restored with subsequent photon or phonon emission. FRET between a donor and acceptor molecule (already described in details in chapter 1)

constitutes a special case, in which an exciton may be transferred from one molecule to another.

## 2.3 Plasmon-exciton strong coupling: a classical description

The interaction between surface plasmons and excitons is very similar to the interaction between a cavity resonance and a quantum system (as it was studied in chapter 1), with the cavity mode being replaced by the plasmonic one. When excited quantum emitters are placed in close proximity to a plasmonic element (metallic surface or nanostructure) they can decay towards the ground state following three different channels: energy dissipation through Ohmic losses in the metal (due to roto-vibrational and phononic effects), spontaneous emission of photons into the far-field or energy transfer into radiative and non-radiative surface plasmon polariton modes of the metal. In the latter case, as in the atom-cavity picture, a change in the radiative decay rate of the emitter is observed, if the two systems are only weakly coupled. If, instead, the energy exchange rate in the "plasmonic channel" exceeds the dissipation rates of the other mechanisms, then mixed hybrid states are formed bearing significantly different optical properties from the initial constituents.

In the following, we will employ a classical approach to theoretically illustrate strong coupling between SPPs and emitters[46] and we will assume that the dielectric environment in the vicinity of the plasmonic structure contains emitters with a well-defined absorption/emission spectrum. Whenever the frequency of the SPP overlaps with a transition frequency ($\omega_0$) of the emitters, their absorption will hinder the propagation of the plasmon mode. The emitters in the medium will be considered as classical Lorentzian oscillators, which well suits the case of molecules, atoms or quantum dots located near the metal surface, so that they can be described by the dynamics of an electron of charge *e* and mass *m*. The electron of the molecule/emitter can be thought as an harmonically bound, damped oscillator driven by the field $E(r,t)$. The equation of motion of such a system (1D for simplicity) is:

$$m(\ddot{r} + \gamma\dot{r} + \omega_0^2 r) = -eE(r,t) \tag{41}$$

where $\omega_0$ is the frequency of the harmonic oscillator and γ describes the damping. Within the dipole approximation, the field can be assumed to be constant in the *r* coordinate, since the electron movement is much smaller than the wavelength of the radiation.

Assuming a harmonic EM field, i.e. $E(r,t) = E_0 e^{i\omega t}$, the steady-state solution of equation (41) becomes

$$r = -\frac{e}{m}\frac{1}{\omega_0^2 - \omega^2 - i\gamma\omega}E_0 e^{i\omega t} \tag{42}$$

Being the dipole moment of the electron simply $p = -er$, in the case of N emitters (and corresponding dipole moments) the macroscopic polarization density $P$ is defined as the average dipole moment per unit volume (V), and it can be written as

$$P = \frac{Ne^2}{Vm}\frac{1}{\omega_0^2 - \omega^2 - i\gamma\omega}E_0 e^{i\omega t} \tag{43}$$

where $N/V$ is the number density of dipole moments. The macroscopic polarization is also defined in terms of the electric susceptibility $\chi$ as $P = \varepsilon_0 \chi E$; by inserting this equation into (43) we can find a formula for the macroscopic electric susceptibility as a function of the radiation wavelength

$$\chi(\omega) = \frac{Ne^2}{V\varepsilon_0 m}\frac{1}{\omega_0^2 - \omega^2 - i\gamma\omega} \tag{44}$$

The imaginary part of the susceptibility describes dissipation and gives the absorption coefficient of the material. The permittivity of the material is related to the susceptibility through $\varepsilon(\omega) = 1 + \chi(\omega)$ and will therefore have real and imaginary parts $\varepsilon'$ and $\varepsilon''$ respectively

$$\varepsilon' = n^2 - \kappa^2, \quad \varepsilon'' = 2n\kappa \tag{45}$$

where n and κ are the refractive index real and imaginary parts. Up to now, we have considered only the molecular part of our system and we therefore need to introduce the plasmonic element (in the following, the permittivities of the metal and the dielectric/emitters will be referred as $\varepsilon_1$ and $\varepsilon_2$, respectively). In order to do so, we recall back the SPP dispersion relation (35) given in section 2.1 and assume that we are far away from the plasma frequency of the metal. In this limit, the permittivity of the metal ($\varepsilon_1$) can be considered to be constant. Moreover, we assume $\varepsilon_1$ to be negative and relatively

large in absolute value (which typically suits well for metals) so that the term $\varepsilon_1 + \varepsilon_2$ in the dispersion always stays negative, even when the permittivity $\varepsilon_2$ of the emitters is large and positive. Based on these considerations, the dispersion can be written as[46]

$$k_{SPP}^2 = \frac{\omega^2}{c^2}\frac{|\varepsilon_1|}{|\varepsilon_1 + \varepsilon_2|}(1 + \chi(\omega)) \tag{46}$$

By rescaling the momentum to $\kappa^2 = k_{SPP}^2 \frac{|\varepsilon_1+\varepsilon_2|c^2}{|\varepsilon_1|}$, we obtain

$$\kappa^2 = \omega^2(1 + \chi(\omega)) = \omega^2\left(1 + \frac{\mathrm{g}^2}{\omega_0^2 - \omega^2 - i\gamma\omega}\right) \tag{47}$$

where g is the system coupling strength defined as $\mathrm{g}^2 = \frac{Ne^2}{V\varepsilon_0 m}$. In the case of $\kappa \sim \omega_0$ and $\gamma = 0$ (i.e. close to resonance and no damping) the above equation becomes

$$(\kappa - \omega)(\omega_0 - \omega) = \frac{\mathrm{g}^2}{4} \tag{48}$$

The solutions for this equations are the two hybrid normal modes of the coupled system (see Figure 2.11 for the level scheme), and if we substitute κ with the metal plasmon resonance $\omega_{pl}$ and insert the detuning $\delta = \omega_{pl} - \omega_0$, we obtain the plasmon-excitons branches usually found in literature[47,48]

$$\omega_\pm = \frac{\omega_{pl}}{2} + \frac{\omega_0}{2} \pm \frac{1}{2}\sqrt{4\mathrm{g}^2 + \delta^2} \tag{49}$$

and shown in Figure 2.12.

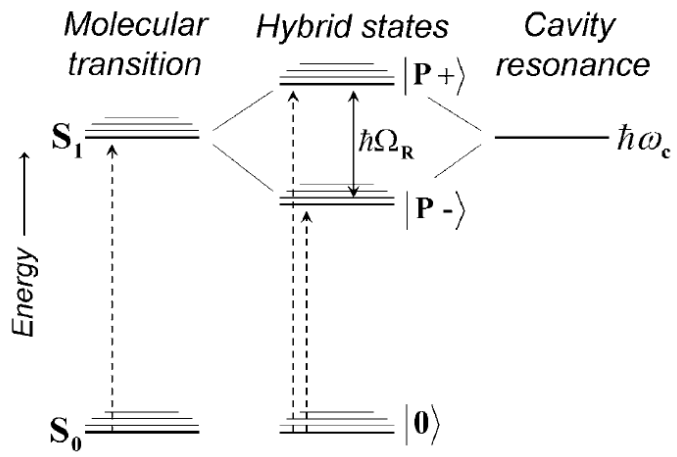


**Figure 2.11:** Simplified energy landscape showing the interaction between a molecular transition and a plasmonic cavity mode. When energy exchange is rapid compared to energy loss, strong coupling leads to the formation of two hybrid light-matter (polaritonic) states, separated by the Rabi splitting energy $\hbar\Omega_R$**.** Moreover, the absolute energy of the ground level of the coupled system $|0\rangle$ may also be modified by strong coupling.

At resonance, when the plasmon mode exactly matches the absorption transition of the emitters ($\omega_{pl} = \omega_0$) the normal mode splitting is given by

$$\Omega_R = 2\mathrm{g} = \sqrt{\frac{N}{V}}\frac{e}{\sqrt{\varepsilon_0 m}} \tag{50}$$

which retrieves the emitter concentration dependence found in the semi-classical and quantum descriptions for the general case of an atom-cavity system (see chapter 1).

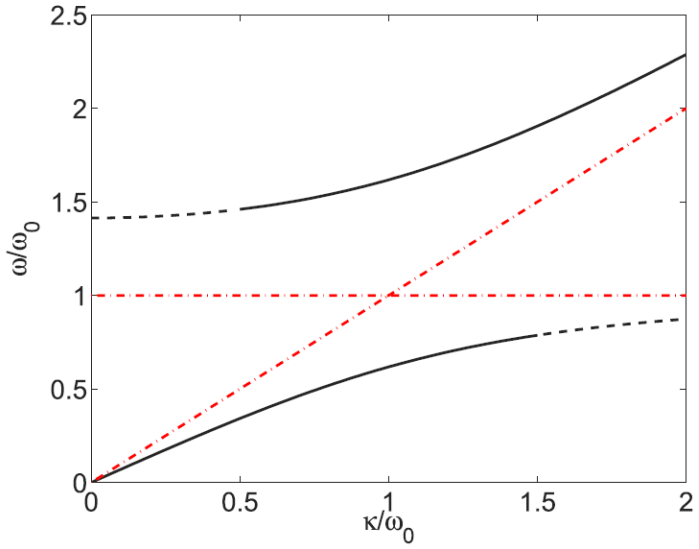

**Figure 2.12:** The dispersion of an SPP-emitter system given by equation (47). The black curves are the polariton branches, while the red dotted lines are the emitter transition frequency (horizontal line) and the SPP dispersion (diagonal line) for $g = 0$, i.e. no coupling[46].

The only difference here with respect to the quantum case is the missing dependence on the cavity (plasmon) field energy $\hbar\omega$ and the emitters dipole moment, which are derived from a quantum mechanical description of a two-level system. In the quantum case in fact, the vacuum Rabi splitting in zero-photon conditions becomes

$$\hbar\Omega_R = 2\mu\sqrt{\frac{\hbar\omega}{2\varepsilon_0 V}} \tag{51}$$

## 2.4 Plasmon-exciton strong coupling: state-of-the-art

Owing to the nanoscale characteristics of surface plasmons and the easy tunability of their plasmonic resonance, strong coupling between SPPs and excitons has recently become an active topic of research. Many different excitonic systems have been addressed so far and strong coupling has been attained with J-aggregates[49,50], dye molecules[51,52], and quantum dots[53,54], to cite just a few.

As already anticipated in section 2.1 of this chapter and evidenced by equation (51), the strength of the coupling between matter (excitonic system) and light (SPP mode) can be increased in two ways: by increasing the dipole moment $\mu$ of the emitter, or by decreasing the modal volume *V*. SPPs mode volumes are extremely small, if compared to semiconductor microcavities, due to their intrinsic nanoscale confinement properties. Moreover, relatively large dipole moments can be achieved by using high concentrations of optically active material, as it is the case of cyanine-based J-aggregates. These aggregates are self-organized molecular crystals and have partially delocalized excitons with relatively narrow absorption bands (with an associated strong dipole moment) compared to that of the corresponding dye monomer (see Figure 2.13a). The high oscillator strength of J-aggregates results from coherent interaction between the dipole moments associated with many molecular units, providing an effective "super moment"[46].

These advantages have been exploited by Bellessa et al.[50] to investigate strong coupling between the SP mode of a planar silver film and the exciton of TDBC J-aggregated molecules spin-coated on top of the metal layer, finding very large Rabi splittings (180 meV, about 8% of the hybridized transition

frequency) at room temperature. Reflectometry spectra, performed in Kretschmann geometry as a function of the incident light angle (see Figure 2.13c), showed the arising of two hybrid energy bands at the sides of the uncoupled absorption line, a clear signature of strongly coupled systems. These findings were furtherly corroborated by the characteristic anticrossing behavior of the polariton energies dispersion, as it can be observed in Figure 2.13b. Far from the resonance condition, the reflectometry dip position is close to the uncoupled plasmon energy, thus highlighting a totally unmixed plasmonic nature. At resonance instead, i.e. when the uncoupled SP mode has the same energy of the exciton, the plasmon and the exciton contributions cannot be separated anymore and the two dips correspond to the plasmon-exciton mixed states. In addition to this, the authors demonstrated the modification of the J-aggregate luminescence upon realization of strong coupling (see Figure 2.13d). Luminescence spectra acquired for different detection angles feature two emission maxima: the high energy peak (close to the exciting laser line) is due to luminescence of the J-aggregates into radiative modes, while the luminescence peak with lower energy can be ascribed to the emission of the low energy exciton-plasmon polariton. The high energy polariton state is not present in the luminescence spectra as a result of relaxation towards uncoupled excitonic states.

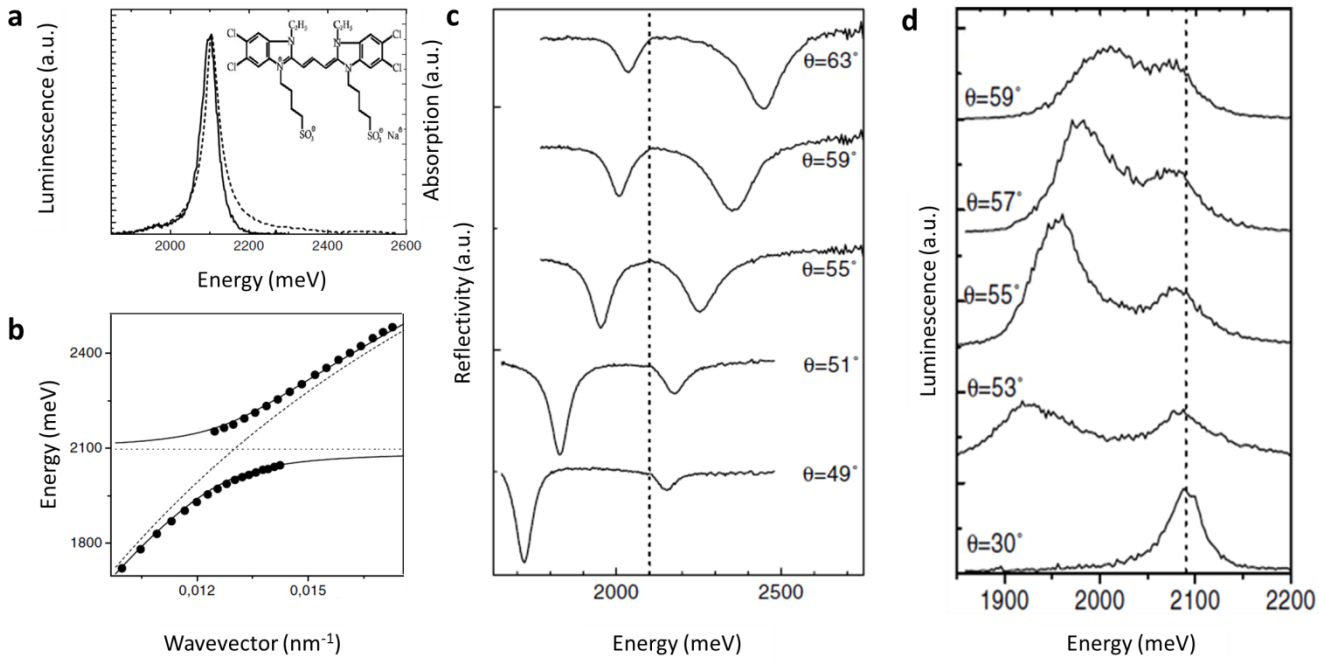


**Figure 2.13: a)** Luminescence spectrum (continuous line) and absorption (dashed line) of TDBC J-aggregates inserted in a PVA matrix. The inset shows the chemical formula of TDBC. **b)** Measured reflectometry dips energy (black dots) as a function of the incident wavevector. The dashed horizontal line is the TDBC exciton energy, while the diagonal one is the

dispersion relation of an uncoupled SP. **c)** Reflectometry spectra for different angles as a function of the incident light energy. **d)** Luminescence spectra recorded for different detection angles.

Later works directed their attention from the spectral response of plasmonic-emitter systems to the investigation of the dynamical behavior. The primary method of probing the dynamics of many photo-physical systems relies on transient absorption spectroscopy, as demonstrated by Vasa et al.[55] on J-aggregate layers deposited onto gold gratings. In this work, they observed temporal oscillations in their measured differential reflectivity ($\Delta R/R$) spectra (see Figure 2.14), which can be directly attributed to Rabi oscillations of the hybrid system, as a result of the periodic emission and reabsorption of photons between the upper and lower polariton states. Because of the large value of the normal mode splitting observed (~ 200 meV), the energy exchange occurs with a Rabi period of $T_R \approx 2\pi/\Omega_R$ which, in the present case, corresponds to a short timescale of ~ 30 fs. The major challenge in observing these oscillations is due to the short decay times of plasmon modes (~ 100 fs) and Rabi oscillations times thus have to be even shorter if they are to be observed. Thanks to the high oscillator strength of J-aggregates, large splittings can be achieved in such systems allowing temporal resolution of the Rabi oscillations against the plasmon decay.

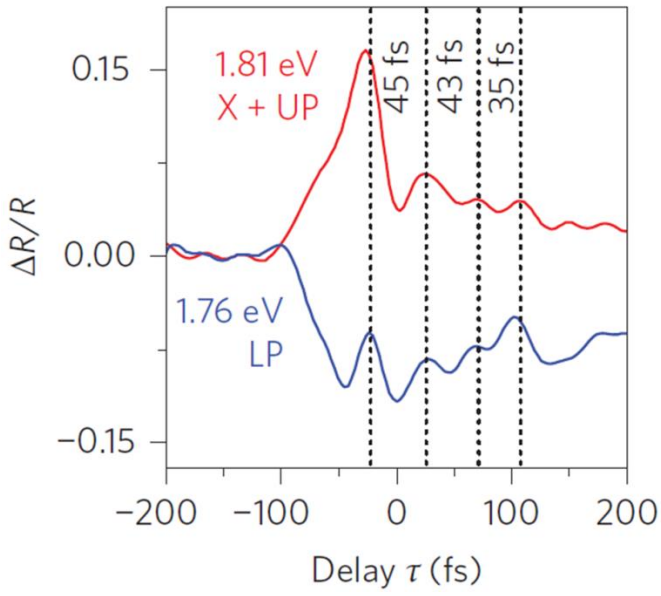


**Figure 2.14:** Time evolution of $\Delta R/R$ at the lower polariton LP resonance at 1.76 eV (blue line) and near the overlapping upper polariton UP and bare J-aggregates resonances at 1.81 eV (red line) showing Rabi oscillation with a $T_R$ ~ 45 fs.

In recent years, there has been a great deal of effort towards understanding the dynamics of strongly coupled systems by transient spectroscopy measurements. It has been demonstrated that the lifetime of lower and the upper hybrid bands in exciton-SPP systems can be much longer than the life of bare excited molecules. In the latter case, it was suggested that this result can be caused by the existence of a trap state[56] or by the blockage of the vibrational relaxation modes due to the large Rabi splitting in such systems[57].

Employing a hybrid structure of gold nanoholes arrays covered with J-aggregate molecules in a PVA matrix, Dintinger[58] and Wang[49,59] in a similar work, verified the $\sqrt{N/V}$ dependence of the Rabi splitting and demonstrated a reduced lifetime of the upper hybrid band upon increasing of the coupling strength. Periodic metallic hole arrays have the capability to convert incident radiation into SPPs modes, which are characterized by a remarkable field confinement at the metallic surface. The desired SPP mode can be chosen by accurately tuning the nanoholes period thus to overlap the absorbance peak of the J-aggregates and maximize the coupling strength. By increasing the thickness of the J-aggregate layer, they were able to experimentally measure a Rabi splitting of 245 meV at the resonance period of 310 nm. In Figure 2.15a, is highlighted the behavior of the hybrid polariton energy separation displaying a linear dependence on the square root of the J-aggregates absorbance which, in turn, depends on molecule concentration. Thus, the Rabi splitting observed in the transmission spectra follows a $\sqrt{N/V}$ dependence, in accordance with previous experimental results and the theoretical/numerical descriptions of strong coupling (see chapter 1).

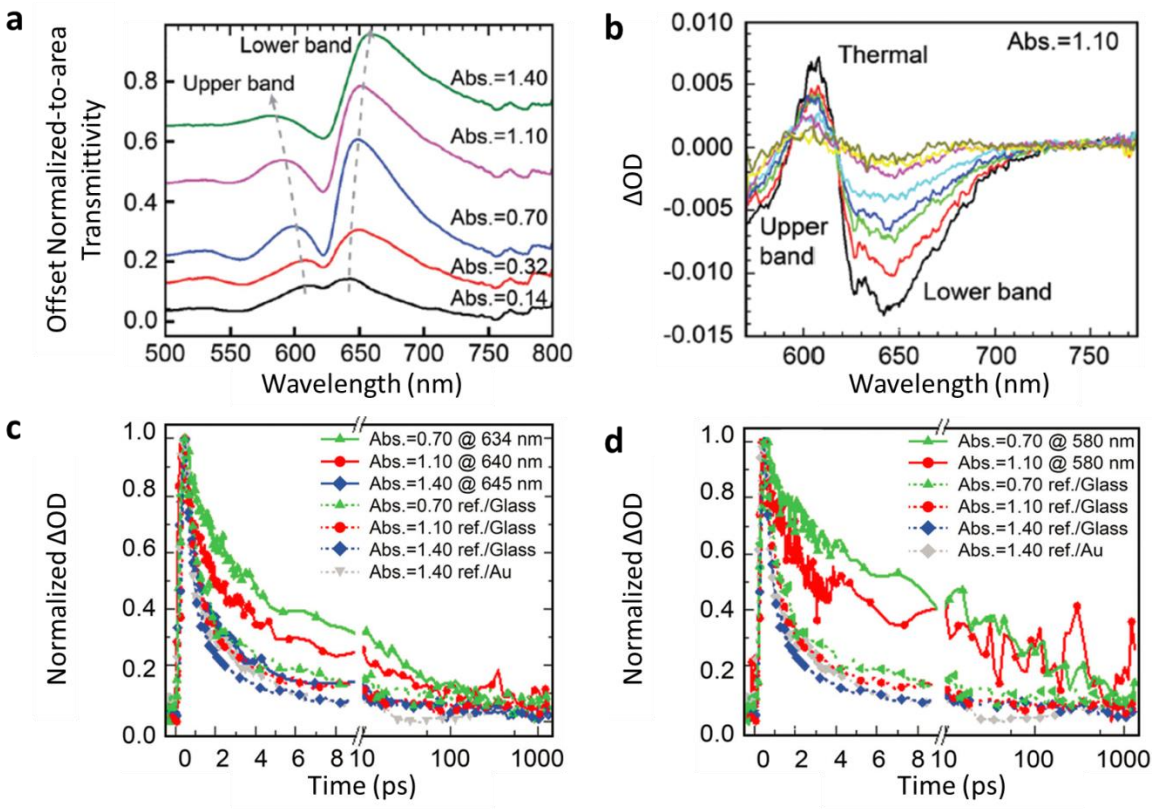


**Figure 2.15: a)** Experimental transmission spectra of gold hole arrays (period = 310 nm) upon increasing of J-aggregate concentration (absorbance from 0.14 to 1.40 measured at 623 nm). **b)** Transient absorption spectra of PVA/J-aggregates, corresponding to absorbance of 1.10 and deposited on a gold holes array under 560 nm excitation, recorded at different times. **c)** Lower and **d)** upper hybrid bands normalized bleaching dynamics of different J-aggregates concentrations in comparison with reference samples.

Femtosecond transient absorption (TA) spectroscopy was carried out to investigate the dynamics of the hybrid bands. In TA experiments, Wang et al. measured the variation of the optical density $\Delta OD$, defined as $-\log\left(I(\lambda)_{pumped}/I(\lambda)_{unpumped}\right)$, that is the logarithm of the ratio between the intensity of the probe beam of a "pumped" (i.e. after the excitation beam has hit the sample) and "unpumped" (i.e. no excitation employed) sample measured by the detector. In Figure 2.15b, transient spectra for the J-aggregate concentration corresponding to an absorbance of 1.10 are shown. In the measured spectra acquired for laser excitation at 560nm (corresponding to the upper band spectral position) two bleaching signals arise, with the upper band strongly blue-shifted and almost out of the detection window as a result of the large Rabi splitting. Between the two bleaching minima a positive excited state absorption signal, associated to thermal effects[60], is observed. Indeed, in the present configuration

the resonant pump laser brings the system to an excited configuration where the energy is shared and oscillates between the hybrid modes associated with the gold nanoholes and the J-aggregates.
The kinetics of the lower (Figure 2.15c) and upper (Figure 2.15d) hybrid bands with different coupling strengths (i.e. J-aggregate concentration) were compared with the kinetics of J-aggregates on a flat glass substrate and a flat gold film. The reported results show that the hybrid bands have longer lifetimes than the bleaching recovery of J-aggregates on bare substrates and the kinetics of the exciton-SPP state is significantly affected by the molecule concentration. The longer lifetime with respect to the uncoupled case can be explained in terms of a bottleneck relaxation mechanism[61]. Moreover, the lifetime of both hybrid bands is reduced by increasing the coupling strength differently from the behavior of J-aggregates on a flat gold film, where no dependence on the concentration was detected.

If we now go back at section 2.3 and look at equation (50) we can obtain a condition to clearly observe strong coupling

$$\frac{Ne^2}{V\varepsilon_0 m} > \frac{\gamma^2}{2} + \frac{\gamma_{SPP}^2}{2} \tag{52}$$

which states that the linewidths of the absorption/emission resonance and the optical/plasmonic mode should be smaller than the coupling strength. One would thus anticipate that strong coupling is possible only for molecules with a narrow absorption spectrum, such as J-aggregates. However, strong coupling was also observed between SPPs and molecules with a broader absorption spectrum, as it is the case of Rhodamine 6G[51] or methylene-blue dyes[62].
In the latter case, Chikkaraddy et al.[62] achieved few to single-molecule strong coupling at room temperature by designing plasmonic nanocavities with extremely low modal volumes (down to some tens of cubic nanometers), paving the way for the realization of quantum information systems and ultralow-power switches and lasers. In order to obtain such results they employed the nanoparticle-on-mirror (NPoM) geometry, placing the emitters in the gap region between nanoparticles and an underlying flat metallic film (see Figure 2.16a) and accurately controlling the nanogap size to a sub-nanometer scale using molecular spacers. To avoid random aggregation of dye molecules in the gaps, they exploited the host-guest chemistry of macrocyclic cucurbit[*n*]uril molecules, which are characterized by varying hollow internal volumes (depending by the number *n* of units in their ring) in which methylene-blue guest molecules can sit[63]. In this respect, they employed cucurbit[7]uril, which can host only one guest molecule. When gold nanoparticles bind on top of a cucurbit[*n*]uril monolayer

filled with methylene-blue molecules as in Figure 2.16a, two scattering peaks at either side of the absorption ($\omega_0$) of uncoupled methylene appear in the dark-field spectra (see Figure 2.16b). These new features in the measured spectra correspond to the formation of hybrid plasmon-exciton branches $\omega_{\pm} = \omega_0 \pm g/2$, yielding in this specific case a maximum Rabi frequency of $g = 300$ meV. By changing the ratio of methylene-blue to cucurbit[7]uril they were able to systematically tune the number of molecules in the nanogap region, down to the single-molecule level, and measure the corresponding Rabi splitting in each specific case, verifying the $N/V$ law (see Figure 2.16c).

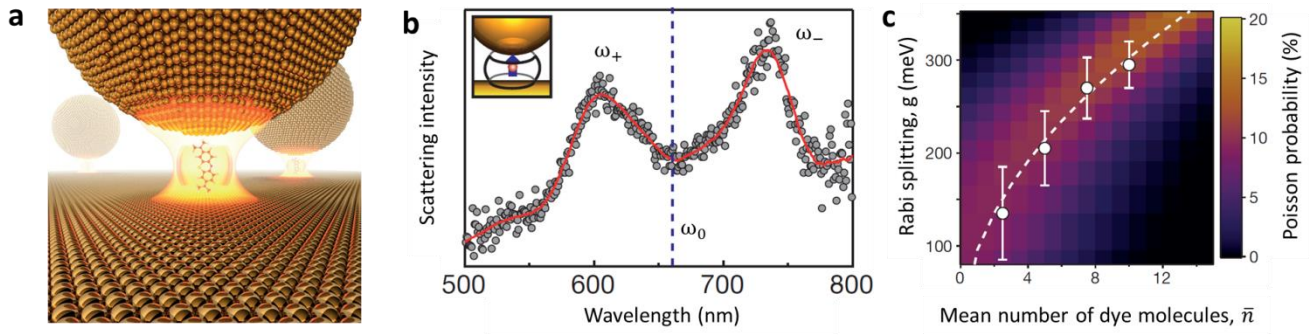


**Figure 2.16: a)** Illustration of a methylene-blue molecule in cucurbit[$n$]uril, in the nanoparticle-on-mirror geometry. **b)** Scattering spectrum resulting from isolated NPoMs; strong coupling between the emitter and the plasmon gives rise to hybrid peaks at either side of the methylene blue absorption frequency. **c)** Energy of Rabi oscillations (g) versus mean number of dye molecules ($\bar{n}$). Experimental points and error bars are shown and follow the theoretical curve (dashed line). The colors represent the Poisson probability distribution of $\bar{n}$.

The advantages of plasmon based devices were also exploited by Gómez et al.[53] to realize strong coupling between SPs propagating on a planar silver thin film and the lowest excited state of CdSe semiconductor nanocrystals deposited on top of it. Due to the quantum size effect, the optical properties of these nanocrystals (also called quantum dots, QDs) are different from those of their bulk counterparts, leading to interesting phenomena such as size-dependent photoluminescence. In QDs, photoluminescence comes from radiative exciton annihilation (electron-hole recombination), an irreversible process which competes with non-radiative decay channels that deteriorate the performance of the nanocrystals. One approach to overcome these drawbacks consists of coupling the QDs to electromagnetic radiation (through a cavity or a plasmon mode), thus modifying the energy spectrum of the QDs and leading to enhancement or suppression of radiative decay pathways.

In the present case[53], coupling of excitons in the QDs with the SPs of the silver film is mediated via a dipole interaction, which arises between the electric field produced in the CdSe by the SP and the

electric dipole moment of the exciton transition. Attenuated total reflection measurements in the Kretschmann-Raether configuration show the appearance of two reflectivity minima in the spectra, as a result of a reversible energy exchange between the SP mode at the Ag/CdSe interface and the exciton transition in the CdSe QDs (see Figure 2.17a). A further evidence of the strong interaction was given in the reconstruction of the dispersion curves for the hybrid bands, which shows the characteristic anticrossing behavior of strongly coupled systems (see Figure 2.17b).

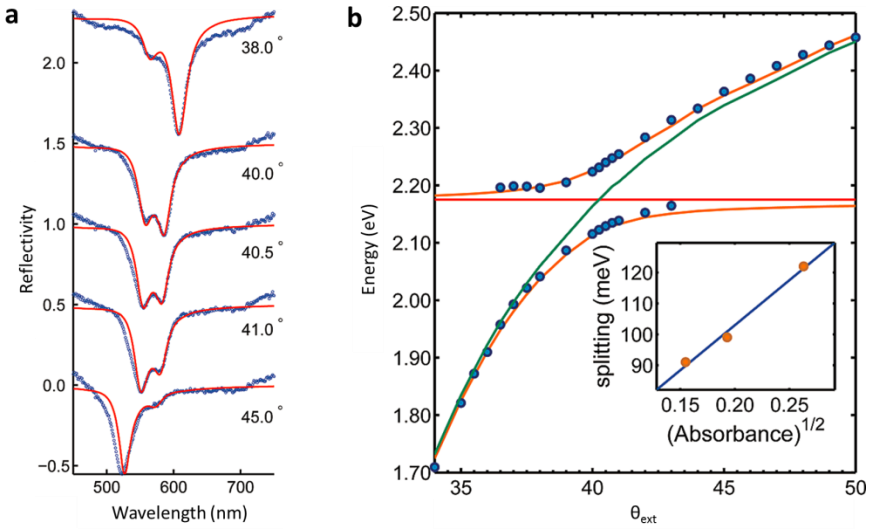


**Figure 2.17: a)** Experimental reflectivity curves of p-polarized white light measured at different incident angles. **b)** Experimental dispersion curve. The points originate from the minima in the reflectivity measurements and are plotted against the external angle of incidence. The horizontal red line is the energy of the uncoupled exciton, while the green line is the energy of the uncoupled SP. The inset is a plot of the upper-lower polariton branch splitting vs the square root of the absorbance of the exciton.

All the interesting features of plasmon-exciton hybrid systems presented so far, have been extensively exploited for a variety of applications. The strong modification of the energy levels has been used to modify chemical reaction rates[64] and the work function, the energy necessary to remove an electron from the Fermi level into vacuum, of organic materials[65]. In the former, Hutchison et al.[64] were able to influence a chemical reaction by strongly coupling the energy landscape governing the reaction pathway to electromagnetic vacuum fields. In this respect, they employed spiropyran photochromic molecules, which undergo photoisomerization to merocyanine upon UV irradiation, in a plasmonic cavity composed of two opposite Ag metal films and resonant with the molecular transition investigated. Interestingly, during UV exposure, they observed a slower photoisomerization rate for the

molecules embedded in the cavity structure, with respect to uncoupled molecules. This retardation corresponds to the onset of strong coupling conditions and the formation of hybrid light-matter states which influence the reaction pathways. In a following work, Hutchison et al.[65] demonstrated modification of the work-function of photochromes, which affects the performance of electronic devices, such as organic transistors and solar cells. As in the previous work spiropyran was employed as photochromic molecule, while the plasmonic structure was represented by a hole-array resonant with the molecular transition. By means of Kelvin Probe Method (KPM) technique, which is routinely used to measure surface potential differences $\Delta SP$ (directly related to changes in the work-function), they obtained very big shifts in $\Delta SP$ reaching a maximum when the hole-array surface plasmon mode was matching the investigated transition, i.e. when the system was most strongly coupled with the electromagnetic vacuum field.

Exploiting a similar design (hexagonal hole arrays milled in Ag or Al metal film), Orgiu et al.[66] investigated the effect of strong coupling on the conductivity of organic semiconductors, which have generated considerable interest in their potential application for large scale and flexible devices[67,68]. In their work hybridization is achieved between the molecular transition of aromatic diimide molecules and the plasmonic modes supported by the subwavelength hole-arrays (see Figure 2.18a). These organic compounds exhibit strong absorption bands that can be efficiently coupled to surface plasmon resonances. Current-voltage (I-V) curves were measured for thin semiconductor films between patterned electrodes and were compared to the response of molecules on planar electrodes. As shown in Figure 2.18b, at the intersection of the molecular absorption and the plasmon modes of the hole-array, i.e. where strong coupling occurs, a resonance in the measured currents is clearly visible, reaching values one order of magnitude greater than in the reference or uncoupled case. This behaviour corresponds to carrier injection from the metal electrodes to the hybridized coherent states of the molecules ($\sim 10^5$ oscillators involved), resulting in enhanced conductivity of the material.

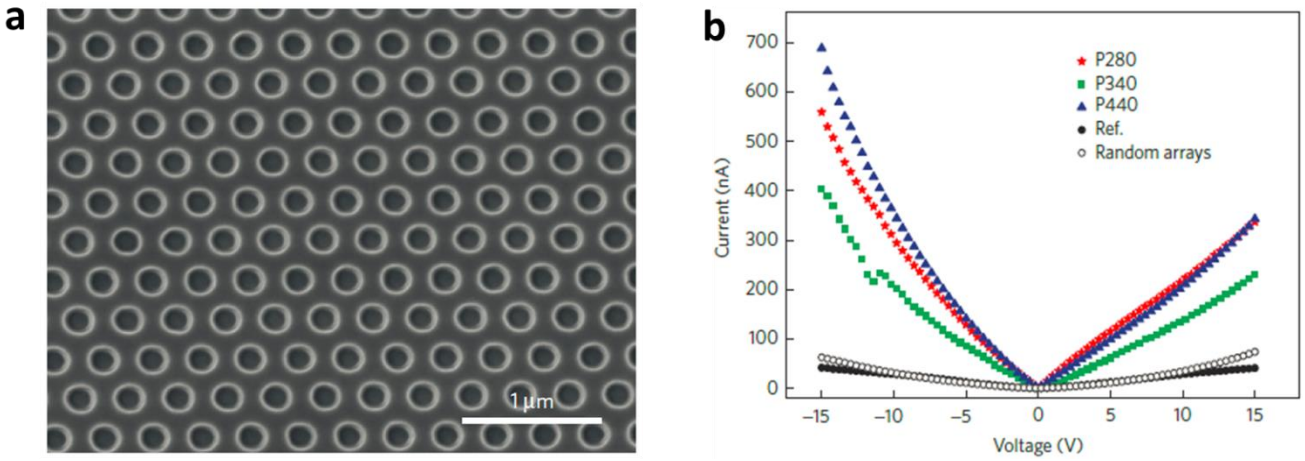


**Figure 2.18: a)** SEM image of an hexagonal array of holes milled in a Al metal film providing the plasmon resonance that is strongly coupled to the molecule. **b)** I-V curves as a function of the hexagonal array at selected periods.

Moreover, due to the bosonic characters of the polariton states, non-equilibrium Bose-Einstein condensation has been observed at room temperature[36] paving the way towards the realization of groundbreaking nano-plasmonic devices, such as all-optical switches[37], low threshold nano-lasers[69] and single-photon optical transistors[70]. SPP-excitons strong coupling was also employed to increase the Raman signal of organic dyes[71], to modify the luminescence spectrum of J-aggregates[50] (presented in detail above) and to enhance the excitation rate and the fluorescence intensity of semiconductor QDs, thus offering the possibility to boost the performance of organic LEDs[72]. Despite the great amount of applications, research in this field is still at an embryonic stage. Further advances in nanofabrication techniques could unveil the quantum origin of strong coupling in plasmonics and improve our understanding of this phenomenon, thus indicating future directions and challenges.

## References

[1] Adato, R.., Altug, H., "In-situ ultra-sensitive infrared absorption spectroscopy of biomolecule interactions in real time with plasmonic nanoantennas," Nat. Commun. **4**, 2154, Nature Pub. Group (2013).

[2] Gopalakrishnan, A., Chirumamilla, M., De Angelis, F., Toma, A., Zaccaria, R. P.., Krahne, R., "Bimetallic 3D nanostar dimers in ring cavities: recyclable and robust surface-enhanced Raman scattering substrates for signal detection from few molecules.," ACS Nano **8**(8), 7986–7994

(2014).

[3] Hao, F., Sonnefraud, Y., Dorpe, P. Van., Maier, S. A., Halas, N. J.., Nordlander, P., "Symmetry Breaking in Plasmonic Nanocavities: Subradiant LSPR Sensing and a Tunable Fano Resonance," Nano Lett. **8**(11), 3983–3988 (2008).

[4] Prodan, E., Radloff, C., Halas, N. J.., Nordlander, P., "A hybridization model for the plasmon response of complex nanostructures.," Science **302**(5644), 419–422, American Association for the Advancement of Science (2003).

[5] Boltasseva, A.., Atwater, H. A., "Materials science. Low-loss plasmonic metamaterials.," Science **331**(6015), 290–291, American Association for the Advancement of Science (2011).

[6] Zhang, S., Genov, D. A., Wang, Y., Liu, M.., Zhang, X., "Plasmon-Induced Transparency in Metamaterials," Phys. Rev. Lett. **101**(4), 47401, American Physical Society (2008).

[7] Bauch, M., Toma, K., Toma, M., Zhang, Q.., Dostalek, J., "Plasmon-Enhanced Fluorescence Biosensors: a Review," Plasmonics **9**(4), 781–799 (2014).

[8] Cetin, A. E.., Altug, H., "Fano Resonant Ring/Disk Plasmonic Nanocavities on Conducting Substrates for Advanced Biosensing," ACS Nano **6**(11), 9989–9995 (2012).

[9] Zhou, W., Dridi, M., Suh, J. Y., Kim, C. H., Co, D. T., Wasielewski, M. R., Schatz, G. C.., Odom, T. W., "Lasing action in strongly coupled plasmonic nanocavity arrays," Nat. Nanotechnol. **8**, 506, Nature Publishing Group (2013).

[10] Yang, A., Hoang, T. B., Dridi, M., Deeb, C., Mikkelsen, M. H., Schatz, G. C.., Odom, T. W., "Real-time tunable lasing from plasmonic nanocavity arrays," Nat. Commun. **6** (2015).

[11] Barnes, W. L., Dereux, A.., Ebbesen, T. W., "Surface plasmon subwavelength optics," Nature **424**, 824, Nature Publishing Group (2003).

[12] Celebrano, M., Wu, X., Baselli, M., Großmann, S., Biagioni, P., Locatelli, A., De Angelis, C., Cerullo, G., Osellame, R., et al., "Mode matching in multiresonant plasmonic nanoantennas for enhanced second harmonic generation," Nat. Nanotechnol. **10**, 412, Nature Publishing Group (2015).

[13] Tame, M. S., McEnery, K. R., Özdemir, Ş. K., Lee, J., Maier, S. A.., Kim, M. S., "Quantum plasmonics," Nat. Phys. **9**, 329, Nature Publishing Group (2013).

[14] Jacob, Z.., Shalaev, V. M., "Physics. Plasmonics goes quantum.," Science **334**(6055), 463–464, American Association for the Advancement of Science (2011).

[15] Maier, S. A., Plasmonics: fundamentals and applications (2007).

[16] Klimov, V., Nanoplasmonics (2014).

[17] Kretschmann, E.., Raether, H., "Radiative decay of non radiative surface plasmons excited by light," Zeitschrift für Naturforsch. A **23**(12), 2135–2136 (1968).

[18] Otto, A., "Excitation of nonradiative surface plasma waves in silver by the method of frustrated total reflection," Zeitschrift für Phys. A Hadron. Nucl. **216**(4), 398–410 (1968).

[19] Hecht, B., Bielefeldt, H., Novotny, L., Inouye, Y.., Pohl, D. W., "Local Excitation, Scattering, and Interference of Surface Plasmons," Phys. Rev. Lett. **77**(9), 1889–1892, American Physical Society (1996).

[20] Park, S., Lee, G., Song, S. H., Oh, C. H.., Kim, P. S., "Resonant coupling of surface plasmons to radiation modes by use of dielectric gratings," Opt. Lett. **28**(20), 1870–1872, OSA (2003).

[21] Bohren, C. F.., Huffmann, D. R., Absorption and scattering of light by small particles, 1st editio, John Wiley and Sons (1983).

[22] Biagioni, P., Huang, J.-S.., Hecht, B., "Nanoantennas for visible and infrared radiation," Reports Prog. Phys. **75**(2), 24402 (2012).

[23] Atwater, H. A.., Polman, A., "Plasmonics for improved photovoltaic devices," [Materials for Sustainable Energy], 1–11.

[24] Ozbay, E., "Plasmonics: merging photonics and electronics at nanoscale dimensions.," Science **311**(5758), 189–193, American Association for the Advancement of Science (2006).

[25] Ju, L., Geng, B., Horng, J., Girit, C., Martin, M., Hao, Z., Bechtel, H. A., Liang, X., Zettl, A., et al., "Graphene plasmonics for tunable terahertz metamaterials," Nat. Nanotechnol. **6**, 630, Nature Publishing Group (2011).

[26] De Angelis, F., Malerba, M., Patrini, M., Miele, E., Das, G., Toma, A., Zaccaria, R. P.., Di Fabrizio, E., "3D hollow nanostructures as building blocks for multifunctional plasmonics.," Nano Lett. **13**(8), 3553–3558 (2013).

[27] Nazir, A., Panaro, S., Proietti Zaccaria, R., Liberale, C., De Angelis, F.., Toma, A., "Fano coil-type resonance for magnetic hot-spot generation," Nano Lett. **14**, 3166–3171 (2014).

[28] Cerea, A., Garoli, D., Zilio, P., Dipalo, M., Calandrini, E., Jacassi, A., Caprettini, V., Carrara, A., Pelizzo, M. G., et al., "Modified three-dimensional nanoantennas for infrared hydrogen detection," Microelectron. Eng. **162**, 105–109 (2016).

[29] Ye, T., Dai, Z., Mei, F., Zhang, X., Zhou, Y., Xu, J., Wu, W., Xiao, X.., Jiang, C., "Synthesis and optical properties of gold nanorods with controllable morphology," J. Phys. Condens. Matter **28**(43), 434002 (2016).

[30] Chirumamilla, M., Chirumamilla, A., Roberts, A. S., Zaccaria, R. P., De Angelis, F., Kjaer

Kristensen, P., Krahne, R., Bozhevolnyi, S. I., Pedersen, K., et al., "Hot-Spot Engineering in 3D Multi-Branched Nanostructures: Ultrasensitive Substrates for Surface-Enhanced Raman Spectroscopy," Adv. Opt. Mater. **5**(4), 1600836 (2017).

[31] Panaro, S., Nazir, A., Proietti Zaccaria, R., Razzari, L., Liberale, C., De Angelis, F.., Toma, A., "Plasmonic Moon: A Fano-Like Approach for Squeezing the Magnetic Field in the Infrared," Nano Lett. **15**(9), 6128–6134 (2015).

[32] Malerba, M., Alabastri, A., Miele, E., Zilio, P., Patrini, M., Bajoni, D., Messina, G. C., Dipalo, M., Toma, A., et al., "3D vertical nanostructures for enhanced infrared plasmonics," Sci. Rep. **5** (2015).

[33] Nie, S., "Probing Single Molecules and Single Nanoparticles by Surface-Enhanced Raman Scattering," Science (80-. ). **275**(5303), 1102–1106 (1997).

[34] Willets, K. A.., Duyne, R. P. Van., "Localized Surface Plasmon Resonance Spectroscopy and Sensing," Annu. Rev. Phys. Chem. **58**(1), 267–297 (2007).

[35] Purcell, E. M., "Proceedings of the American Physical Society," Phys. Rev. **69**(11–12), 674–674, American Physical Society (1946).

[36] Plumhof, J. D., Stöferle, T., Mai, L., Scherf, U.., Mahrt, R. F., "Room-temperature Bose–Einstein condensation of cavity exciton–polaritons in a polymer," 247, Nature Publishing Group (2013).

[37] Volz, T., Reinhard, A., Winger, M., Badolato, A., Hennessy, K. J., Hu, E. L.., Imamoğlu, A., "Ultrafast all-optical switching by single photons," 605, Nature Publishing Group (2012).

[38] Kéna-Cohen, S.., Forrest, S. R., "Room-temperature polariton lasing in an organic single-crystal microcavity," 371, Nature Publishing Group (2010).

[39] Frenkel, J., "On the Transformation of light into Heat in Solids. I," Phys. Rev. **37**(1), 17–44, American Physical Society (1931).

[40] Peierls, R., "Zur Frage des elektrischen Widerstandsgesetzes für tiefe Temperaturen," Ann. Phys. **404**(2), 154–168, WILEY-VCH Verlag (1932).

[41] Wannier, G. H., "The Structure of Electronic Excitation Levels in Insulating Crystals," Phys. Rev. **52**(3), 191–197, American Physical Society (1937).

[42] Knox, R. S., Theory of excitons (1963).

[43] Veamatahau, A., Jiang, B., Seifert, T., Makuta, S., Latham, K., Kanehara, M., Teranishi, T.., Tachibana, Y., "Origin of surface trap states in CdS quantum dots: relationship between size dependent photoluminescence and sulfur vacancy trap states," Phys. Chem. Chem. Phys. **17**,

2850–2858 (2015).

[44] Liang, W. Y., “Excitons,” Phys. Educ. **5**(4), 226 (1970).

[45] Davydov, A., Theory of molecular excitons, Springer US (2013).

[46] Törmä, P.., Barnes, W. L., “Strong coupling between surface plasmon polaritons and emitters: a review,” Reports Prog. Phys. **78**(1), 13901 (2015).

[47] Agranovich, V. M., Litinskaia, M.., Lidzey, D. G., “Cavity polaritons in microcavities containing disordered organic semiconductors,” Phys. Rev. B **67**(8), 85311, American Physical Society (2003).

[48] Zengin, G., Wersäll, M., Nilsson, S., Antosiewicz, T. J., Käll, M.., Shegai, T., “Realizing Strong Light-Matter Interactions between Single-Nanoparticle Plasmons and Molecular Excitons at Ambient Conditions,” Phys. Rev. Lett. **114**(15), 157401, American Physical Society (2015).

[49] Wang, H., Toma, A., Wang, H.-Y., Bozzola, A., Miele, E., Haddadpour, A., Veronis, G., De Angelis, F., Wang, L., et al., “The role of Rabi splitting tuning in the dynamics of strongly coupled J-aggregates and surface plasmon polaritons in nanohole arrays,” Nanoscale **8**(27), 13445–13453, The Royal Society of Chemistry (2016).

[50] Bellessa, J., Bonnand, C., Plenet, J. C.., Mugnier, J., “Strong Coupling between Surface Plasmons and Excitons in an Organic Semiconductor,” Phys. Rev. Lett. **93**(3), 36404, American Physical Society (2004).

[51] Hakala, T. K., Toppari, J. J., Kuzyk, A., Pettersson, M., Tikkanen, H., Kunttu, H.., Törmä, P., “Vacuum Rabi Splitting and Strong-Coupling Dynamics for Surface-Plasmon Polaritons and Rhodamine 6G Molecules,” Phys. Rev. Lett. **103**(5), 53602, American Physical Society (2009).

[52] Väkeväinen, A. I., Moerland, R. J., Rekola, H. T., Eskelinen, A.-P., Martikainen, J.-P., Kim, D.-H.., Törmä, P., “Plasmonic Surface Lattice Resonances at the Strong Coupling Regime,” Nano Lett. **14**(4), 1721–1727, American Chemical Society (2014).

[53] Gómez, D. E., Vernon, K. C., Mulvaney, P.., Davis, T. J., “Surface Plasmon Mediated Strong Exciton−Photon Coupling in Semiconductor Nanocrystals,” Nano Lett. **10**(1), 274–278, American Chemical Society (2010).

[54] Santhosh, K., Bitton, O., Chuntonov, L.., Haran, G., “Vacuum Rabi splitting in a plasmonic cavity at the single quantum emitter limit,” Nat. Commun. **7**, ncomms11823, The Author(s) (2016).

[55] Vasa, P., Wang, W., Pomraenke, R., Lammers, M., Maiuri, M., Manzoni, C., Cerullo, G.., Lienau, C., “Real-time observation of ultrafast Rabi oscillations between excitons and plasmons

in metal nanostructures with J-aggregates," Nat. Photonics **7**, 128, Nature Publishing Group (2013).

[56] Balci, S., Kocabas, C., Küçüköz, B., Karatay, A., Akhüseyin, E., Gul Yaglioglu, H.., Elmali, A., "Probing ultrafast energy transfer between excitons and plasmons in the ultrastrong coupling regime," Appl. Phys. Lett. **105**(5), 51105, American Institute of Physics (2014).

[57] Schwartz, T., Hutchison, J. A., Léonard, J., Genet, C., Haacke, S.., Ebbesen, T. W., "Polariton Dynamics under Strong Light–Molecule Coupling," ChemPhysChem **14**(1), 125–131, WILEY-VCH Verlag (2013).

[58] Dintinger, J., Klein, S., Bustos, F., Barnes, W. L.., Ebbesen, T. W., "Strong coupling between surface plasmon-polaritons and organic molecules in subwavelength hole arrays," Phys. Rev. B **71**(3), 35424, American Physical Society (2005).

[59] Wang, H., Wang, H.-Y., Bozzola, A., Toma, A., Panaro, S., Raja, W., Alabastri, A., Wang, L., Chen, Q.-D., et al., "Dynamics of Strong Coupling between J-Aggregates and Surface Plasmon Polaritons in Subwavelength Hole Arrays," Adv. Funct. Mater. **26**(34), 6198–6205 (2016).

[60] Hartland, G. V., "Optical Studies of Dynamics in Noble Metal Nanostructures," Chem. Rev. **111**(6), 3858–3887, American Chemical Society (2011).

[61] Coles, D. M., Grant, R. T., Lidzey, D. G., Clark, C.., Lagoudakis, P. G., "Imaging the polariton relaxation bottleneck in strongly coupled organic semiconductor microcavities," Phys. Rev. B **88**(12), 121303, American Physical Society (2013).

[62] Chikkaraddy, R., de Nijs, B., Benz, F., Barrow, S. J., Scherman, O. A., Rosta, E., Demetriadou, A., Fox, P., Hess, O., et al., "Single-molecule strong coupling at room temperature in plasmonic nanocavities," Nature **535**, 127, Nature Publishing Group, a division of Macmillan Publishers Limited. All Rights Reserved. (2016).

[63] Kasera, S., Herrmann, L. O., Barrio, J. del., Baumberg, J. J.., Scherman, O. A., "Quantitative multiplexing with nano-self-assemblies in SERS," Sci. Rep. **4**, 6785, Nature Publishing Group (2014).

[64] Hutchison, J. A., Schwartz, T., Genet, C., Devaux, E.., Ebbesen, T. W., "Modifying Chemical Landscapes by Coupling to Vacuum Fields," Angew. Chemie Int. Ed. **51**(7), 1592–1596, WILEY-VCH Verlag (2012).

[65] Hutchison, J. A., Liscio, A., Schwartz, T., Canaguier-Durand, A., Genet, C., Palermo, V., Samorì, P.., Ebbesen, T. W., "Tuning the Work-Function Via Strong Coupling," Adv. Mater. **25**(17), 2481–2485, WILEY-VCH Verlag (2013).

[66] Orgiu, E., George, J., Hutchison, J. A., Devaux, E., Dayen, J. F., Doudin, B., Stellacci, F., Genet, C., Schachenmayer, J., et al., "Conductivity in organic semiconductors hybridized with the vacuum field," Nat. Mater. **14**, 1123, Nature Publishing Group (2015).

[67] Arias, A. C., MacKenzie, J. D., McCulloch, I., Rivnay, J.., Salleo, A., "Materials and Applications for Large Area Electronics: Solution-Based Approaches," Chem. Rev. **110**(1), 3–24 (2010).

[68] Forrest, S. R., "The path to ubiquitous and low-cost organic electronic appliances on plastic," Nature **428**, 911, Macmillian Magazines Ltd. (2004).

[69] McKeever, J., Boca, A., Boozer, A. D., Buck, J. R.., Kimble, H. J., "Experimental realization of a one-atom laser in the regime of strong coupling," Nature **425**, 268, Macmillian Magazines Ltd. (2003).

[70] Chang, D. E., Sørensen, A. S., Demler, E. A.., Lukin, M. D., "A single-photon transistor using nanoscale surface plasmons," Nat. Phys. **3**, 807, Nature Publishing Group (2007).

[71] Nagasawa, F., Takase, M.., Murakoshi, K., "Raman Enhancement via Polariton States Produced by Strong Coupling between a Localized Surface Plasmon and Dye Excitons at Metal Nanogaps," J. Phys. Chem. Lett. **5**(1), 14–19, American Chemical Society (2014).

[72] Hobson, P. A., Wedge, S., Wasey, J. A. E., Sage, I.., Barnes, W. L., "Surface Plasmon Mediated Emission from Organic Light-Emitting Diodes," Adv. Mater. **14**(19), 1393–1396, WILEY-VCH Verlag (2002).

# Chapter 3

# Strong coupling at THz frequencies: building up the system

Strong light-matter coupling has been the subject of extensive research in the last decades and has led to fundamental discoveries, some of which were described in the previous chapter. Through the formation of hybrid states, light-matter strong interaction offers exciting new perspectives for molecular and material sciences by inducing significant changes in the properties of the each constituent. So far, these concepts have been mainly investigated by linking electronic transitions (in the form of excitons) to the confined electromagnetic field of a cavity, a photonic crystal or a plasmonic resonator.

This phenomenon, however, is not limited to electronic transitions. Very recently, it has been shown that also vibrational modes can be coupled to electromagnetic radiation to achieve the strong coupling regime in the infrared (IR) and terahertz (THz) spectral range, where phonon resonances lie[1–4]. Phonons, namely quanta of collective vibrations, are central to the emerging technology termed "phononics", which focuses on understanding and controlling the phononic properties of materials with particular attention on applications such as phononic crystals[5], acoustic and thermal cloaking[6,7], thermal diodes[8] and thermoelectrics[9]. Before the advent of this young field, phonons were mainly associated with heat, lost energy and noise and regarded as a major source of energy dissipation in solid-state systems, thus affecting some of the most relevant properties (electronic, thermal, optical) of materials. Of particular significance for nanotechnology, phonons severely affect light emission in luminescent nanomaterials and charge transport in nanoelectronic devices. Electron-phonon interactions and the predominantly dissipative nature of phonons are also responsible for decoherence of the atom-like quantum states hosted by low-dimensional solid-state structures, such as quantum dots[10].

## 3.1 Vibrational strong coupling: state of the art

Vibrational strong coupling (VSC) offers the possibility to take advantage of the phonon characteristics to modify the intrinsic properties of materials. The vibro-polariton states obtained under VSC are

formed by superposition of a cavity photon (or plasmon mode) and excited molecular vibrations that are collectively distributed over a large number of molecules (see Figure 3.1). The modification of bond strengths and molecular vibration frequencies associated with this phenomenon plays a crucial role in chemistry, since it could open many possibilities in chemical reactivity, catalysis and site-selective reactions. So far, hybridization has been obtained by filling Fabry-Pérot microcavities featuring sharp infrared resonances with either solid layers[11] or liquids[12] containing the targeted molecules. This approach is potentially a simple way to modify a given chemical bond, generating two new vibrational modes (vibrational polaritonic states) and modifying the associated chemistry and chemical properties[13] of the molecule.

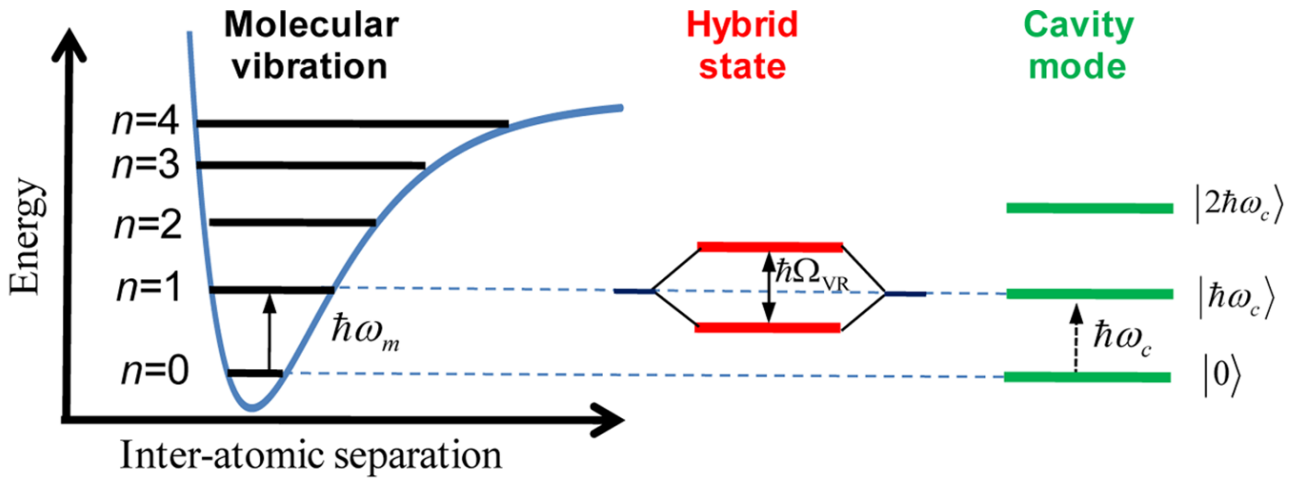


**Figure 3.1:** Schematic illustration of the light matter coupling between one vibrational transition and a cavity mode resulting in the Rabi splitting $\hbar\Omega_{VR}$.

The first demonstration of VSC was given by Shalabney et al.[11], who obtained coherent strong interactions between molecular vibrational transitions of a large number of oscillators and an optical mode of a surrounding Fabry-Pérot microcavity. Even if the Rabi splitting obtained for a single molecular transition is well below the mechanical damping rate, strong interaction can be achieved in this system by coupling several resonators with the same cavity mode, as in the present case. In this picture, the spatially coherent single-mode cavity field drives all the coupled resonators in phase with each other. This induces coherence among the resonators within the whole mode volume and leads to the definition of a macroscopic collective dipole. In order to achieve VSC, they choose polyvinyl acetate, which is characterized by a vibration band (symmetric stretching of C = O bond) well isolated from other modes, hybridized with the first mode of a specifically designed cavity. By acquiring the

transmission spectra of the coupled system with a Fourier transform interferometer (see Figure 3.2a), they were able to measure a vacuum Rabi splitting at room temperature of about 20 meV, well exceeding the decoherence rates of the constituents. As a result, the formation of two new opto-vibrational modes were observed (the upper and lower polaritonic states) corresponding to molecular vibrations dressed by the cavity vacuum field. The hybrid peaks position as a function of incidence angle shows an anti-crossing behaviour (Figure 3.2b), which is the unambiguous signature of the strong coupling regime, opening up the possibility to modify chemical reactions by engineering the energy landscape of the system.

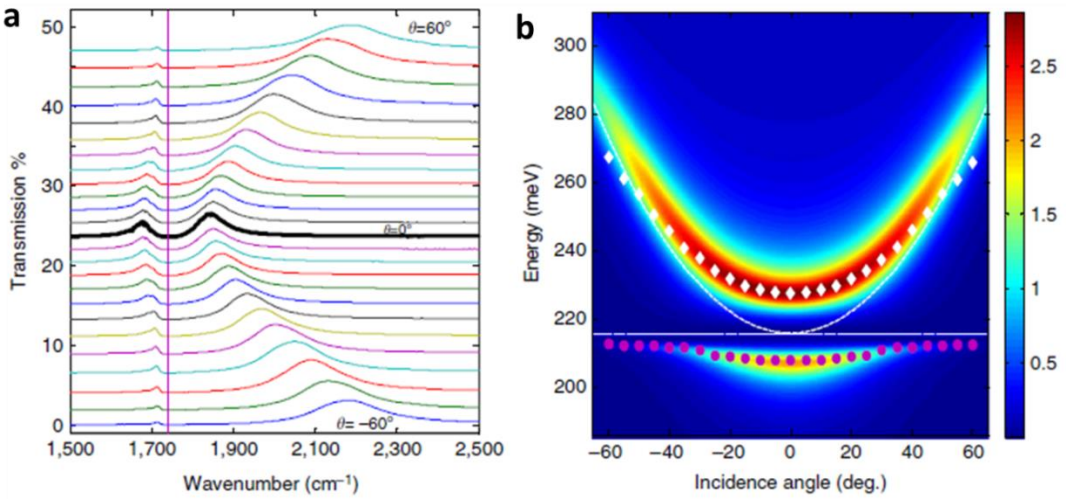


**Figure 3.2: a)** Measured transmission spectra of the cavity-molecules system as a function of the IR-beam incidence angle. At normal incidence ($\theta = 0°$), the avoided crossing is clearly revealed as the signature of the strong coupling regime between the cavity mode and the (C = O) stretching mode, whose position in the uncoupled situation in indicated by a vertical line. **b)** Colour plot of the polariton dispersion. Cavity diamonds and purple circles correspond, respectively, to the measured positions of the upper and lower polaritons. The dashed curve and dashed horizontal line show, respectively, the dispersion of the empty cavity and vibrational uncoupled mode.

Exploiting a similar design, VSC was achieved in a liquid environment by Vergauwe[14] in the case of protein vibrational modes and by George[12] and Thomas[13] for different organic molecules.

In a later work, Shalabney at al.[15] investigated the Raman scattering of hybridized light-matter states. They demonstrated that the coherent nature of the vibro-polariton states can boost the Raman scattering cross-section by two to three orders of magnitude, revealing a new enhancement mechanism as a result of vibrational strong coupling. Also in this case, VSC was achieved by matching the mode of a Fabry-

Pérot cavity with a vibrational transition of polyvinyl acetate molecules, which are active in both IR and Raman spectroscopy (see Figure 3.3a for the energy level scheme). When the cavity thickness was tuned to couple to the vibrational frequencies of the molecule, a clear splitting in the transmission spectrum of the cavity-molecule system was visible with the appearance of two hybrid states (see Figure 3.3b).

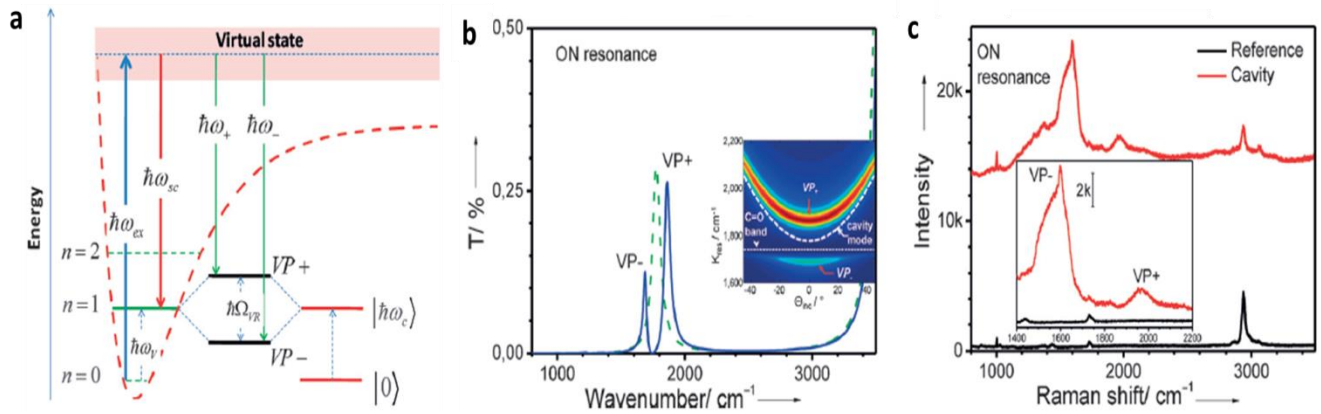


**Figure 3.3: a)** Energy-level diagram under vibrational strong coupling showing the scheme for the Raman scattering from the new vibro-polariton states. **b)** Cavity transmission without (dashed green) and with coupled resonators (solid blue line) showing the formation of the hybrid bands, also shown by the dispersion (inset). **c)** Raman scattering from the cavity given in (**c)** showing in the inset the new density of states.

In the on-resonance situation, these new features were also visible in the Raman signal coming from the hybridized molecules (see Figure 3.3c). These peaks were not present in the Raman scattering of the reference (uncoupled molecules) and could only originate from the formation of upper/lower vibro-polaritons (VP±) in the coupled system. Contemporarily with this effect, they observed a $10^2/10^3$ enhancement in the scattering cross-section for the coupled molecules relative to the reference sample. They claimed that, being the coupled resonators in phase with each other in the strong coupling regime, the Raman signal could be boosted either by constructive interference or by enhanced polarizability of the single molecules. This aspect was theoretically investigated by del Pino et al.[16,17] who focused on the collective nature of the vibro-polariton states. In their model, the dynamics of an ensemble of organic molecules in the strong coupling regime can be described through a single collective oscillator coupled to a photonic mode of the cavity, but no collective enhancement of the Raman signal is predicted, thus being in contrast with the experimental findings of Shalabney et al.[15]. They demonstrated that the main effect of VSC is a redistribution of the total Raman cross section, which is

therefore approximately conserved, as long as the ultra-strong coupling regime is not reached. In order to explain the enhanced Raman signal, they considered two possible scenarios: either the VSC process induces a modification of the bare molecule transition strengths or the Raman cross section is increased by non-linear effects that were not taken into consideration. However, they were not able to find a univocal explanation, thus highlighting the necessity for further theoretical and experimental studies of the process.

In a recent work of Kerfoot et al.[18], phonon-induced transparency in a pair of QDs is achieved *via* the formation of a molecular polaron[19], a mechanism by which the interacting phonon is made non-dissipative and coherent, thereby enhancing coherent interaction between the two dots. They demonstrated the transparency, as a result of a Fano-type quantum interference mechanism, to be widely tunable both optically and electrically, thus providing a tool to increase the performance of optoelectronic and quantum devices.

In the last few years, hybridization of phonon resonances with an electromagnetic field has been also explored in the case of plasmonic elements providing the light constituent of the coupled system. In this context, induced transparency was observed by Huck et al.[20] in the case of metal antenna plasmons coupled to the surface phonons in a $SiO_2$ layer in the IR spectral range.

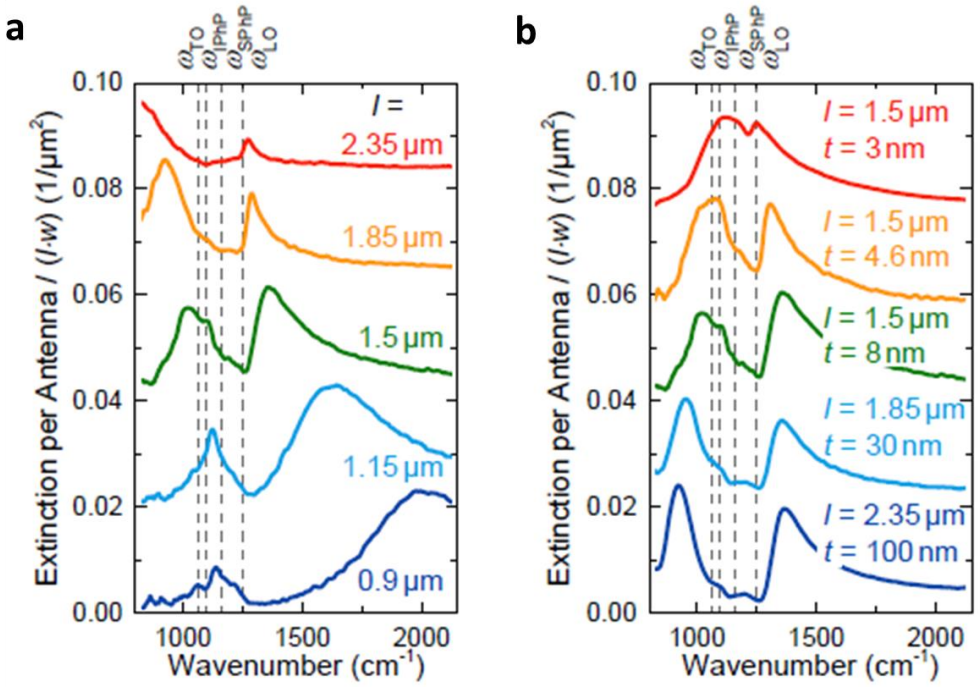

**Figure 3.4: a)** Extinction spectra of nanoantennas with different length *l* on top of a 8 nm thick $SiO_2$ layer with a Si wafer beneath. **b)** Extinction spectra of antennas on $SiO_2$ with increasing thickness *t*. The antenna lengths are resonantly matched to the TO and LO frequencies.

In far-field extinction spectra, acquired with an IR light source coupled to a IR microscope and spectrometer, a transparency window opens close to the LO mode of the $SiO_2$ layer underneath the metal nanoantennas. Representative spectra of different antenna lengths on top of a 8 nm thick layer are shown in Figure 3.4a. For detuned antennas ($l = 0.9$ μm) the plasmon resonance is located in the mid IR and two distinct peaks appear in the spectrum, but both excitations are already hybridized even though the resonances are not matched. For longer antennas the resonance shifts towards the $SiO_2$ vibration and both excitations hybridize strongly. As a consequence a transparency window between the LO and surface phonon polariton (SPhP) frequencies opens, which is strongest for resonantly tuned antennas. In Figure 3.4b, the evolution of this window with $SiO_2$ layer thickness *t* is shown. Since the resonance frequency strongly depends on the layer thickness, tunable transparency windows can be created. For oxide layer thickness larger than 30 nm, a full transparency window is formed in the plasmonic extinction. The observation of this strong coupling effect means that the antenna on the $SiO_2$ layer becomes invisible as a result of coupling to the layer beneath, which without antenna has a forbidden excitation exactly at the plasmonic resonance. In a similar work, Shelton et al.[1] obtained hybridization of the surface phonon of a thin $SiO_2$ layer with the plasmon mode of metallic split-ring resonators (SRRs). In particular, they investigated the dependence of the coupling strength on the metamaterial design, the dielectric layer thickness and its proximity to the resonators, and the amount of field overlap between the system constituents, thus unveiling the near-field character of the strong coupling phenomenon.

With the spreading of graphene potentialities, people have started to exploit these relatively "young" material also in view of light-matter strong coupling. In a pioneering work of Luxmoore et al.[3], they investigated the transmission characteristics of electrically contacted nanoribbon arrays on a 300 nm thick $SiO_2$ layer. They demonstrated strong coupling of the graphene plasmon to three distinct surface optical (SO) phonon modes of the underlying dielectric, including a resonance at about 30 μm, therefore extending graphene plasmonics into the far-infrared range. Using a FTIR spectrometer, they measured the transmission of patterned arrays of nanoribbons for a given gate voltage applied. As it is shown in Figure 3.5a, when the incident light is polarized parallel to the nanoribbons long-axis no

spectral feature is present in the transmission spectrum, while for perpendicular polarization four sharp absorption resonances appear. These resonances can be attributed to the coupling of graphene plasmons with SO phonons of the $SiO_2$ *via* the long-range Fröhlich interaction, resulting in the excitation of surface plasmon-phonon-polariton modes. The positions of the hybrid resonances are shown in Figure 3.5b as a function of the uncoupled plasmon wavevector *q* and display the characteristic anti-crossing behaviour of strongly coupled systems.

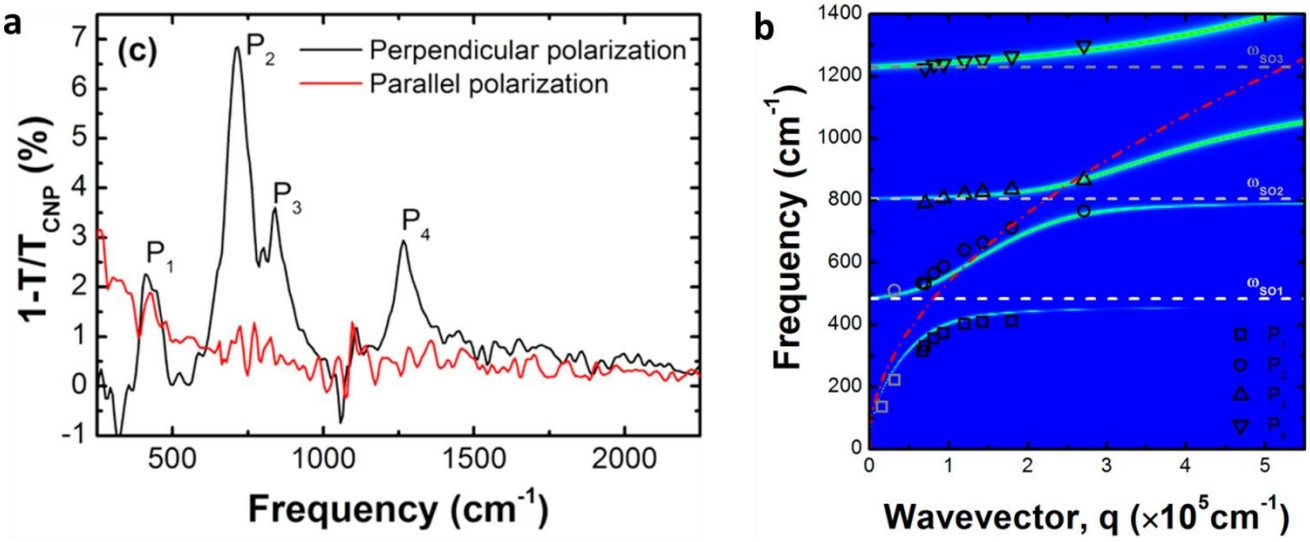


**Figure 3.5: a)** Extinction spectra of a 180 nm wide graphene nanoribbon array on $SiO_2$ for incident light polarized parallel and perpendicular to the ribbons. When the light is polarized perpendicular to the nanoribbon, four peaks, labeled $P_1$ – $P_4$, are clearly identified. **b)** Calculated loss plot with extracted peak frequencies overlaid. The red dashed line shows the calculated dispersion of the uncoupled graphene plasmon. The white, light grey and grey dashed lines show the calculated frequency of the three surface optical phonons. The grey symbols are peak positions extracted from microribbon arrays.

In this context, our work concentrates on the realization of plasmon-phonon hybridization in a nanoscale system strongly coupled with the THz vacuum electric field. This is achieved by combining the extreme radiation confinement properties oh THz plasmonic nanocavities[21] with the marked dipole-active phonon resonance of polar semiconductor cadmium sulfide (CdS) nanocrystals (NCs)[10] located at around 8 THz. In such plasmonic nanocavities, the THz vacuum field (i.e. the field associated with the quantum zero-point energy of the cavity resonance mode) can reach extraordinary high values and can be effectively coupled with the phonon resonance of the nanocrystals. Hybridization in this nanoscale system leads to a dramatic change of the NCs phonon spectrum and to characteristics that no longer belong to the original nanomaterial. Our findings open exciting perspectives for engineering the

optical phonon response of functional materials and for the realization of a novel platform for nanoscale quantum optomechanics.

In the following sections, the constituents of the coupled system will be characterized in detail both theoretically and experimentally and their utilization in previous works will be described.

## 3.2 THz plasmonic nanoantennas

In order to investigate plasmon-phonon strong coupling in the THz regime, we fabricated arrays of gold plasmonic nanoantennas (covering an area of 200 x 200 $\mu m^2$) separated by narrow gaps, which represent the plasmonic nanocavities where hybridization occurs, by means of electron beam lithography (EBL) technique. EBL is a powerful method for creating nanostructures that are too small to fabricate with conventional photolithography. State of the art EBL systems can achieve resolution down to sub-10 nm using an accelerated beam of electrons to pattern features on samples that have been coated with an electron sensitive resist. The electron beam induces a change in the molecular structure and solubility of the resist film. Following electron exposure, the resist is developed in a suitable solvent to selectively dissolve either the exposed or unexposed areas of the resist. After this steps, the resist layer remaining can be used as an etch mask or template for either transferring the pattern into the underlying substrate or depositing metallic films.

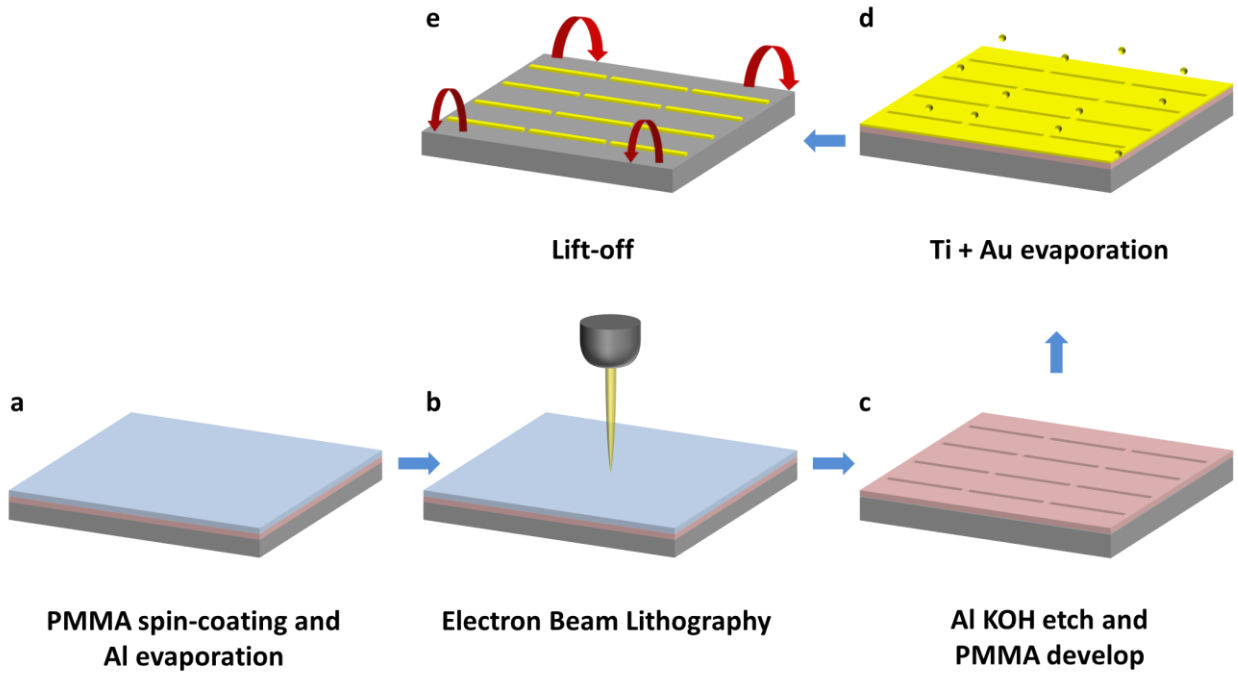


**Figure 3.6: a) - e)** Fabrication steps of the THz nanoantenna arrays.

The fabrication procedure was carried out in a Cleanroom environment (ISO6, or equivalently class1000) to prevent sample contamination from environmental pollutants. A schematic representation of the various fabrication steps is provided in Figure 3.6. After cleaning in an ultrasonic bath of acetone and isopropyl alcohol, a 160-nm thick poly(methyl methacrylate) (PMMA) layer was spin-coated at 1800 rpm on a 500- μm thick, high resistivity (> 10 kΩcm) (100)-oriented silicon chip. Subsequently, annealing was performed at 180 °C for 7 minutes. In order to prevent charging effects during the electron beam exposure, a 10-nm thick Al layer was thermally evaporated on the PMMA surface (Figure 3.6a). Electron beam direct-writing of the nanoantenna arrays was carried out using an ultra-high resolution Raith 150-Two e-beam lithography and imaging system, which enables nanostructures fabrication with a resolution down to few nanometers (Figure 3.6b). During exposure of the nanoantennas, a beam energy of 20 keV was employed, setting the exposure dose to 550 μC/cm$^2$. After the Al conductive layer removal in a 1 M KOH solution, the exposed resist was developed in a solution of methyl isobutyl ketone (MIBK)/isopropanol (IPA) (1:3) for 30 s (Figure 3.6c). Electron beam evaporation in a high vacuum chamber (base pressure $10^{-7}$ mbar) was exploited to produce a 5-nm adhesion layer of titanium and a 50-nm Au film, with a 0.3 Å/s deposition rate (Figure 3.6d). Finally, the unexposed resist was removed through a conventional lift-off process in hot acetone (Figure 3.6e). To improve the lift-off efficiency, sonication for 2 minutes at 40 kHz frequency was employed. The substrate was then rinsed out in IPA for 30 s and dried in nitrogen. $O_2$ plasma ashing at 150 W for 10 minutes was used to remove residual PMMA resist and other organic residues.

The fabricated two-dimensional arrays cover an area of 200 × 200 μm$^2$ and are composed of chains of h = 55-nm high and w = 200-nm wide dipole antennas coupled end-to-end through a fixed gap $G_x$ = 30 nm (about 750 nanogaps for each array) along their long-axis direction and featuring a spacing $G_y$ = 8.5 μm along their short-axis direction. A schematic view of a THz nanoantenna array and a single-nanocavity region is presented in Figure 3.7. Arrays with different nanoantenna length L, ranging from 4 to 7 μm, were fabricated on the same silicon substrate in order to tune their plasmonic resonance in the THz frequency band around the optical phonon mode of the nanocrystals. A Helios NanoLab 600i scanning electron microscope (SEM) has been used to acquire the images reported in Figure 3.7 of a nanoantenna coupled with its neighbour antennas and the detail of the nanocavity region. Through direct visual inspection with the SEM system, we have collected high-resolution SEM images of few tens of nanogaps and we have therefore extracted an average gap size of $G_{x,0} = 32.2 \pm 3.7$ nm, finding good correspondence with the expected value.

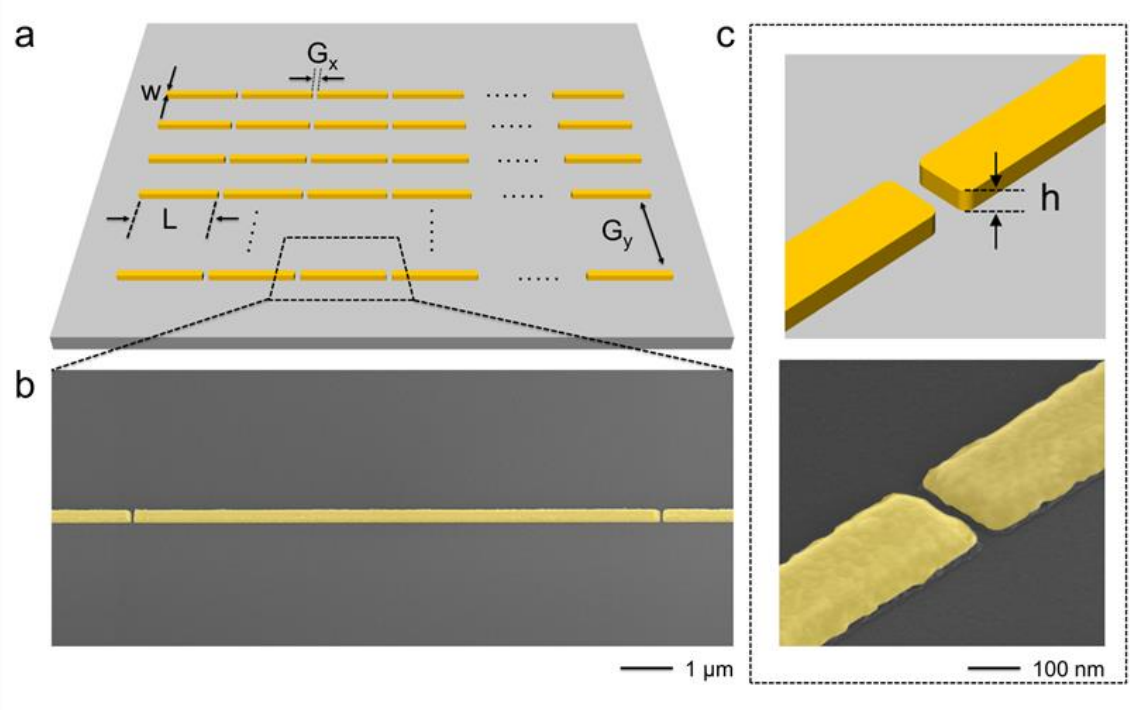


**Figure 3.7: a)** Schematic view of THz antennas on the Si substrate. **b)** SEM image in false colors of a THz nanoantenna coupled to its neighbour antennas. **c)** Sketch showing the details of the cavity gap between two antennas (upper panel) and corresponding SEM picture in false colors (lower panel).

In order to estimate the best nanoantenna configuration that matches the phonon resonance of the NCs, we have performed electromagnetic simulations using a commercial Finite Element Method-based software: COMSOL Multiphysics, Optics Module. For the silicon substrate we assumed a constant refractive index of $n_{sub}$ = 3.42, while the complex permittivity of gold was taken from literature[22]. We considered nanoantenna with geometrical parameters corresponding to the fabricated values (see above) and the nanoantenna length was varied in the same range (4-7 µm) to tune the array resonance peak position. All the nanoantenna sharp edges were rounded with a radius of curvature of 20 nm, except the ones perpendicular to the substrate in correspondence of the nanocavities, where a curvature of 40 nm was introduced to better resemble the fabricated structures. The response of an infinite nanoantenna array was obtained by imposing appropriate periodic boundary conditions in the plane of the array. Two perfectly matched layers (PMLs) were instead set as boundary conditions at the top (air) and bottom (silicon substrate) of the calculation domain, to avoid spurious reflections.

For the input illumination conditions, we employed a linearly polarized plane wave. The plane of incidence was tilted by an angle φ = 45° with respect to the nanoantenna long axis, while the angle of

incidence in this plane was set to θ = 18° (in accordance with the mean incidence angle of the Cassegrain objective used in THz measurements, see Chapter 4). The polarization state of the wave was then set taking into account the input polarization (parallel to the nanoantenna long axis) impinging on the Cassegrain objective. We found that this type of illumination well reproduces the transmission response of the arrays. Finally, the results of the simulations were normalized to the area of the illuminating THz spot in the experimental measurements (diameter D ≈ 260 μm), which is bigger of the array dimensions (200 x 200 $\mu m^2$).

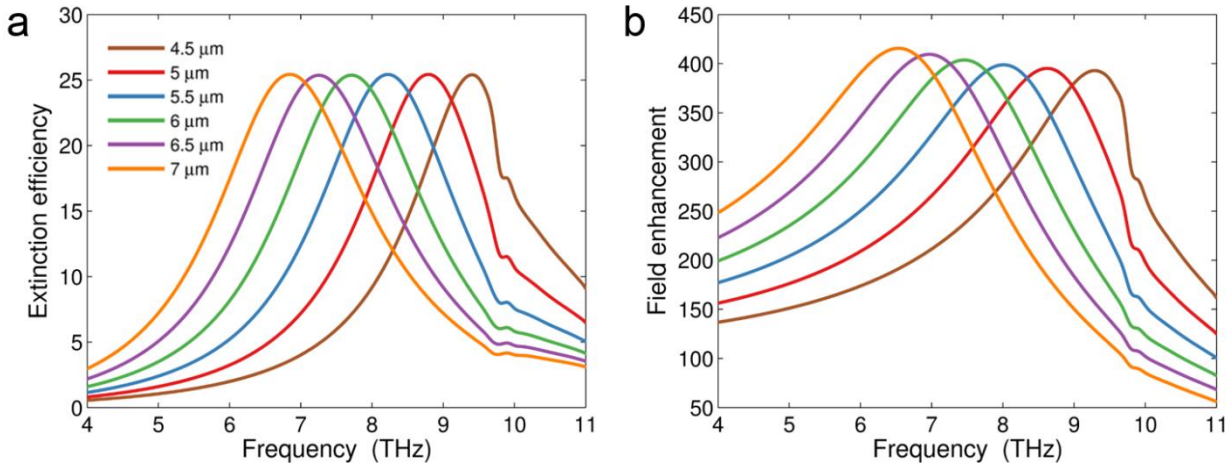


**Figure 3.8: a)** Extinction efficiency for six different nanoantenna lengths. **b)** Corresponding field enhancement values, estimated in the center of the nanocavity.

Figure 3.8a shows the nanoantenna extinction efficiency (the ratio of the extinction cross section to the nanoantenna geometrical area) for arrays with different nanoantenna lengths as function of frequency, and shows how the array resonance can be easily tuned across a wide frequency range. Here the array response of L = 5.5-6 μm nanoantennas best overlaps the NCs phonon resonance located close to 8 THz (see next section). Figure 3.8b shows instead the dispersion of the near field enhancement value (the ratio of the local electric field to the background field) in the center of the nanocavities demonstrating the high field-enhancement and strong localization into subwavelength nanoscale volumes, making this design particularly suitable for applications in THz spectroscopy.

In both figures above, the presence of an array lattice mode at around 9.8 THz is clearly visible as a kink in the simulated spectra. The lattice modes of a plasmonic array[23] arise from the mutual electromagnetic coupling of the individual plasmonic scatterers, associated with a grazing (diffracted) wave in the plane of the array. When a lattice mode is spectrally close to a plasmonic resonance of the

array elements, the energy transfer between these two excitations can reshape the overall spectral response, also leading to an increase of the array resonance quality factor[24]. Lattice resonances are known to be in correspondence of the so-called Wood-Rayleigh anomalies[23] and for our specific configuration, the lowest energy anomaly appears at the frequency that satisfies the following equation:

$$k_{sub} = \left| \boldsymbol{k}_x + \boldsymbol{k}_y - \boldsymbol{A}_y \right| \tag{53}$$

where $k_{sub} = k_0 n_{sub} = \frac{2\pi\nu n_{sub}}{c}$ is the absolute value of the wave vector in the array substrate, $\boldsymbol{k}_x = \hat{e}_x k_0 \sin\theta \cos\varphi$ and $\boldsymbol{k}_y = \hat{e}_y k_0 \sin\theta \sin\varphi$ are the x and y in-plane components of the incident light wave vector (with φ being the angle formed by the plane of incidence with the long axis of the nanoantennas and θ the angle of incidence within this plane), while $\boldsymbol{A}_y = \hat{e}_y \frac{2\pi}{G_y}$ is the reciprocal lattice vector in the y direction. Figure 3.9 shows how the lattice mode can be straightforwardly tuned by changing the spacing $G_y$ of the array, and also evidences the good agreement between the lattice resonance positions that can be estimated using Eq. (53) (vertical lines) and the ones visible in the electromagnetic simulations (colored curves).

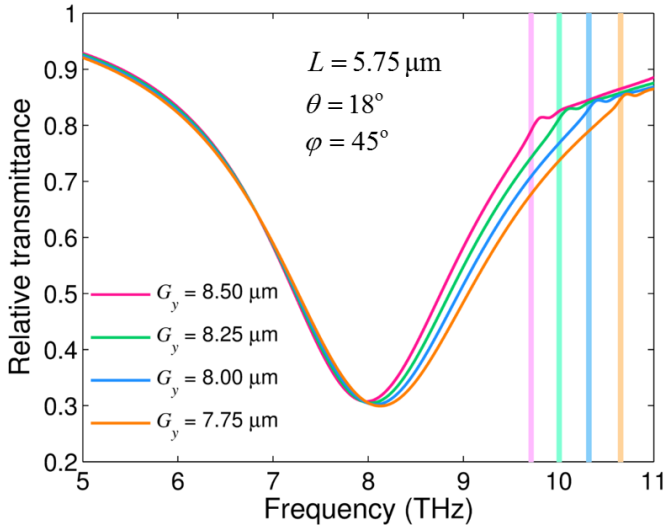


**Figure 3.9:** Lattice mode dependence on the antenna periodicity, estimated for a fixed antenna length L = 5.75 µm. The colored curves are the simulated transmission spectra, while the corresponding vertical lines indicate the lattice resonance positions calculated using Eq. (53) with the parameters of our investigation ($n_{sub}$ = 3.42, θ = 18°, φ = 45°).

So far we have considered the effect of small variations in the y spacing between the nanoantenna chains, but also deviations from the fixed value of the nanoantenna gaps ($G_x$ = 30 nm) might affect the overall array response. In order to evaluate the dependence of the antenna resonance on small gap-size variations, we have performed numerical simulations to evaluate the antenna resonance considering a fixed nanoantenna length $L_0$ = 5.75 μm and evaluating the effect of a gap size change of $\pm\sigma$ obtained from the experimental evaluation (see $G_{x,0}$ estimation above). In the following, we have assumed that the quantity $L + G_x$ remains constant, so that a smaller/larger gap $G_x = G_{x,0} \pm \sigma$ results in longer/shorter antenna length $L = L_0 \mp \sigma$, as should be the case considering the e-beam lithographic process we employed. The results of these simulations are presented in Figure 3.10, which shows on the left side the array transmission as a function of frequency and on the right side a table summarizing the key parameters, including the array resonance position and the relative shift.

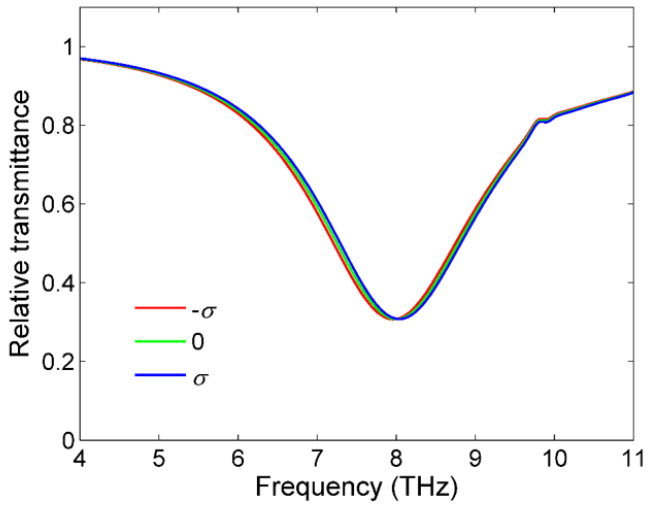


$L_0 = 5.75\,\mu m$

| | -σ | 0 | σ | unit |
|---|---|---|---|---|
| $G$ | 28.5 | 32.2 | 35.9 | nm |
| $L$ | 5.7537 | 5.7500 | 5.7463 | μm |
| Res. | 7.962 | 8.003 | 8.040 | THz |
| Res. Shift | -0.041 | / | 0.037 | THz |

**Figure 3.10:** Effects of nanogap size changes on the array resonance for antenna length corresponding to L = 5.75 μm.

As can be seen both in the transmission spectra and the table, the array resonance position and its bandwidth are only slightly modified by nanogap size distribution.

Having established the geometrical parameters and enhancement properties of our nanocavities, we now want to give an estimate of their mode volume and the THz vacuum electric field that they can support. Knowing these characteristics is of paramount importance to design a system which can be strongly coupled to the nanomaterial resonators, especially in the spectral regime where we operate. Indeed, the vacuum field scales with the square root of the photon energy (extremely low at infrared

and terahertz frequencies) and of the inverse of the effective cavity volume, which in turn is proportional to the cube of the radiation wavelength in traditional cavities and thus becomes particularly large in these spectral regions. These concepts are well exemplified by the following equation for the Rabi splitting observed in systems coupled by means of the vacuum electric field[25],

$$\hbar\Omega_R = 2\,\vec{E}_{vac}\cdot\vec{\mu} = 2\mu\sqrt{\frac{\hbar\omega}{2\varepsilon_0 V}} \tag{54}$$

We therefore performed numerical calculation to determine the electric field distribution in the nanocavity area at resonance on the planes perpendicular to the main simulation axes (see Figure 3.11).

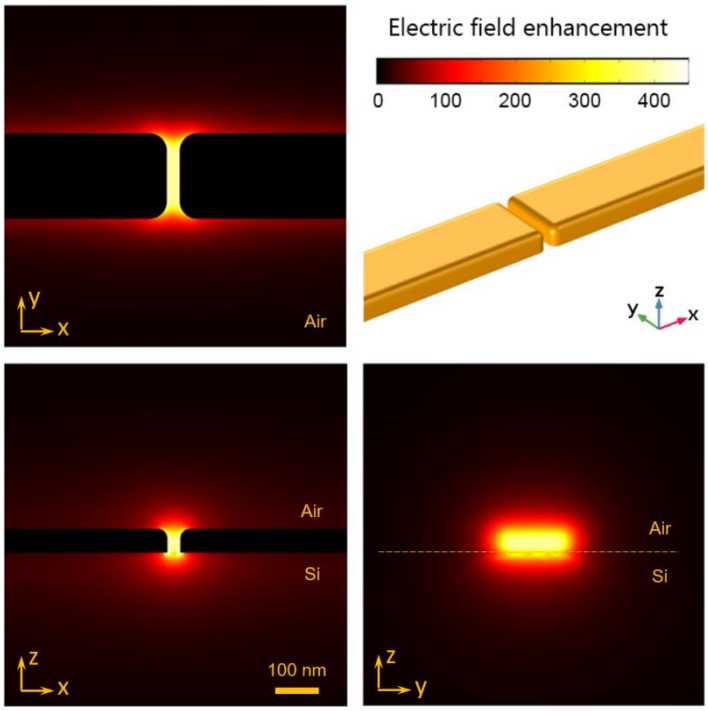


**Figure 3.11:** The local electric field distribution in the area of a nanocavity (all the 2D projections are taken on a plane passing through the nanocavity geometrical center) at the resonance position of 8 THz and for 5.75 μm antennas.

Starting from the distribution of the local electric field in 3D space, the mode volume of the plasmonic nanocavity can be estimated by[26]:

$$V_{mod} = \frac{\int \varepsilon(\boldsymbol{r})|E(\boldsymbol{r})|^2 d\boldsymbol{r}}{max(\varepsilon(\boldsymbol{r})|E(\boldsymbol{r})|^2)} \tag{55}$$

where the numerator can be read as the full domain integral of the energy density, and the denominator as the maximum value of the energy density extracted in the same domain. Considering the case of the array with nanoantenna length L = 5.75 μm (corresponding to a resonance peak at around 8 THz, well aligned to the NC phonon resonance) we obtain a mode volume at resonance as small as $V_{mod} = 1.43 \times 10^6$ nm$^3$, which is much smaller than the volume of an analogous Fabry-Pérot cavity ($V_{Fabry-Pérot} \approx 8 \times 10^{12}$ nm$^3$) supporting a resonant mode at the same frequency. Compared to the geometrical volume of the nanocavity ($V_{geo} \approx 200 \times 30 \times 55$ nm$^3$ $= 0.33 \times 10^6$ nm$^3$), the mode volume is about 4.3 times larger. A graphical comparison of these two quantities is given in Figure 3.12, in which the effective squeezing of the radiation in the nanocavity region becomes evident.

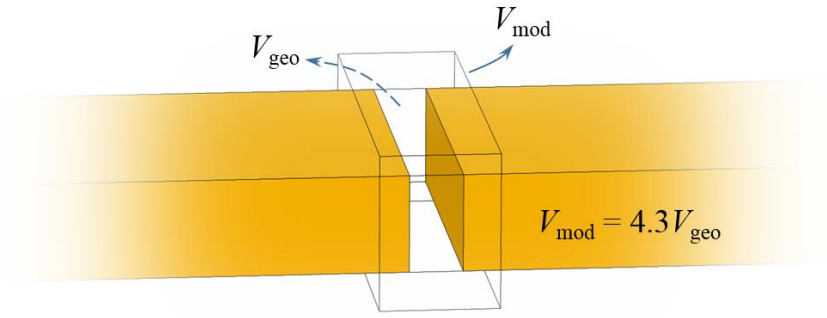


**Figure 3.12:** Size comparison between the geometrical nanocavity volume and the mode volume.

Having an estimate of the mode volume, we can also evaluate the THz vacuum electric field (in air) within the cavity:

$$|E_{vac}| = \sqrt{\frac{\hbar\omega_{res}}{2\varepsilon\varepsilon_0 V_{mod}}} = 4.6 \times 10^5\ V/m \tag{56}$$

where $\omega_{res}$ is the resonance frequency, ħ is the reduced Planck constant, ε and $\varepsilon_0$ are the relative and vacuum permittivities, respectively. The calculated vacuum field thus reaches an extraordinary high value over a nanoscale volume, thus demonstrating the extreme confinement properties of our THz plasmonic nanocavities.

## 3.3 CdS semiconductor nanocrystals

In order to achieve plasmon-phonon strong coupling, we combine the high field enhancement and small mode volumes of our plasmonic nanocavities with the marked dipole-active phonon resonance of cadmium sulfide (CdS) polar NCs.

The NCs were synthesized in the Nanochemistry Department of the Italian Institute of Technology (IIT) using a two-steps protocol, in which a CdS shell of desired thickness was grown on pre-synthesized CdS cores, following the procedure reported in Ref.[27] for CdSe/CdS giant-shell NCs. CdS cores were obtained by mixing 3 g of trioctylphosphine oxide (TOPO), 0.280 g of Octadecylphosphonic acid (ODPA) and 0.060 g of CdO in a 25 mL tri-neck flask. The mixture was heated at 120°C under vacuum for 1 hour. Then, under nitrogen athmosphere, the temperature was increased to 380°C to completely dissolve the CdO. When the CdO was dissolved and the solution became colorless, 1.5 mL of trioctylphosphine (TOP) was injected into the system and the temperature was allowed to recover to 380°C before the injection of TOP:S solution (0.020 g S+ 0.500 g TOP). The time of growth was set to 10 minutes to get cores of 6 nm in diameter. After the synthesis, the NCs were washed by precipitation and re-dissolution (3 times) in toluene and methanol. The final sample was dispersed in 3 mL of toluene.

For the synthesis of core-shell CdS@CdS NCs, cadmium and sulfur precursors were prepared by respectively dissolving 0.640 g of CdO in 5 mL of oleic acid (OA) and 0.160 g S powder in 5 mL of TOP. Both precursors were then diluted with octadecene (ODE) to get a 0.5 M Cd oleate solution in ODE (solution 1) and a 0.5 M TOP:S solution in ODE (solution 2). In a 25 mL tri-neck flask a mixture of 3 mL of ODE and 1 mL of CdS cores solution was first degassed at 80°C under vacuum to remove water. Then, under nitrogen, the solution was heated to 300°C and a mixture of solution 1 and solution 2 (0.65 mL each) was injected into the system drop by drop in 1 hour, targeting a shell thickness of 2.35 nm, corresponding to the growth of 7 CdS monolayers (each layer having a thickness of 0.3358 nm, which is equivalent to half the lattice parameter along the crystallographic *c* axis). The final sample was washed by centrifugation and re-dissolution with toluene and 2-propanol (3 times) and finally suspended in 3 mL of toluene.

The synthesized CdS cores and final CdS@CdS NCs were characterized by means of Transmission Electron Microscopy (TEM) and images were acquired on a JEOL JEM-1011 microscope equipped with a thermionic gun at 100 kV accelerating voltage (see Figure 3.13a and c, respectively).

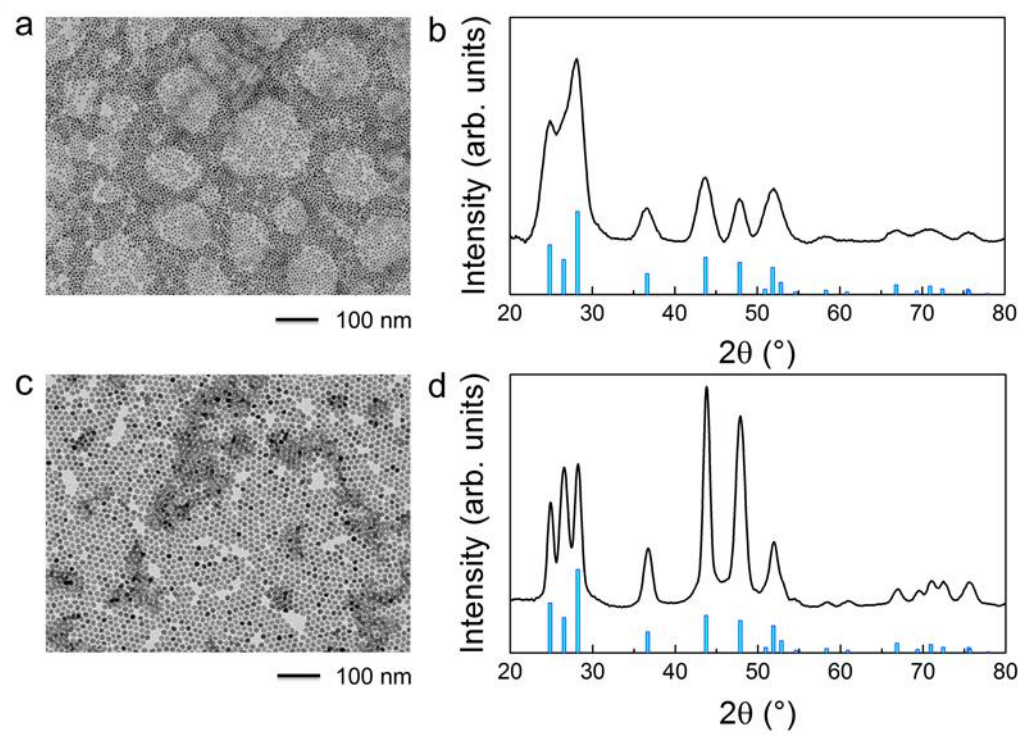


**Figure 3.13: a)** TEM images and **b)** XRD patterns of CdS cores. **c)** TEM images and **d)** XRD patterns of CdS@CdS Giant Shell NCs.

As evident from TEM characterizations, the two samples are quite monodisperse, with an average size of (5.6 ± 0.4) nm and (10.2 ± 0.6) nm for the CdS cores and the CdS@CdS Giant Shell NCs, respectively.

In order to obtain a composition analysis of the synthesized NCs powder X-Ray Diffraction (XRD) patterns were acquired using a PANalytical Empyrean X-ray diffractometer equipped with a 1.8 kW Cu Kα ceramic X-ray tube, PIXcel3D 2×2 area detector and operating at 45 kV and 40 mA. The diffraction patterns were collected in air at room temperature using a Parallel-Beam (PB) geometry and symmetric reflection mode. All XRD samples were prepared by drop casting a concentrated solution on a zero diffraction silicon wafer. XRD patterns confirm the crystallinity of both samples (Figure 3.13b for cores and 3.8d for core-shell NCs), showing an excellent match with reference card ICSD 98-015-4186, corresponding to the hexagonal wurtzite structure with $a = b = 4.1365$ Å and $c = 6.7160$ Å lattice parameters. Moreover, the absence of other peaks related to different phases and to precursors residues certifies the high purity of the used samples.

The concentration of the NCs solutions obtained following the previously described protocols was retrieved *via* Inductively Coupled Plasma Optical Emission Spectroscopy (ICP-OES). ICP-OES

analysis performed on an iCAP 6000 spectrometer (ThermoScientific) was used to estimate the concentrations of CdS cores and CdS@CdS Giant Shell NCs solutions. Prior to measurements, the samples were decomposed in aqua regia ($HCl/HNO_3$ = 3/1 (v/v)) overnight. The measured CdS core concentration was 34.24 μM, while the concentration of CdS@CdS Giant Shell NCs in the final sample solution was 10.95 μM.

The NCs we synthesized are endowed with 3 main phonon lines: the transverse optical (TO) and longitudinal optical (LO) phonon modes ($\nu_{TO} \approx 6.9$ THz, $\nu_{LO} \approx 9.1$ THz), which are also characteristic of bulk crystalline CdS, as well as a Fröhlich (FR) optical phonon resonance ($\nu_{FR} \approx 7.85$ THz), typical of nanoparticles[28], which lies between the TO and LO lines. The FR mode of the NCs is associated with a dipolar charge distribution on the surface of the nanoparticle and thus, being dipole-active, can be effectively coupled to electromagnetic radiation. This kind of resonance can be stimulated in polar dielectric crystals between the TO and LO phonon frequencies, in the spectral range denoted as "Reststrahlen" band[28]. Similarly to metals for frequencies lower than the plasma frequency, polar dielectric crystal exhibit high reflectivity and negative real part of the permittivity in the Reststrahlen band, as a result of coherent oscillations of the vibrating bound charges on the atomic lattice (optic phonons). Even for polar nanocrystals as CdS, the dispersion relation can be approximated as a Lorentz oscillator:

$$\varepsilon(\omega) = \varepsilon_\infty \left(1 + \frac{\omega_{LO}^2 - \omega_{TO}^2}{\omega_{TO}^2 - \omega^2 - i\omega\gamma}\right) \tag{57}$$

where γ is a damping constant, $\varepsilon_\infty$ is the high-frequency dielectric permittivity and $\omega_{LO}$, $\omega_{TO}$ the LO and TO phonon frequencies, respectively. Between these two frequencies the permittivity is negative and both localized and propagating surface phonon polariton modes can be supported on the surface of the NCs as it happened for LSPs and SPPs in metals.

In order to describe the NCs response at THz frequencies, we considered an effective permittivity $\varepsilon_{eff}$ derived from the Maxwell-Garnett approximation for a dielectric mixture:

$$\frac{\varepsilon_{eff} - \varepsilon_b}{\varepsilon_{eff} + 2\varepsilon_b} = f\frac{\varepsilon_{CdS} - \varepsilon_b}{\varepsilon_{CdS} + 2\varepsilon_b} \tag{58}$$

where $\varepsilon_b$ and $\varepsilon_{CdS}$ are the permittivities of the background (air in our case, $\varepsilon_b = 1$) and filling (CdS NCs) materials, while $f$ is a dimensionless quantity representing the filling ratio of the mixture, which was found to well reproduce the experimental data for a value around 0.75. Using literature values[29] for bulk crystalline CdS and the dispersion equation (57), we were able to simulate the transmittance and the absorption of our NCs (Figure 3.14a-b), finding very good agreement with the experimental measurements (see next chapter).

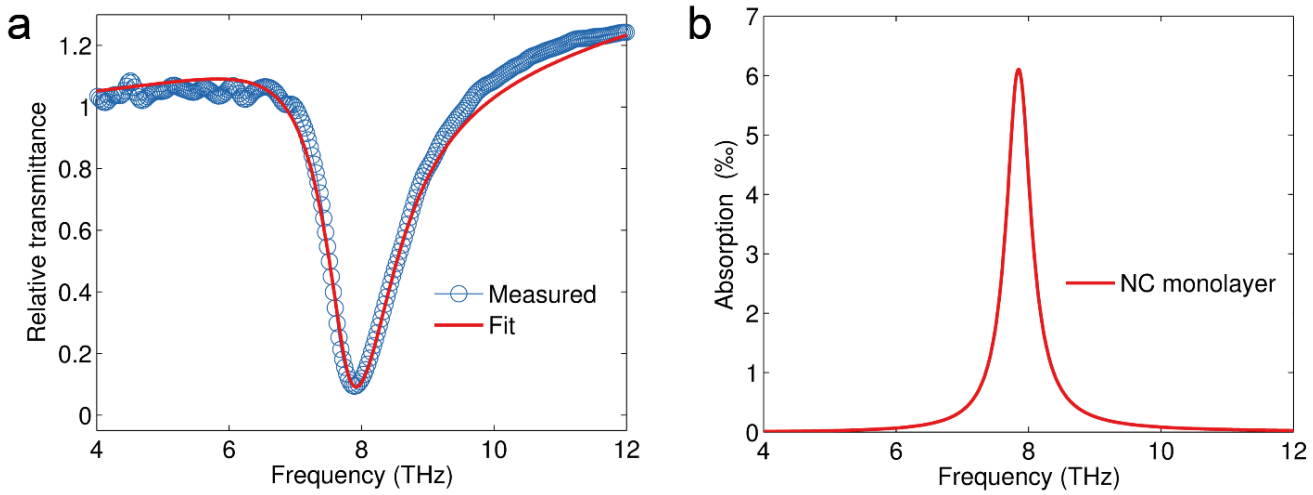


**Figure 3.14: a)** Relative transmittance spectra (blue circles: experimental measurement, red line: fit using Eq. (57)) of a 2.5 μm thick CdS NC layer. The relative transmittance is obtained normalizing the sample transmission with the one of a bare silicon substrate. **b)** Absorption spectrum of a monolayer of CdS NCs, as obtained using Eq. (57) and the parameters extracted from the fit in **a)**.

The Fröhlich resonance position is independent on structural deviations of the NCs from the original shape, as well as on different arrangements or densities. In order to demonstrate this, we have performed a series of numerical simulations and retrieved the Fröhlich resonance peak of ensembles of nanocrystals in various conditions. The results of this investigation are summarized in the following figures. Changes in the shape of individual nanocrystals, as well as in the 2D lattice arrangement, have basically no effect on the resonance position (Figure 3.15a-d). Also large changes in the size of NCs do not shift or perturb the Fröhlich resonance (Figure 3.15e), which is just affected only by changes in the filling factor $f$ (Figure 3.15f), whose value however was both experimentally and numerically verified to be close to 0.75.

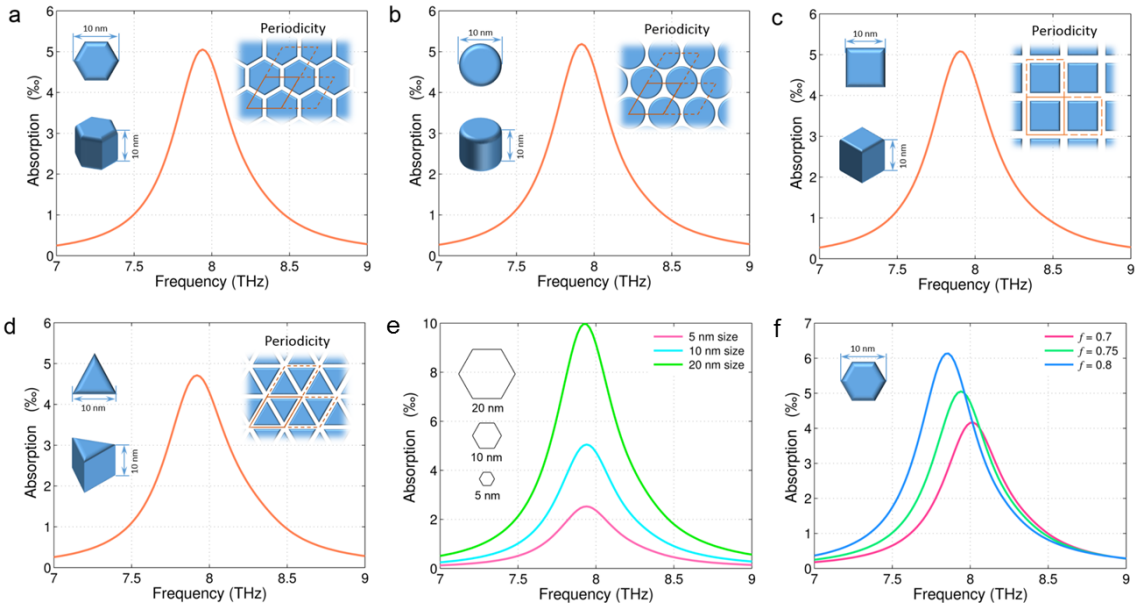


**Figure 3.15: a-d)** Fröhlich resonance peak retrieved by means of numerical simulations for different nanocrystal shapes and lattice arrangements (filling factor $f$ = 0.75). **e)** Fröhlich resonance for different nanocrystal size and **f)** different filling factors.

## 3.4 Coupled system

The deposition of the CdS nanocrystals on the fabricated nanoantenna array was carried out *via* spin-coating under ambient conditions and at room temperature. Specifically, the 10.95 μM solution obtained after the synthesis, was diluted to a final NCs concentration of 1 μM. Then, 20 μL of the diluted solution were spin cast onto the patterned substrate at 2000 rpm for 60 s (acceleration of 1000 rpm/s).

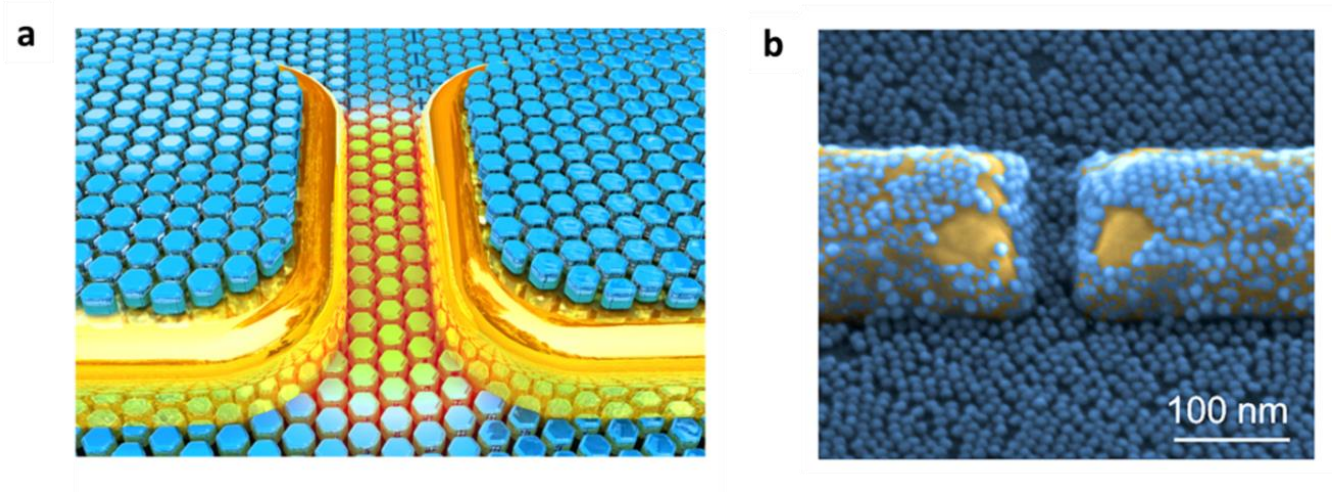


**Figure 3.16: a)** Graphical representation and **b)** SEM image (in false colours) of a nanocavity region covered with a monolayer of NCs; scale bar 100 nm.

The procedure resulted in the deposition of a uniform monolayer of CdS@CdS Giant Shell NCs that well covers the sample surface, even within the antenna nanocavities, as shown in Figure 3.16a-b.

In order to explore how the plasmon-phonon strong coupling is affected by the number of NCs interacting with the plasmonic nanostructures, we followed a specific protocol to add additional NCs. Thicker layers were obtained through multi-step layer-by-layer spin coating deposition; to avoid complete re-dissolution of the already deposited NCs, spin coating steps were interspersed with exposure of the sample to 20 μL of TBAI solution in methanol (10 mg/mL) for 30 s, followed by three rinse-spin steps with methanol, as described in Ref.[30]. The results of this deposition protocol for different NC numbers are summarized in Figure 3.17, where representative SEM images are shown.

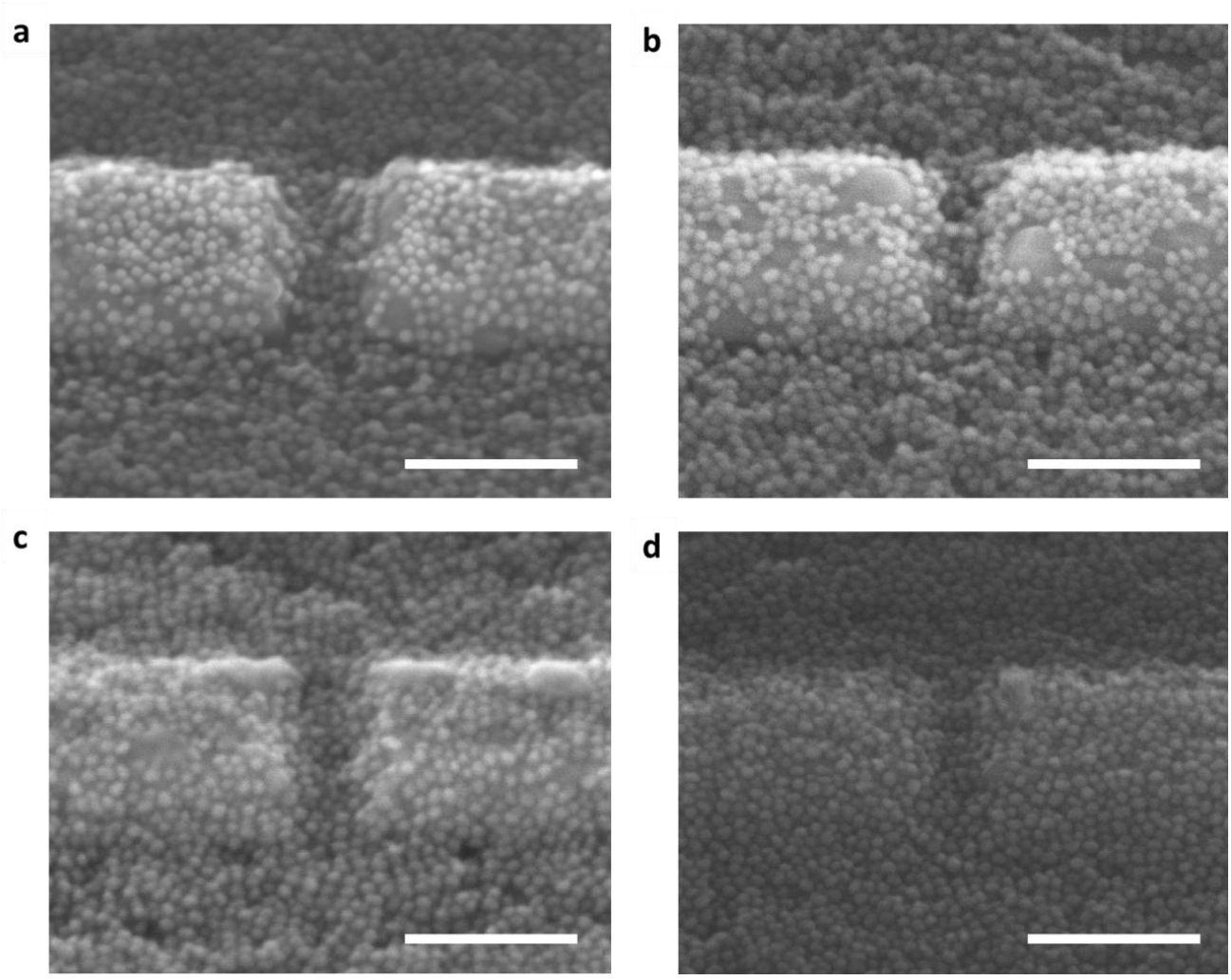


**Figure 3.17: a) - d)** Increasing number of CdS NCs deposited on the pre-existent layers; scale bar 100 nm.

The spectral response of each measured nanogap was expressed in terms of the average number of NC layers. For each nanocavity, several SEM images taken with different tilt angles were considered, in order to evaluate their stacking in the case of multiple layers. From the average number of NCs obtained for the reference case of the monolayer $n_{avg}^{1}$ (calculated over 20-30 nanogaps), we then estimated the number of layers $N_{EST}$ using the following formula

$$N_{EST} = \frac{n_{avg}}{n_{avg}^{1}} \tag{59}$$

where $n_{avg}$ is the average number of NCs extracted for the different sample coverage conditions investigated in our work. This estimation protocol, however, is intrinsically operator dependent. We

therefore employed an alternative and more objective procedure by means of Electron Dispersive X-Ray (EDX) measurements. For this purpose, we used a FEI Helios NanoLab 650 microscope working at an accelerating voltage V = 5 kV, current I = 0.4 nA and acquisition time 120s. SEM images of the nanogaps were collected with 250'000x magnification, in order to include the CdS NCs as well as the gold edges of the nanocavities. A typical spectrum obtained by EDX investigation and the results of the analysis carried out on three different nanogaps with similar NC coverage are reported in Figure 3.18.

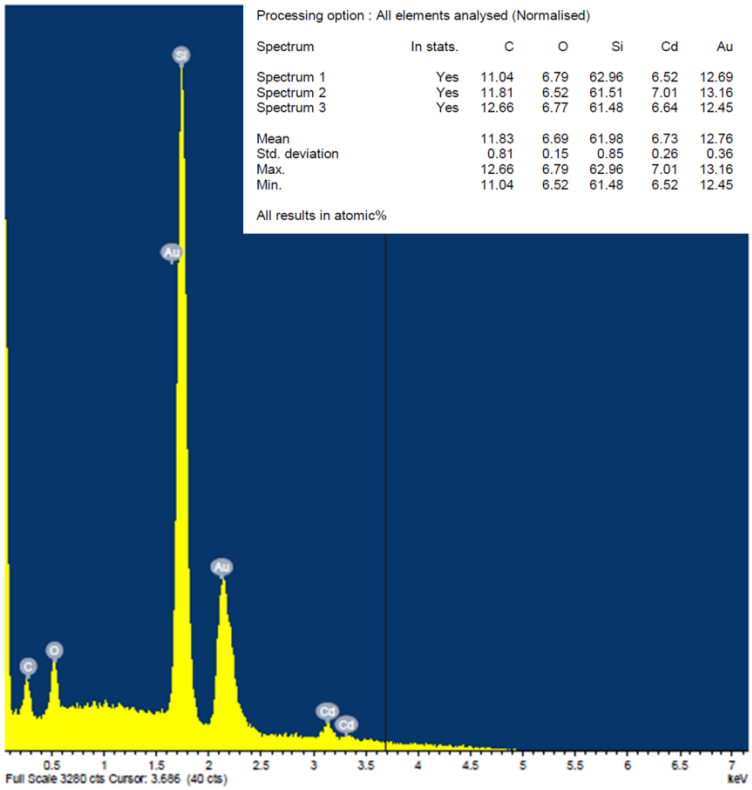


**Figure 3.18:** Typical EDX spectrum obtained over a nanocavity and featuring peaks in correspondence of each element characteristic X-ray energy. The inset summarizes the results in relative atomic fraction obtained over three nanocavities with similar NC coverage.

The relative atomic fractions of Cd and Au extracted from the EDX measurements taken in such configuration were then used to estimate the equivalent number of NC layers, by fixing as a reference ($N_{EDX} = 1$) the case of a monolayer.

## 3.5 Other applications of the same design

The nanoantenna-semiconductor NCs design, that we have used in the present study, was already exploited in previous works[21,31] for sensing applications in the IR and THz spectral range. Usually, the large wavelength associated with THz radiation (300 μm at 1 THz) severely hinders its interaction with nano-objects (i.e nanoparticles, nanorods and large molecules), thus limiting investigations to macroscopic ensembles of these compounds, in the form of thick pellets of crystallized molecules or highly concentrated solutions. However, the high field enhancement and localization in plasmonic "hot-spots" associated to resonant nanoantennas allow detection of small amounts of molecules and characterization of their optical response even in this frequency range. Localized surface plasmon resonances of metallic nanoclusters have proven to be capable of effectively enhancing the optical response of NCs thin films, showing a clear potential for enhanced spectroscopy in the IR range.

Thanks to these properties, Toma et al.[21] exploited nano-engineered dipole nanoantennas coupled end-to-end (see Figure 3.19a-b) to retrieve the spectroscopic response of a monolayer of cadmium selenide (CdSe) nanocrystals, which are endowed with a phonon resonance in the THz spectral range (at 5.65 THz). In this study, the THz response of the coupled system was characterized by means of Fourier transform spectroscopy in transmission configuration and the plasmonic nanoantennas were carefully engineered to support a resonant mode located in proximity of the CdSe phonon resonance position (see Figure 3.19c, green curve and dotted line). When the polarization of THz light was set perpendicular to the long axis of the nanoantennas (non-resonant illumination) the overall transmission was found to be the same of a bare silicon substrate, and the presence of the QDs could not be detected (see black curve in Figure 3.19c). When instead the sample was resonantly illuminated (in order to excite the dipole mode of the antennas), a modified array response was observed (see Figure 3.19c, red curve), highlighting a particular spectral feature superimposed on the array resonance. The appearance of this peculiar feature as an extra transmission peak in the measured spectra can be ascribed to the Fano interference between the broad nanoantenna resonance and the sharp QD phonon resonance. The sensing of a monolayer of QDs, through the formation of a Fano-like resonance, is made possible by significant absorption enhancement (with a factor as high as $10^6$ in the present case) induced by the nanoantennas. In fact, in the close proximity of the gap, the usually small effective absorption cross-section of a nano-object at THz frequencies can be greatly amplified, making this design suitable for successful applications in enhanced THz spectroscopy of nanomaterials.

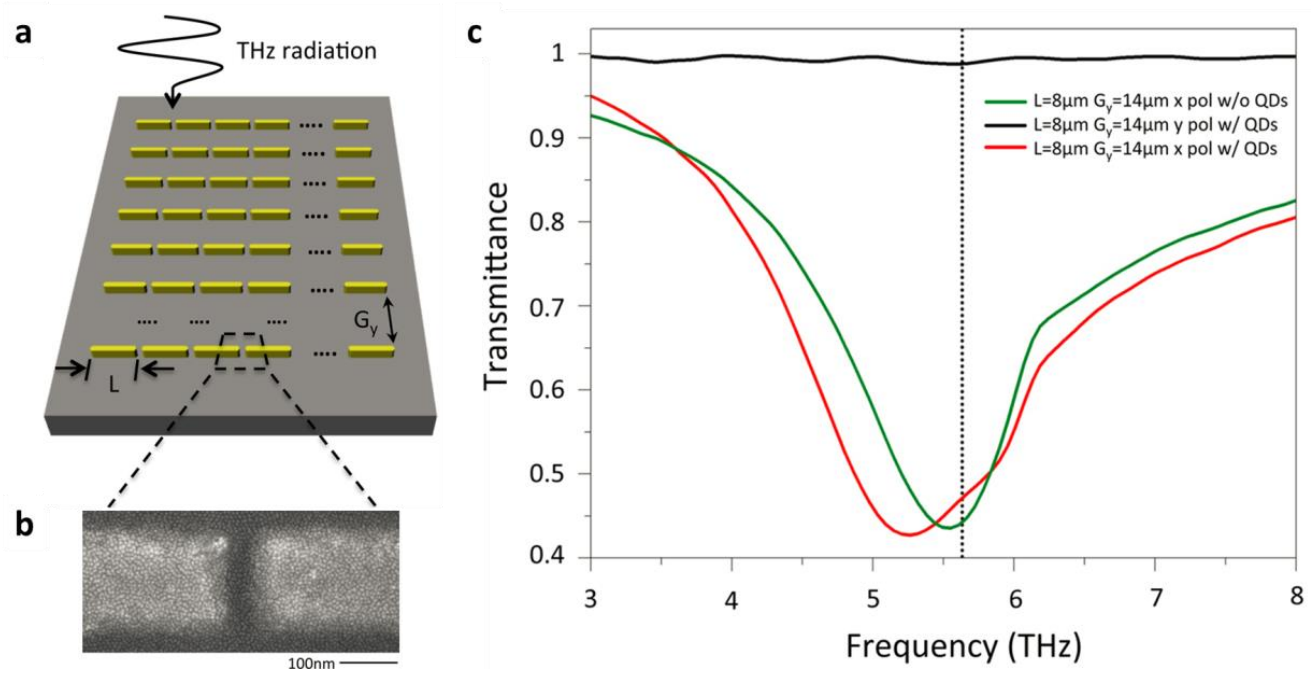


**Figure 3.19: a)** Sketch of the THz nanoantenna array. **b)** SEM image of a CdSe monolayer uniformly deposited in the nanogap region. **c)** Transmittance of the array with nanoantenna length $L$ = 8 μm and periodicity $G_y$ = 14 μm for THz polarization set along the nanoantenna long axis and without QDs over the surface (green curve); transmittance of the same array covered with a QD monolayer, for THz polarization set along the nanoantenna short axis (black curve) and long axis (red curve). The vertical dotted line denotes the unperturbed CdSe phonon resonance.

In a recent work, Milekhin et al.[31] exploited the same design to further maximize the NC response in Surface Enhanced Infrared Absorption (SEIRA) measurements by superimposing plasmonic and diffraction resonances in the periodic nanoantenna structures. In particular, they studied the dependence of the measured signal on the periodicity of the fabricated structures, while keeping fixed the antenna dipolar LSPR (set by their length). By doing this, they were therefore able to determine an optimal configuration associated with maximal enhancement of both the electromagnetic near field and IR absorption (see Figure 3.20a-b).

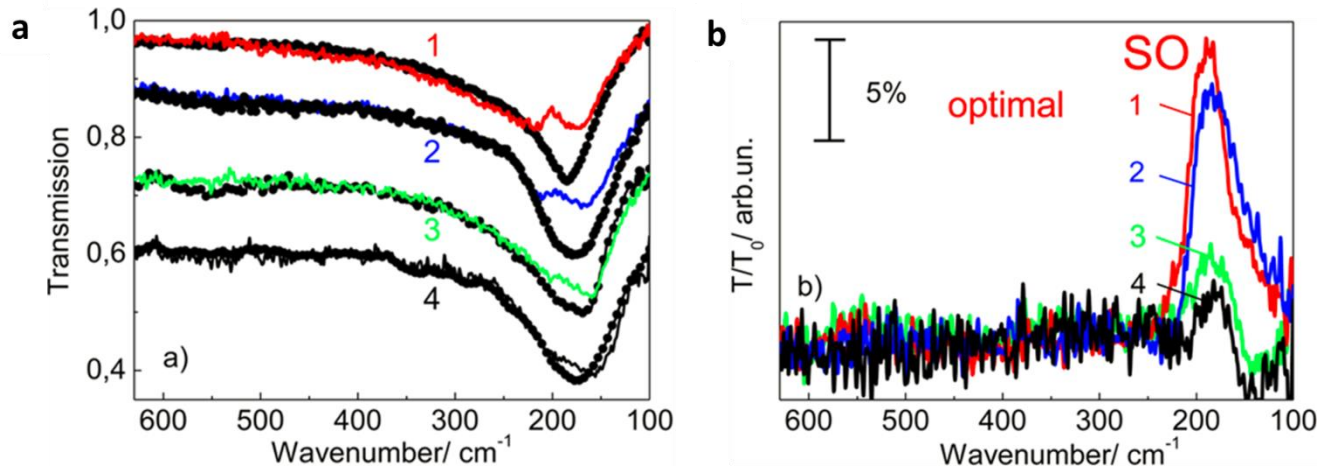


**Figure 3.20: a)** IR transmission spectra of an optimized Au nanoantenna array (curve 1) and of arrays with the transverse periodicity $G_y$ reduced by 20% (curve 2) and increased by 20% (curve 3) and 50% (curve 4) relative to the optimal value before depositing NCs (solid lines with circles) and after covering with 1ML of CdSe NCs (solid lines). **b)** The same spectra after normalization.

In the two examples presented above, a modification in the optical properties of the coupled system was observed, resulting in a resonance shift and the appearance of a spectral feature attaining to the NCs. In both situations however, the interaction strength is not big enough to overcome the relaxation rates of both the plasmonic elements and the semiconductor quantum dots.

In this context, our aim is to properly engineer a system supporting strong light-matter interactions, enabling the intrinsic properties of few tens of NCs to be drastically modified through the formation of hybrid plasmon-phonon polariton states.

## References


[1] Shelton, D. J., Brener, I., Ginn, J. C., Sinclair, M. B., Peters, D. W., Coffey, K. R.., Boreman, G. D., "Strong Coupling between Nanoscale Metamaterials and Phonons," Nano Lett. **11**(5), 2104–2108 (2011).

[2] Marty, R., Mlayah, A., Arbouet, A., Girard, C., Tripathy, S., "Plasphonics : local hybridization of plasmons and phonons," Opt. Express **21**(4), 4551–4559, OSA (2013).

[3] Luxmoore, I. J., Gan, C. H., Liu, P. Q., Valmorra, F., Li, P., Faist, J.., Nash, G. R., "Strong Coupling in the Far-Infrared between Graphene Plasmons and the Surface Optical Phonons of Silicon Dioxide," ACS Photonics **1**(11), 1151–1155 (2014).

[4] Jia, Y., Zhao, H., Guo, Q., Wang, X., Wang, H.., Xia, F., "Tunable Plasmon–Phonon Polaritons in Layered Graphene–Hexagonal Boron Nitride Heterostructures," ACS Photonics **2**(7), 907–912 (2015).

[5] Yu, J.-K., Mitrovic, S., Tham, D., Varghese, J.., Heath, J. R., "Reduction of thermal conductivity in phononic nanomesh structures," Nat. Nanotechnol. **5**, 718, Nature Publishing Group (2010).

[6] Chen, H.., Chan, C. T., "Acoustic cloaking in three dimensions using acoustic metamaterials," Appl. Phys. Lett. **91**(18), 183518 (2007).

[7] Guenneau, S., Amra, C.., Veynante, D., "Transformation thermodynamics: cloaking and concentrating heat flux," Opt. Express **20**(7), 8207–8218, OSA (2012).

[8] Li, B., Wang, L.., Casati, G., "Thermal Diode: Rectification of Heat Flux," Phys. Rev. Lett. **93**(18), 184301, American Physical Society (2004).

[9] Hochbaum, A. I., Chen, R., Delgado, R. D., Liang, W., Garnett, E. C., Najarian, M., Majumdar, A.., Yang, P., "Enhanced thermoelectric performance of rough silicon nanowires," Nature **451**, 163, Nature Publishing Group (2008).

[10] Irmer, G., Monecke, J.., Verma, P., "Light Scattering of Semiconducting Nanoparticles," Encycl. Nanosci. Nanotechnol., 1–26.

[11] Shalabney, A., George, J., Hutchison, J., Pupillo, G., Genet, C.., Ebbesen, T. W., "Coherent coupling of molecular resonators with a microcavity mode," Nat. Commun. **6**, 5981, Nature Pub. Group (2015).

[12] George, J., Shalabney, A., Hutchison, J. A., Genet, C.., Ebbesen, T. W., "Liquid-Phase Vibrational Strong Coupling," J. Phys. Chem. Lett. **6**(6), 1027–1031, American Chemical Society (2015).

[13] Thomas, A., George, J., Shalabney, A., Dryzhakov, M., Varma, S. J., Moran, J., Chervy, T., Zhong, X., Devaux, E., et al., "Ground-State Chemical Reactivity under Vibrational Coupling to the Vacuum Electromagnetic Field," Angew. Chemie **128**(38), 11634–11638 (2016).

[14] Vergauwe, R. M. A., George, J., Chervy, T., Hutchison, J. A., Shalabney, A., Torbeev, V. Y.., Ebbesen, T. W., "Quantum Strong Coupling with Protein Vibrational Modes," J. Phys. Chem. Lett. **7**(20), 4159–4164 (2016).

[15] Shalabney, A., George, J., Hiura, H., Hutchison, J. A., Genet, C., Hellwig, P.., Ebbesen, T. W., "Enhanced Raman Scattering from Vibro-Polariton Hybrid States," Angew. Chemie Int. Ed. **54**(27), 7971–7975 (2015).

[16] del Pino, J., Feist, J.., Garcia-Vidal, F. J., "Signatures of Vibrational Strong Coupling in Raman

Scattering," J. Phys. Chem. C **119**(52), 29132–29137, American Chemical Society (2015).

[17] del Pino, J., Feist, J.., Garcia-Vidal, F. J., "Quantum theory of collective strong coupling of molecular vibrations with a microcavity mode," New J. Phys. **17**(5), 53040 (2015).

[18] Kerfoot, M. L., Govorov, A. O., Czarnocki, C., Lu, D., Gad, Y. N., Bracker, A. S., Gammon, D.., Scheibner, M., "Optophononics with coupled quantum dots," Nat. Commun. **5**, 3299, Nature Publishing Group, a division of Macmillan Publishers Limited. All Rights Reserved. (2014).

[19] Hameau, S., Guldner, Y., Verzelen, O., Ferreira, R., Bastard, G., Zeman, J., Lema\^\itre, A.., Gérard, J. M., "Strong Electron-Phonon Coupling Regime in Quantum Dots: Evidence for Everlasting Resonant Polarons," Phys. Rev. Lett. **83**(20), 4152–4155, American Physical Society (1999).

[20] Huck, C., Vogt, J., Neuman, T., Nagao, T., Hillenbrand, R., Aizpurua, J., Pucci, A.., Neubrech, F., "Strong coupling between phonon-polaritons and plasmonic nanorods," Opt. Express **24**(22), 25528–25539, OSA (2016).

[21] Toma, A., Tuccio, S., Prato, M., De Donato, F., Perucchi, A., Di Pietro, P., Marras, S., Liberale, C., Proietti Zaccaria, R., et al., "Squeezing Terahertz Light into Nanovolumes: Nanoantenna Enhanced Terahertz Spectroscopy (NETS) of Semiconductor Quantum Dots," Nano Lett. **15**(1), 386–391, American Chemical Society (2015).

[22] Walther, M., Cooke, D. G., Sherstan, C., Hajar, M., Freeman, M. R.., Hegmann, F. A., "Terahertz conductivity of thin gold films at the metal-insulator percolation transition," Phys. Rev. B **76**(12), 125408, American Physical Society (2007).

[23] Zilio, P., Malerba, M., Toma, A., Zaccaria, R. P., Jacassi, A.., Angelis, F. De., "Hybridization in Three Dimensions: A Novel Route toward Plasmonic Metamolecules," Nano Lett. **15**(8), 5200–5207, American Chemical Society (2015).

[24] Kravets, V. G., Schedin, F.., Grigorenko, A. N., "Extremely Narrow Plasmon Resonances Based on Diffraction Coupling of Localized Plasmons in Arrays of Metallic Nanoparticles," Phys. Rev. Lett. **101**(8), 87403, American Physical Society (2008).

[25] Yoshie, T., Scherer, A., Hendrickson, J., Khitrova, G., Gibbs, H. M., Rupper, G., Ell, C., Shchekin, O. B.., Deppe, D. G., "Vacuum Rabi splitting with a single quantum dot in a photonic crystal nanocavity," Nature **432**, 200, Macmillian Magazines Ltd. (2004).

[26] Koenderink, A. F., "On the use of Purcell factors for plasmon antennas," Opt. Lett. **35**(24), 4208–4210, OSA (2010).

[27] Christodoulou, S., Vaccaro, G., Pinchetti, V., De Donato, F., Grim, J. Q., Casu, A., Genovese,

A., Vicidomini, G., Diaspro, A., et al., “Synthesis of highly luminescent wurtzite CdSe/CdS giant-shell nanocrystals using a fast continuous injection route,” J. Mater. Chem. C **2**(17), 3439–3447, The Royal Society of Chemistry (2014).

[28] Caldwell, J., Lindsay, L., Giannini, V., Vurgaftman, I., Reinecke, T., Maier, S.., Glembocki, O., Nanophotonics., 68, De Gruyter (2014).

[29] Adachi, S., Optical constants of crystalline and amorphous semiconductors: numerical data and graphical information, Springer Science & Business Media (1999).

[30] Chuang, C.-H. M., Brown, P. R., Bulović, V.., Bawendi, M. G., “Improved performance and stability in quantum dot solar cells through band alignment engineering,” Nat. Mater. **13**, 796, Nature Publishing Group (2014).

[31] Milekhin, A. G., Kuznetsov, S. A., Sveshnikova, L. L., Duda, T. A., Milekhin, I. A., Rodyakina, E. E., Latyshev, A. V., Dzhagan, V. M.., Zahn, D. R. T., “Surface-Enhanced Infrared Absorption by Optical Phonons in Nanocrystal Monolayers on Au Nanoantenna Arrays,” J. Phys. Chem. C **121**(10), 5779–5786, American Chemical Society (2017).

# Chapter 4

# Plasmon-phonon strong coupling *via* plasmonic nanoantennas

## 4.1 THz characterization

Far from the resonance matching conditions, i.e. for nanoantenna resonances strongly detuned from the phonon resonance of the NCs, the spectral response of the overall system resembles that of two uncoupled oscillators with their energy levels unperturbed. As the plasmon resonance approaches the QD Fröhlich mode, the interaction strength between the two constituents increases and hybridization starts to occur. At the overlap of the investigated resonances energy is exchanged at a rate faster than any relaxation rate and the system enters the strong coupling regime. The energy spectrum of the coupled pair is profoundly modified (see energy hybridization scheme in Figure 4.1a) and new hybrid light-matter states are formed, identified as two polariton modes $\nu_-$ and $\nu_+$, as evidenced in the THz extinction spectra of the nanoantennas (see red curve in Figure 4.1b).

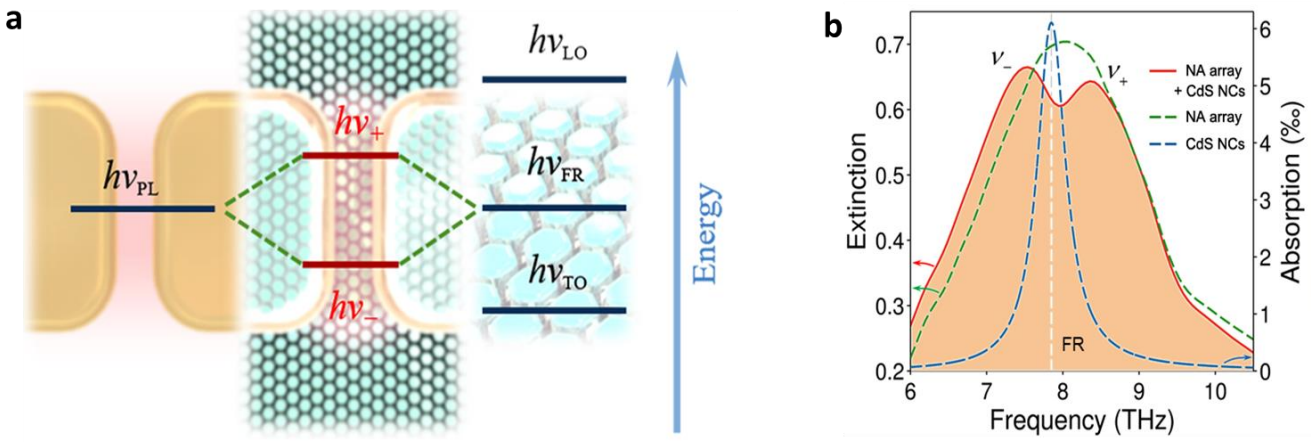


**Figure 4.1: a)** Energy diagram exemplifying the plasmon-phonon resonance hybridization. **b)** Experimental THz extinction spectra of the array featuring nanoantennas of length L = 5.75 μm with (solid red line) and without (green dashed line) a NC monolayer over its surface; blue dashed line: absorption spectrum of a single layer of NCs.

THz transmission measurements of the overall system spectral response were performed using a Fourier-transform THz microscope coupled to synchrotron light (ELETTRA Trieste, SISSI beamline)[1]. The radiation is collected from the synchrotron storage ring (see Figure 4.2a) in correspondence of a bending magnet and is directed into a first ultra-high vacuum (UHV) chamber. Here a plane extraction mirror selects only the IR component of the synchrotron light, discarding the more energetic part. With the aid of an ellipsoid mirror the radiation is focused beyond the shielding wall of the synchrotron hall and enters a second UHV chamber. This optical design allows the aberrations by the transfer optics due to the wide emission angle to be minimized (for more details see Ref.[2,3]).

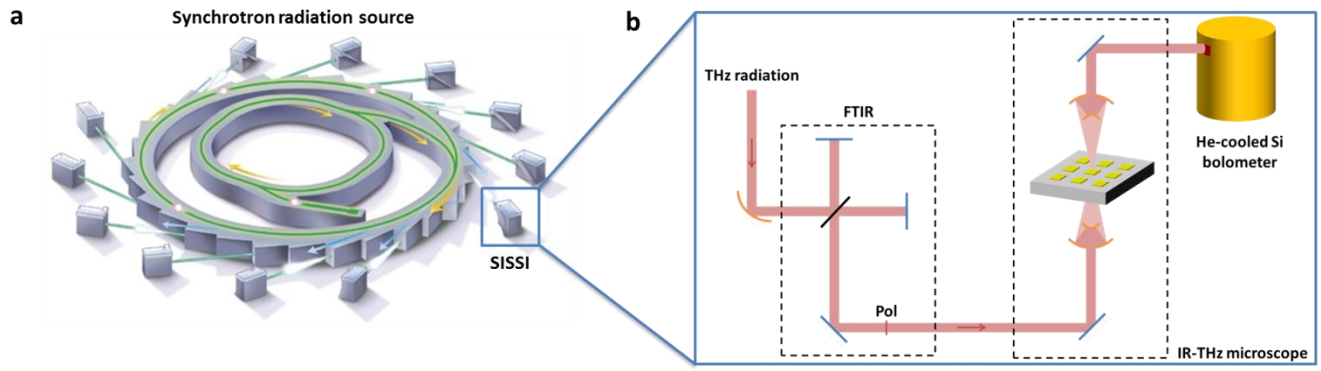


**Figure 4.2: a)** Illustration of the synchrotron scheme. At the center are the linear accelerator (Linac) and the circular accelerator (Booster), surrounded by the outer storage ring. **b)** Schematic view of the THz setup on the SISSI beamline.

The radiation is then propagated to the SISSI laboratory, where it enters a Bruker 70v FTIR spectrometer equipped with a Si beam splitter (see Figure 4.2b). Before going into the Hyperion infrared microscope, the light is passed through a grating polyethylene polarizer (denoted as Pol in Figure 4.2b) oriented along the main linear polarization axis of the synchrotron beam, corresponding to the electrons orbit plane.

Polarized transmittance measurements were performed by orienting the sample mounted on a goniometer, in such a way that the long axis of the nanoantennas was set parallel to the main polarization axis of the incident radiation. A Cassegrain objective (15X, mean incidence angle: 18°) was used to focus THz light onto the sample, while an aperture was employed to limit the focal spot size to a diameter of approximately 260 μm. The light transmitted from the sample was then directed towards a He-cooled Si bolometer, which is very sensitive in the investigated spectral range. Data were acquired by co-adding 512 scans with a spectral resolution of 4 $cm^{-1}$ (spectral point spacing of 2 $cm^{-1}$).

The acquired spectra were normalized to the transmission of the bare silicon substrate measured in correspondence of the un-patterned area of the samples.

In order to characterize the optical properties of the synthesized CdS NCs, preliminary THz transmission measurements were performed on a CdS thin film. Firstly, the transmission of a bare Si substrate was acquired as a reference spectrum and after that, a 2.5 μm thick NC film was drop-casted from a 10 μM solution. The optical response of the NC was normalized to the reference spectrum, so that to obtain their relative transmittance as shown in Figure 4.3. As it can be noticed, the synthesized NCs feature a strong dipole-active Fröhlich resonance located at 7.85 THz (gray dashed line), in good agreement with the numerical results reported in Chapter 3. The noise fluctuations visible at small frequencies are a results of lower detector sensitivity in this spectral range.

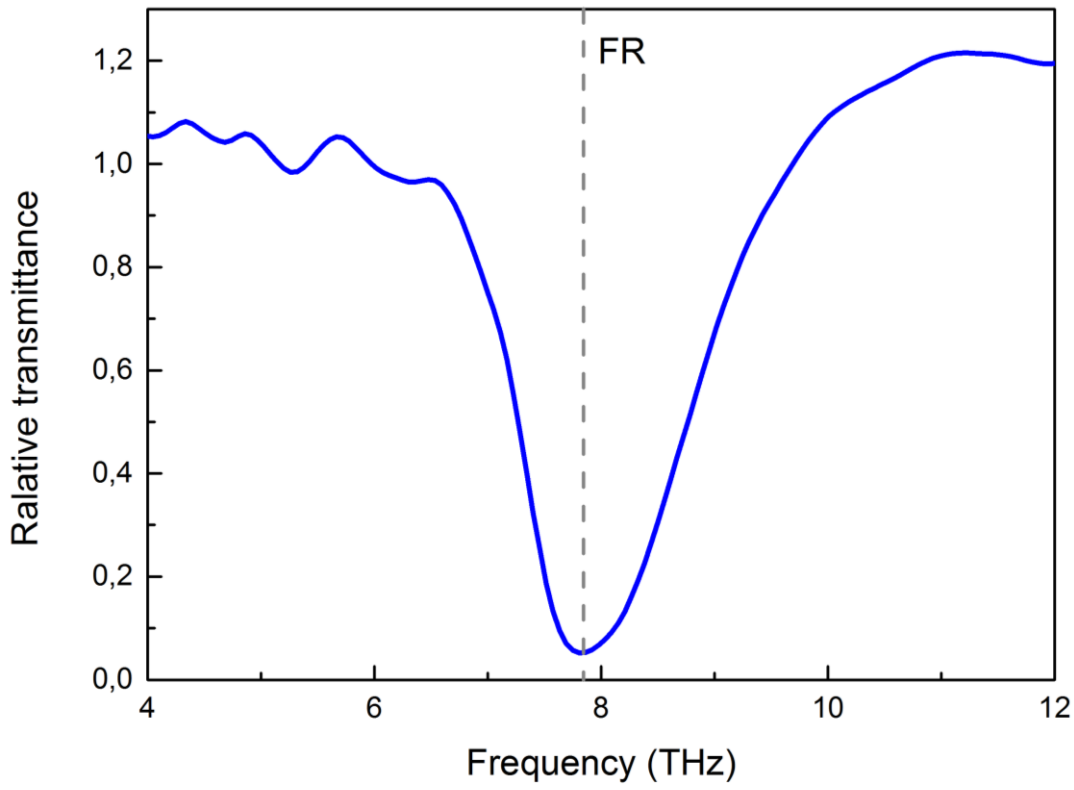


**Figure 4.3:** THz transmittance of CdS NCs deposited on a Si substrate. The NC response is normalized with respect to the transmission of a bare Si substrate. The vertical dashed line marks the position of the NC Fröhlich resonance.

In order to investigate the anti-crossing behaviour of the coupled system, we firstly measured the spectral response of the plasmonic arrays featuring different nanoantenna lengths *L* (see Figure 4.4a).

The measured resonances, appearing as a broad dip in the transmittance spectra, span a wide THz frequency band (from about 7 to 9 THz) comprising the Fröhlich phonon line. The kink visible at about 9.8 THz accounts for the presence of the arrays lattice mode and is indicated as a vertical dashed line. We then covered the fabricated arrays with a monolayer of CdS NCs (following the procedure described in Chapter 3) and we observed the arising of two hybrid dips at each side of the unperturbed phonon resonance (see Figure 4.4b).

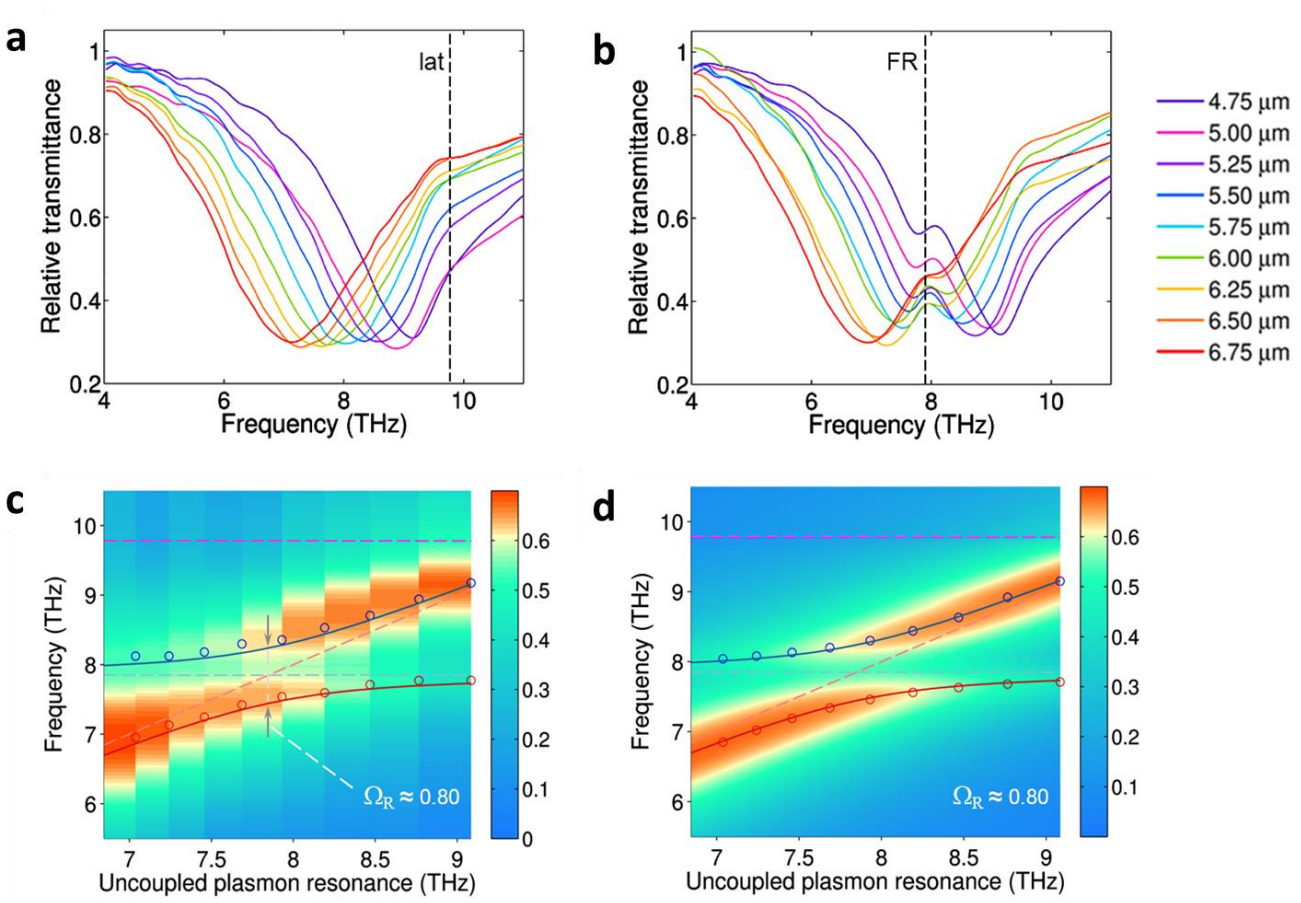


**Figure 4.4: a)** Transmission response of bare arrays featuring different nanoantenna lengths. The vertical dashed line (labeled "lat") marks the position of the lattice mode at around 9.8 THz. **b)** Same as in **(a)** when the arrays are covered with a single layer of NCs (dashed line: Fröhlich phonon resonance). **c) - d)** Experimental (**c)** and numerical **(d)** 2D maps of the polariton branches dispersion. The color bar corresponds to the values of the extinction *E*, extracted from the transmission *T* as $E = 1 - T$. The blue (red) solid lines are the trends of the high-energy (low-energy) polariton branch, as estimated by a three coupled oscillator model (see Appendix A), while the purple dashed line marks the lattice mode position.

The spectral position of these new features allowed us to reconstruct the dispersion of the hybrid polariton bands (see Figure 4.4c), which shows the characteristic anti-crossing behaviour of strongly

coupled systems. In fact, far from the phonon resonance of the NCs the two systems behave as uncoupled oscillators, following the spectral response of either the bare antennas (diagonal dashed line) or the unperturbed Fröhlich mode of the NCs (horizontal dashed line at 7.85 THz). As we approach the resonance matching conditions, the two dispersion curves do not intersect and anti-crossing is observed. For a CdS monolayer, the observed Rabi splitting $\Omega_R$ of the hybridized resonances, i.e. the separation of the two polariton branches when the uncoupled plasmon resonance is aligned to the uncoupled optical phonon mode, was estimated to be 0.8 THz. This value corresponds to about 10% of the unperturbed resonance and far exceeds the relaxation rates of the two systems, thus hinting for the establishment of a strong coupling regime. The same behaviour was also well reproduced by the results of the numerical simulations, as it is shown in Figure 4.4d. Finally, the horizontal dashed line located at 9.8 THz in the 2D dispersion maps represents the lattice mode of the nanoantenna arrays and does not affect the system behaviour, being far detuned from the Fröhlich mode.

In order to investigate how the plasmon-phonon strong coupling is affected by the number of NCs interacting with the plasmonic nanostructures, we followed a specific protocol (see Chapter 3) to add additional nanocrystals on top of the previously deposited monolayer. By direct visual inspection of several nanocavities and EDX analysis (described in Chapter 3), we were able to estimate an average number of layers $N_{EST} = 1.5$ deposited after the first overlayer deposition. A subsequent deposition step, instead, lead to an average value of $N_{EST} = 2.4$ over the sample surface. The results of the transmission measurements acquired after every NC deposition protocol are summarized in Figure 4.5a-b, which reports the 2D reconstruction of the polariton dispersion branches. The 2D maps show that the increase in the NC number results in a further splitting of the branches, as indeed expected for strongly coupled systems[4], reaching almost 15% of the uncoupled phonon resonance. The observed Rabi splitting for the two cases are reported in the 2D maps, together with the estimated average NC layers and the fitted values extracted from the numerical model.

Interestingly, the high-energy polariton branch in our measurements showed a peculiar dispersion at high frequencies and tends to intersect the uncoupled plasmon resonance line above 9 THz. We found that this is due to the presence in our system of a third characteristic resonance already introduced, the lattice mode of the arrays. Our overall system is thus better described by a three-oscillator model[5], i.e. involving plasmon, phonon and lattice resonances (see Appendix A), which well reproduces the observed pinning of the high-energy polariton branch. This behaviour is also confirmed by numerical simulations, as shown in Figure 4.5c-f for the case of $N$ = 1.5, 2, 2.5 and 3 NC layers, respectively.

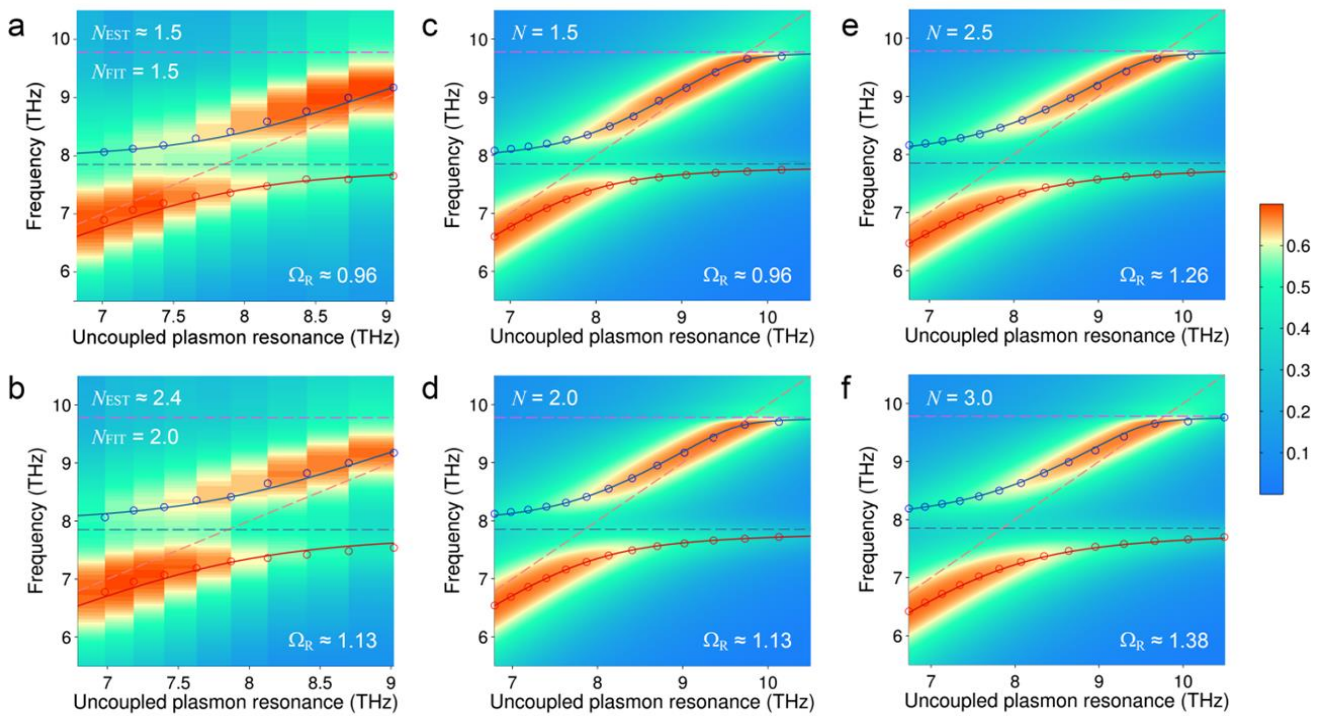


**Figure 4.5 a) - f)** Experimental (**a**,**b**) and numerical (**c**-**f**) 2D maps of the polariton branches dispersion for different values of NC layer number *N*. As a reference for the experimental data, $N_{EST}$ = 1 corresponds to an average number of NCs inside a nanocavity of around 86 (see below). The red (low-energy polariton) and blue (high-energy polariton) lines are the best fit with the three-coupled-oscillator (3CO) model, while the purple dashed line marks the lattice resonance position at 9.8 THz.

Even in the presence of the lattice resonance, the Rabi splitting $\Omega_R$ in our system is found to increase as $\sqrt{N}$, which is the typical trend of two strongly coupled oscillators[4] (as shown in Figure 4.6a). By exploiting this dependence in the fitting model, we extracted an estimate of the average increase of the number of NCs over the array surface (expressed as a fractional increase of the number of layers, see Chapter 3). We thus obtained the values corresponding to $N_{FIT}$ (and their associated Rabi splitting) reported in the table of Figure 4.6b. The different layers measured in the THz transmission experiments (see Figure 4.4c and 4.5a-b) were also characterized by direct SEM visual inspection and EDX analysis, in order to correlate the observed Rabi splitting to a corresponding average NC coverage *N*. In this respect, following the estimation procedure reported in Chapter 3, we were able to calculate three different average number of layers $N_{EST}$ (reported in Figure 4.6b) respectively. Indeed, EDX analysis performed on the same samples confirmed both the fitted and estimated values, following with

remarkable consistency the theoretically predicted power-law dependence. The average number of NC layers obtained *via* EDX analysis is reported in the table below as $N_{EDX}$.

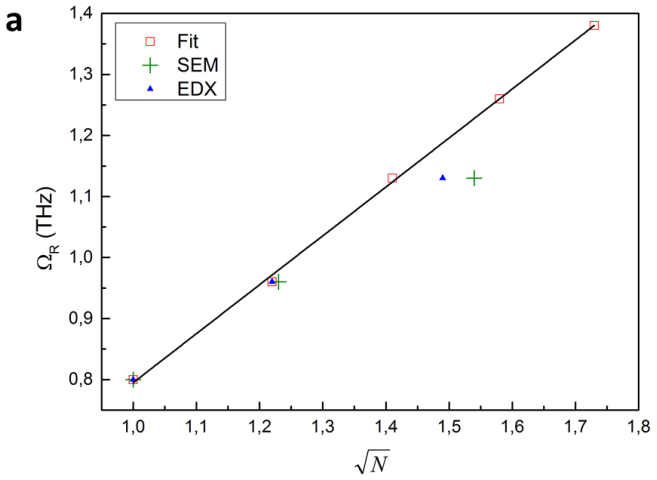


**b**

| $N_{FIT}$ | $\Omega_{R,FIT}$ | $n_{avg}$ | $N_{EST}$ | $N_{EDX}$ | $\Omega_{R,EXP}$ |
|---|---|---|---|---|---|
| 1.0 | 0.8 | $86.4 \pm 8.7$ | $1.00 \pm 0.14$ | $1.00 \pm 0.14$ | 0.8 |
| 1.5 | 0.9 | $130.1 \pm 11.4$ | $1.51 \pm 0.20$ | $1.49 \pm 0.26$ | 0.96 |
| 2 | 1.13 | $205.7 \pm 10.4$ | $2.38 \pm 0.27$ | $2.21 \pm 0.29$ | 1.13 |
| 2.5 | 1.26 | - | - | - | - |
| 3 | 1.38 | - | - | - | - |

**Figure 4.6: a)** Rabi splitting as a function of $\sqrt{N}$, extracted from: the three-coupled-oscillator model (black line), fitted model (red bordered squares), SEM visualization (green crosses) and EDX analysis (blue triangles). **b)** Values obtained from: the fitted model $N_{FIT}$ and their corresponding Rabi splitting $\Omega_{R,FIT}$**;** direct counting of the average NC number $n_{avg}$ and the extracted average NC layer number $N_{EST}$**;** EDX analysis $N_{EDX}$ with corresponding experimental Rabi splitting $\Omega_{R,EXP}$ obtained in the THz transmission measurements.

## 4.2 Raman characterization

In true strong coupling conditions, one expects the hybridization to occur also without the need of any THz illumination, thus in a so-called "dark" condition. In fact, the two involved oscillators should be coupled strongly just by means of the vacuum electromagnetic field, as the quantum description of the phenomenon predicts (see Chapter 1). While this quantum zero-point field is typically low in ordinary Fabry-Pérot THz nanocavity, as a consequence of the low radiation energy and big mode volumes, it can reach extreme values in our plasmonic nanocavities, which overcome diffraction limitations and feature a mode volume well below $\lambda^3/10^7$ (see Chapter 3 for exact calculation). To confirm this, we performed a micro-Raman characterization of the NCs located in the plasmonic nanocavity regions. Raman spectroscopy, by simply monitoring the frequency of visible light (632.8 nm laser excitation) inelastically scattered by the investigated system, can retrieve the phonon response without recurring to a direct THz illumination, i.e. no THz photons are injected in the nanocavities. Moreover, this technique allowed us to confirm the nanoscale nature of the phonon resonance reshaping, demonstrating that hybridization occurs only in the nanocavities, where the vacuum field is strongly

concentrated by the plasmonic nanoantennas. In fact, the Raman measurements performed differs from the THz characterization also for the size of the investigated region. While in the former we probed the phonon response over an area of about 1.4 $\mu m^2$ (dimension of the illuminated spot), therefore illuminating only one nanogap at a time, in THz extinction experiments we illuminated an area of about 200 x 200 $\mu m^2$ (corresponding to the nanoantenna arrays dimension), thus retrieving an averaged response of several hundred nanogaps (about 750 nanogap for the array with $L$ = 5.75 μm).

Raman investigation was performed in a backscattering configuration using a micro-spectrometer system (Renishaw inVia) equipped with a 150× LEICA PL APO objective (numerical aperture NA = 0.95) and a thermo-electrically cooled CCD as detector (working temperature -60 °C). Spectra were collected exciting the system at λ = 632.8 nm with a He:Ne laser; the excitation laser was chosen after optimization of the experimental conditions in terms of scattering efficiency, suppression of fluorescence emission from the CdS NCs (bandgap ~ 2.4 eV), and beam size at the diffraction limit. The laser power was fixed at 1.7 mW with an integration time of 10 seconds. The scan along the nanoantennas was performed using an XYZ motorized stage with a nominal 0.01 μm step. The polarization of the laser source was set by means of a half-waveplate (see Figure 4.7 illustrating the experimental setup), which allows to select a polarization either parallel or orthogonal to the nanoantenna long axis without moving the sample.

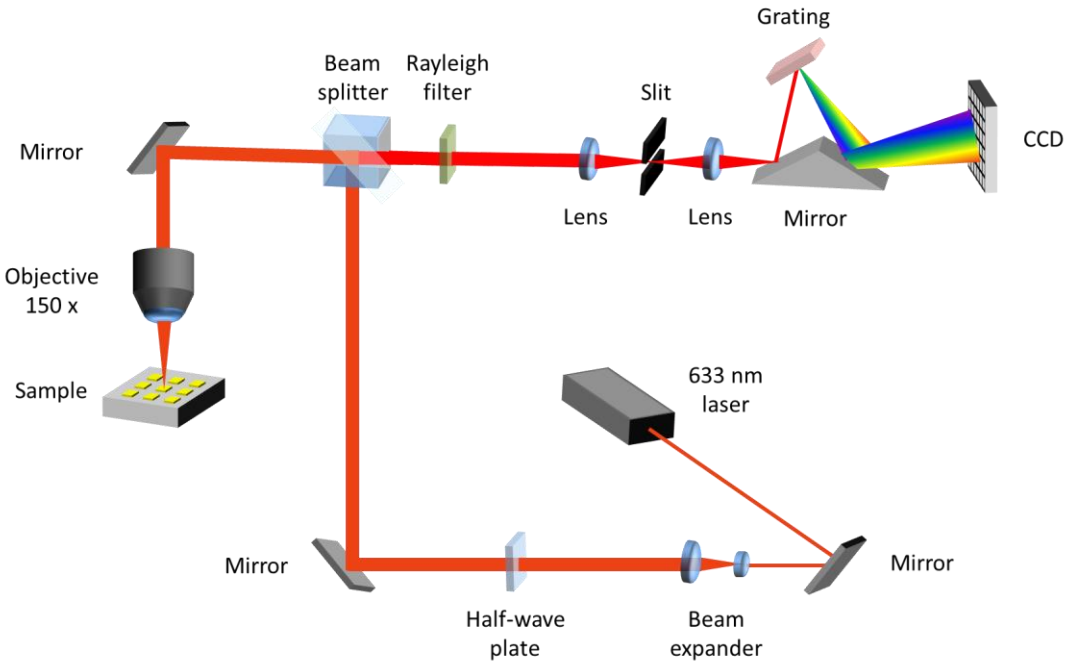


**Figure 4.7:** Schematic description of the Raman setup.

An example of Raman measurements obtained with a CdS monolayer is shown in Figure 4.8b, which emphasizes the difference between the spectrum collected in a nanocavity region (red continuous curve) and the spectrum obtained just outside the nanocavity on the Si substrate (green dashed curve). As can be seen, in the former two new peaks arise in the Raman spectrum at the two sides of the Fröhlich resonance and between the TO and LO modes of the nanocrystals, providing clear evidence of the creation of a new hybrid nanosystem with phonon properties that no longer belong to the original nanomaterial. Such modification of the Raman response is indeed remarkable, especially considering the fact that the focal spot of the micro-Raman system we employed (beam area: ~1.39 $\mu m^2$) is more than 200 times larger than the area covered by one nanocavity and thus illuminates not only the NCs within the nanocavity (about 90 per cavity), but also a large number of NCs that do not contribute to the hybridization (see pictorial representation in Figure 4.8a).

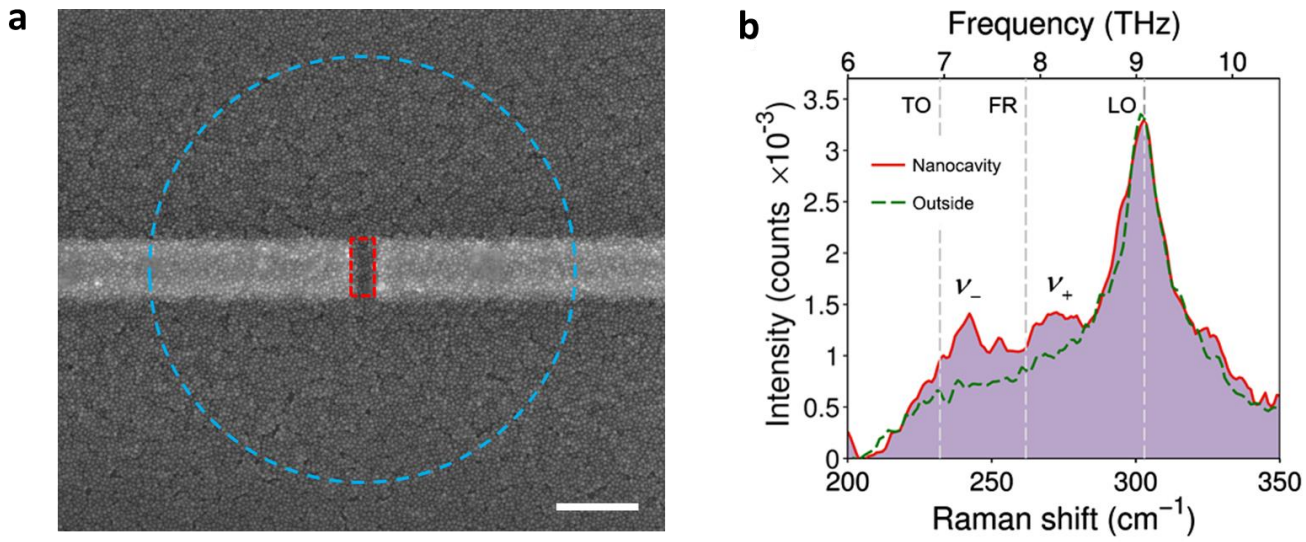


**Figure 4.8: a)** SEM image of the nanocavity region corresponding to the Raman signal in (**b**). The red bordered rectangle marks the nanogap region contributing to the hybridized signal, while the blue bordered circular area represents the focal spot; scale bar 200 nm. **b)** Raman spectra collected in the nanocavity region of (**a**) (solid red line) and just outside the nanocavity on the silicon substrate (green dashed line).

The comparison between the two curves in Figure 4.8b suggests that the Raman signature of the hybridized phonon resonance within the cavity is enhanced by about 2 orders of magnitude, which is consistent with what recently observed in the case of molecular bonds under strong vibrational coupling conditions[6–8]. In this respect, we considered the measured Raman signal $R_{MEAS}(\nu)$ in a

nanocavity region as the weighted average of the Raman response inside the nanocavity $R_{IN}(\nu)$ and the one outside the nanocavity $R_{OUT}(\nu)$, according to the following equation:

$$R_{MEAS}(\nu) = \frac{B - A}{B} R_{OUT}(\nu) + \frac{A}{B} R_{IN}(\nu) \tag{60}$$

where $A = 0.006$ μm$^2$ is the area of a nanocavity and $B = 1.39$ μm$^2$ is the spot size of the Raman excitation laser on the sample. Using Eq. (60), we could then estimate the Raman signal enhancement of the hybridized Raman peaks $K_{\nu_\pm}$ as:

$$K_{\nu_\pm} = \frac{R_{IN}(\nu_\pm)}{R_{OUT}(\nu_{FR})} \tag{61}$$

Calculations performed on the spectra in Figure 4.8b yield a signal enhancement in the range 100-180 for both the hybridized peaks, confirming our expectations.

Figure 4.9a shows some examples of measurements taken in different positions over the sample surface and provides further information regarding the nanoscale response of the investigated plasmon-phonon strong coupling (in the case of a NC monolayer on L = 5.75 μm antennas), confirming that the hybridization phenomenon only occurs within the nanocavity regions (red curve). As a matter of fact, for acquisitions far from the nanocavities, either along the nanoantennas (black curves), at the extremity of a nanoantenna chain (green curve) or away from the metal over the silicon substrate (blue curve), the Raman spectrum of the NCs results not to be affected by the plasmonic structures. The same behaviour is also well reproduced for nanoantennas with varying length and subsequent degree of coupling, in analogy with what was done for the THz transmission measurements. As it can be seen in Figure 4.9b, the Raman spectrum acquired in the nanocavity region is modified only when *L* is tuned to approximately match the plasmon resonance of the nanoantennas to the Fröhlich phonon mode. Hybridization is mostly evident for L = 5.75 μm nanoantennas (red curve), whose plasmon resonance perfectly matches the phonon mode, while the polariton peaks gradually disappear as we move far away from the resonance matching conditions with the remaining part of the Raman spectrum being unchanged.

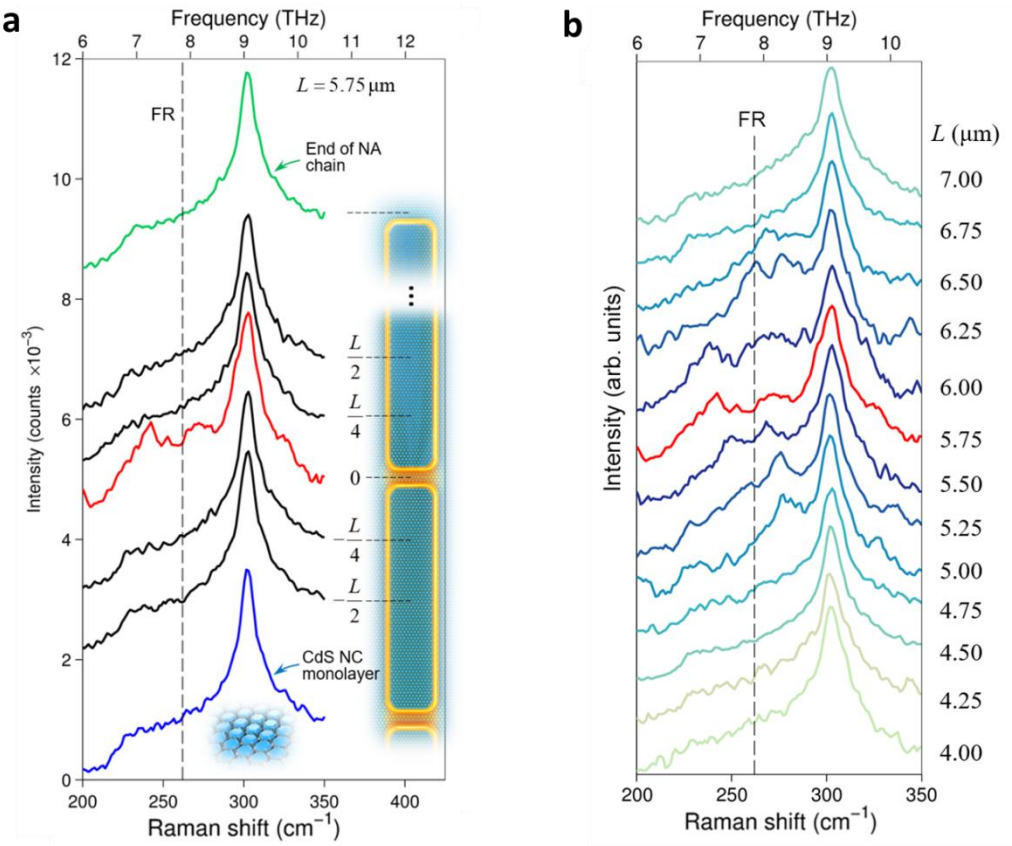


**Figure 4.9: a)** Raman spectra of the NCs taken: in different positions along the nanoantennas composing a nanocavity (black lines), at the end of a nanoantenna chain (green line), in the nanocavity region (red line), and just outside the cavity on the silicon substrate (blue line). The spectra have been vertically shifted for clarity. **b)** Raman spectra of the NCs taken in a nanocavity region for different values of *L*.

Similarly to THz measurements, Raman characterization of increased number of layers confirmed the theoretically predicted power-law dependence on $\sqrt{N}$. Examples of Raman spectra for three values of $N$ are given in Figure 4.10a, which furthermore highlights the significant modification of the Raman response induced by additional NCs, followed by an increase in the measured Rabi splitting.

In order to precisely evaluate the Rabi splitting from the Raman spectra we employed the following procedure. A spectrum of interest (collected in a nanocavity region) was first corrected through linear baseline removal, and then by the subtraction of a reference spectrum (acquired on a spot just outside the cavity region). In this way, the contributions deriving from the transverse optical (TO), longitudinal optical (LO) and uncoupled FR phonon modes, as well as from the gold antenna luminescence background, were removed from the spectral data. On the resulting signals (Figure 4.10b), a deconvolution in the region 200-300 $cm^{-1}$ was operated, by fitting the peaks with two Lorentzian

curves, thus extracting the hybridized resonance positions. For every Raman signal of interest, we then measured the equivalent NC layers $N$ (obtained by direct counting with SEM the NCs in each specific nanocavity) and we were therefore able to associate the observed Rabi splittings with their corresponding $N$ values. The results of these operations are summarized in Figure 4.10c, featuring the dependence of the Rabi splitting on $\sqrt{N}$. Here, the theoretical predictions, i.e. the three-coupled oscillators model and the numerical simulations extracted from the fitted model (2D maps in Figure 4.4 and 4.5), are in very good agreement with both the THz extinction measurements and the Raman points, obtained with the procedure described above. By doing so, we verified the power-law dependence already demonstrated in previous works[9,10], thus providing further evidence of the strong coupling nature of our system.

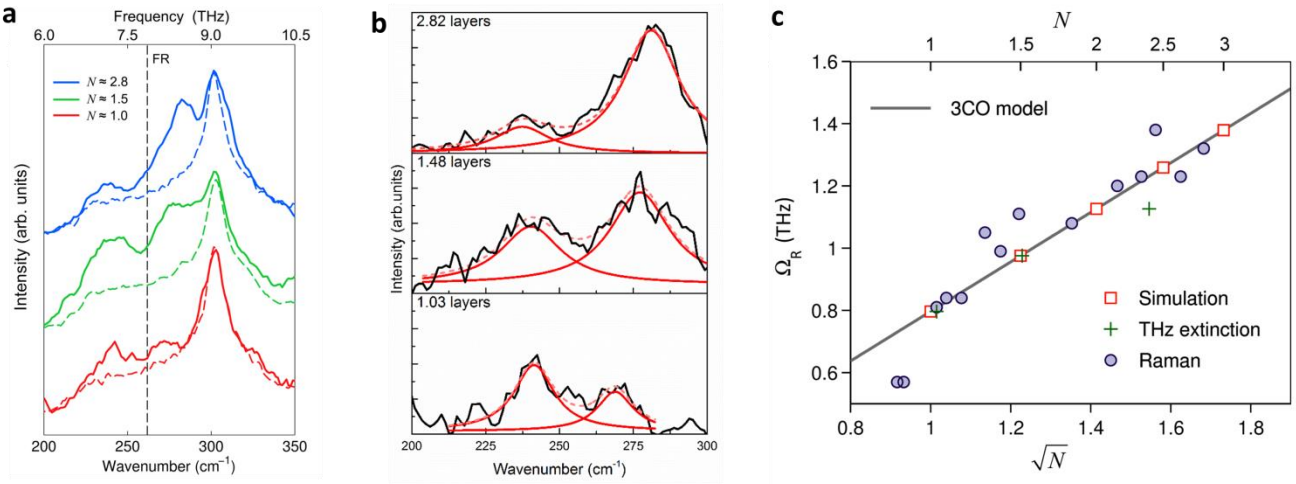


**Figure 4.10: a)** Raman spectra for $L$ = 5.75 μm antennas and three different values of $N$. Solid lines: spectra taken in a nanocavity region; dashed lines: spectra taken just outside the respective cavity (using the same experimental parameters) on the silicon substrate. **b)** Examples of the fitting procedure described above for the Raman spectra reported in (**a**). **c)** Rabi splitting as a function of $\sqrt{N}$, extracted from: the three-coupled-oscillator model (black line), numerical simulations (red bordered squares), THz extinction (green crosses) and Raman measurements (purple circles). For each THz extinction data point, $N$ is evaluated averaging the NC number for several tens of nanocavities. For each Raman data point, instead, $N$ is evaluated considering the number of NCs contained inside the specific nanocavity under measurement.

One limitation of the Raman measurements shown here is represented by the low signal-to-noise ratio. This issue is, however, unavoidable due to both physical and geometrical constraints that are intrinsic properties of the Raman signal. Indeed, the Raman spectral signature of the hybridized Fröhlich

resonance has its origin in an extremely low number of nanocrystals contributing to the hybridization, since the area covered by one nanocavity is 200 time smaller than the focal spot of the exciting laser. Although the noise level is sometimes high, especially in the case of the NC monolayer, the results obtained are remarkable. We have to bear in mind that the Rabi splitting measured in Raman experiments has its origin in the strong coupling of few tens of NCs with the THz vacuum field alone, i.e. no THz photons are injected into the system. Both the NCs and the nanoantennas are non-resonantly coupled to the 633 nm laser employed, so we do not expect any effect like Rabi splitting variations (for changing excitation parameters) or plasmonic enhancement of the signal, differently from conventional Surface Enhanced Raman Scattering experiments[11].

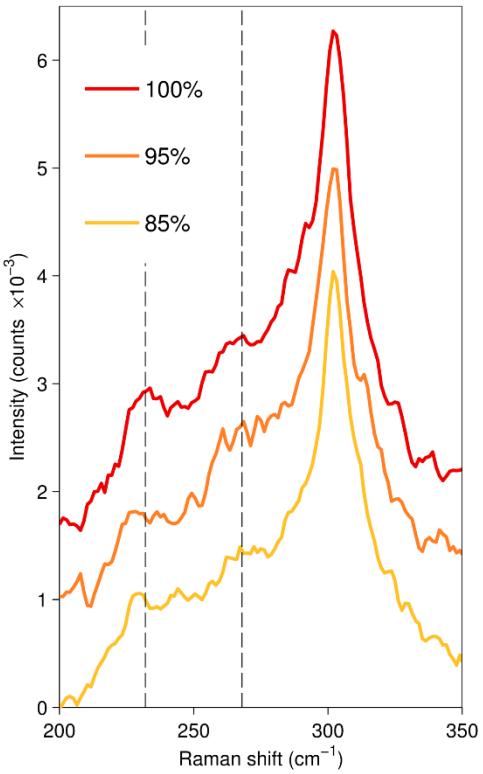


**Figure 4.11:** Raman spectra acquired at different laser power levels on a single nanocavity featuring a number of NC layers $N \sim 1.5$.

In order to corroborate our expectations, we performed additional Raman measurements featuring different laser illumination power on a hybridized plasmonic nanocavity (see Figure 4.11). The maximum laser power was fixed at 1.7 mW (corresponding to 100%) on the sample surface to avoid possible damage to the nanocrystals. Apart from differences in the noise level, the spectral position of

the two hybridized peaks (indicated by vertical dashed lines) did not show any power dependence, and for power levels below 85% they could not be distinguished anymore in the Raman spectra.

Finally, we investigated whether the Raman signal is governed by the scattering of polarized modes of either the plasmonic nanoantennas or the CdS nanocrystals. To this purpose, Raman measurements were acquired to compare spectra where the polarization of the exciting visible laser was set either parallel (red curve in Figure 4.12a) or perpendicular (blue curve in Figure 4.12a) to the long axis of the antennas. In both cases no sign of SERS enhancement, that could be ascribed to particular resonances of the system, was retrieved. Furthermore, no significant differences in the hybridized peak positions and amplitudes were found, confirming that the phonon hybridization observed in Raman measurements does not depend on the polarization properties of the exciting visible laser.

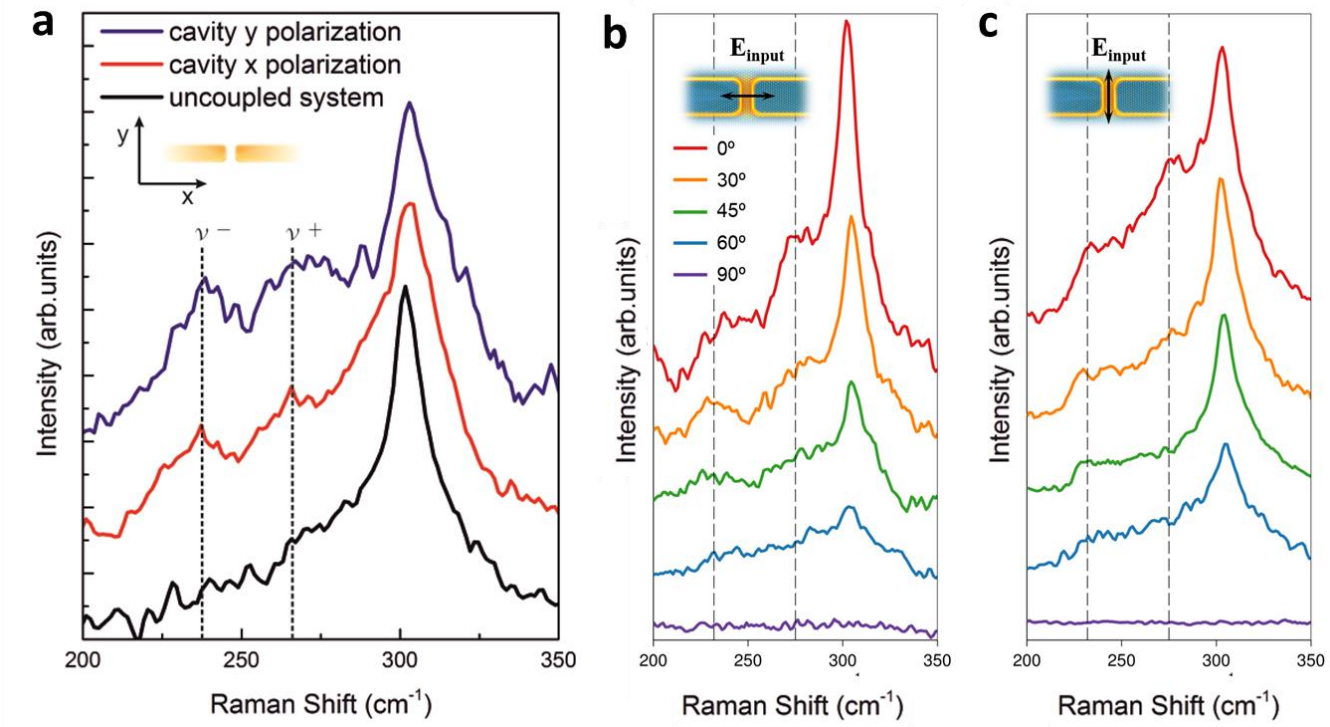


**Figure 4.12: a)** Raman spectra collected in the same nanocavity (covered by a CdS monolayer) with the polarization of the exciting laser source set parallel (red line) and perpendicular (blue line) to the long axis of the antennas. A spectrum collected just outside the gap region (black line) is also shown as reference. **b) - c)**

In addition to these measurements, we also studied the polarization properties of the scattered signal. In order to do this, we positioned an output polarizer (analyzer) in the path of the scattered light collected from the sample, just after the Rayleigh filter (see Figure 4.7 for the setup). We then acquired Raman

spectra of a single hybridized nanocavity keeping fixed the input light polarization (parallel or perpendicular to the long axis of the antennas) and rotating the analyzer in the output path. As can be seen in Figure 4.12b-c, by increasing the angle formed by the main axis of the output analyzer relative to the one of the input polarizer (for the two cases) a progressive reduction of the Raman intensity was observed for both the main LO peak and the hybridized FR peaks, but no variations in peak position and relative amplitudes were noticed. All these peaks eventually disappeared when the main axis of the output analyzer was set perpendicular to the input polarization state. These results thus seem to evidence, at least within our experimental configuration, a similar phonon symmetry between the hybridized Fröhlich response and the LO mode of the NCs, both for the input and the output light polarization.

## References


[1] Nucara, A., Lupi, S.., Calvani, P., "The synchrotron infrared beamline SISSI at ELETTRA," Infrared Phys. Technol. **45**(5), 375–381 (2004).

[2] Lupi, S., Nucara, A., Perucchi, A., Calvani, P., Ortolani, M., Quaroni, L.., Kiskinova, M., "Performance of SISSI, the infrared beamline of the ELETTRA storage ring," J. Opt. Soc. Am. B **24**(4), 959–964, OSA (2007).

[3] Nucara, A., Lupi, S.., Calvani, P., "The infrared synchrotron radiation beamline at the third generation light source ELETTRA," Rev. Sci. Instrum. **74**(9), 3934–3942 (2003).

[4] Törmä, P.., Barnes, W. L., "Strong coupling between surface plasmon polaritons and emitters: a review," Reports Prog. Phys. **78**(1), 13901 (2015).

[5] Lidzey, D. G., Bradley, D. D. C., Armitage, A., Walker, S.., Skolnick, M. S., "Photon-Mediated Hybridization of Frenkel Excitons in Organic Semiconductor Microcavities," Science (80-. ). **288**(5471), 1620 LP-1623 (2000).

[6] Shalabney, A., George, J., Hiura, H., Hutchison, J. A., Genet, C., Hellwig, P.., Ebbesen, T. W., "Enhanced Raman Scattering from Vibro-Polariton Hybrid States," Angew. Chemie Int. Ed. **54**(27), 7971–7975 (2015).

[7] del Pino, J., Feist, J.., Garcia-Vidal, F. J., "Signatures of Vibrational Strong Coupling in Raman Scattering," J. Phys. Chem. C **119**(52), 29132–29137, American Chemical Society (2015).

[8] Nagasawa, F., Takase, M.., Murakoshi, K., "Raman Enhancement via Polariton States Produced

by Strong Coupling between a Localized Surface Plasmon and Dye Excitons at Metal Nanogaps," J. Phys. Chem. Lett. **5**(1), 14–19, American Chemical Society (2014).

[9] Chikkaraddy, R., de Nijs, B., Benz, F., Barrow, S. J., Scherman, O. A., Rosta, E., Demetriadou, A., Fox, P., Hess, O., et al., "Single-molecule strong coupling at room temperature in plasmonic nanocavities," Nature **535**, 127, Nature Publishing Group, a division of Macmillan Publishers Limited. All Rights Reserved. (2016).

[10] Wang, H., Toma, A., Wang, H.-Y., Bozzola, A., Miele, E., Haddadpour, A., Veronis, G., De Angelis, F., Wang, L., et al., "The role of Rabi splitting tuning in the dynamics of strongly coupled J-aggregates and surface plasmon polaritons in nanohole arrays," Nanoscale **8**(27), 13445–13453, The Royal Society of Chemistry (2016).

[11] Chirumamilla, M., Toma, A., Gopalakrishnan, A., Das, G., Zaccaria, R. P., Krahne, R., Rondanina, E., Leoncini, M., Liberale, C., et al., "3D Nanostar Dimers with a Sub-10-nm Gap for Single-/Few-Molecule Surface-Enhanced Raman Scattering," Adv. Mater. **26**(15), 2353–2358 (2014).

# Chapter 5

## THz nanoslits: towards the ultra-strong coupling regime

When the coupling strength of the interaction becomes comparable to the frequency of the involved oscillators, the system enters a new quantum electrodynamics regime, the so-called ultra-strong coupling regime. The perturbation of the coupled system is so strong that even the energies of the other states of the system are considerably modified. This is the case of the ground state energy of the system, which has been predicted to shift[1,2] and has also been observed experimentally[3,4]. Moreover, the system is no longer in the Markovian regime since $\hbar\Omega_{VR} \gg k_B T$ and, as a consequence, the lifetimes of the hybrid polaritonic states cannot be predicted from the lifetimes of the uncoupled constituents, i.e. in our specific case the lifetime of the plasmon and the excited state of the CdS nanocrystals.

From a theoretical point of view, in this regime the rotating wave approximation, that we have exploited in Chapter 1 to retrieve the eigenenergies and eigenstates of the coupled system, is not valid anymore and one should consider additional terms in the overall Hamiltonian. Baumann et al.[5] employed a Dicke Hamiltonian to describe the quantum phase transition in a system formed by a Bose-Einstein condensate ultra-strongly coupled to an optical cavity mode. However, many aspects of the physics behind still remain unexplored and further studies are needed to unveil the quantum nature of these phenomena.

In parallel, several experimental studies have observed Rabi splittings reaching a significant fraction of the involved transition energies in the case of molecules coupled to a cavity light field[6,7], measuring coupling strength corresponding to 73% of the matter excitation energy, the highest ever reported for a light-matter coupled system at room temperature. A recent work[8], involving the coupling of SPPs and molecular excitons, observed normal mode splittings approaching the magnitude of the field frequency; similar results were obtained in the THz spectral range by Todorov et al.[9] using electromagnetic resonators coupled to an electronic transition of a semiconductor quantum well.

The high Rabi splitting values obtained in these works were achieved following two different routes: either using a molecular transition with high absorption cross-section or transition dipole moment ($\mu$), which efficiently couples to the electromagnetic field, or by employing cavities with very small mode volumes ($V$), which feature high electromagnetic field enhancement and squeezing. As a matter of fact,

in the absence of dissipation, the Rabi splitting energy between the two new hybrid light-matter states is given by:

$$\hbar\Omega_R = 2E_{vac}\,\mu\sqrt{n_{ph}+1} = 2\mu\sqrt{\frac{\hbar\omega}{2\varepsilon_0 V}}\sqrt{n_{ph}+1} \tag{62}$$

As already anticipated in Chapter 1, even in the absence of photons, there remains a finite value for the Rabi splitting, i.e. the vacuum Rabi splitting $\hbar\Omega_{VR}$, due to interaction with the vacuum field. This energy splitting is indeed proportional to the square root of the molecular concentration in the cavity.

In further developments of the work presented in Chapter 4, we exploited all these advantages to obtain Rabi splitting energies exceeding 24% of the investigated matter resonance. Vibrational ultra-strong coupling was achieved between the plasmon mode of THz plasmonic nanoslits and the Fröhlich phonon mode of the synthesized nanocrystals. The THz characterization of the coupled system optical response confirmed our expectations and future Raman measurements will provide a clearer picture of the quantum nature of such hybrid nanosystems.

## 5.1 THz plasmonic nanoslits – NCs system

In order to investigate plasmon-phonon ultra-strong coupling in the THz regime, we fabricated arrays of isolated plasmonic nanoslits (covering an area of 200 x 200 $\mu m^2$), which differently from their antenna counterpart are not coupled *via* narrow gaps to their neighbours. A similar design was recently employed by Keller et al.[10] to obtain ultra-strong coupling between hybrid dipole antenna split-ring resonator cavities and less than 100 electrons of a 2D gas.

As for the nanoantennas, the fabrication procedure was carried out in a Cleanroom environment. A 500 μm thick, high resistivity (> 10 kΩcm) (100)-oriented silicon chip was employed as sample substrate. After cleaning in an ultrasonic bath of acetone and isopropyl alcohol, electron beam evaporation in a high vacuum chamber (base pressure $10^{-7}$ mbar) was exploited to produce a 5-nm adhesion layer of chromium and a 55-nm Au film, with a 0.3 Å/s deposition rate. A 160-nm thick poly(methyl methacrylate) (PMMA) layer was spin-coated at 1800 rpm on top of the metal layer, followed by a 7 minutes annealing at 180 °C. Electrical contact between the sample holder and the sample top surface

is provided in this case by the Au metal film, so there is no need to evaporate a conductive layer on top of the PMMA. Electron beam direct-writing of the nanoantenna arrays was carried out using an ultra-high resolution Raith 150-Two e-beam lithography and imaging system, setting the beam energy to 20 keV and the exposure dose to 500 μC/cm$^2$. After e-beam lithography, the exposed resist was developed in a solution of methyl isobutyl ketone (MIBK)/isopropanol (IPA) (1:3) for 30 s at 4 °C, followed by Au and Cr wet etch for 5 and 10 seconds respectively. This fabrication step allows to transfer the lithographic pattern into the underlying metal layer (see Figure 5.1). Drop casting of 20 μL solution (at 10 μM concentration) on the fabricated nanoslits was used to deposit our NCs (either CdS or lead sulfide (PbS) for this design) in the patterned areas. Finally, the unexposed resist and NCs deposited over the PMMA surface were removed through a conventional lift-off process in hot acetone. The final result of this fabrication procedure is schematically depicted in Figure 5.1, showing a single nanoslit completely filled with NCs.

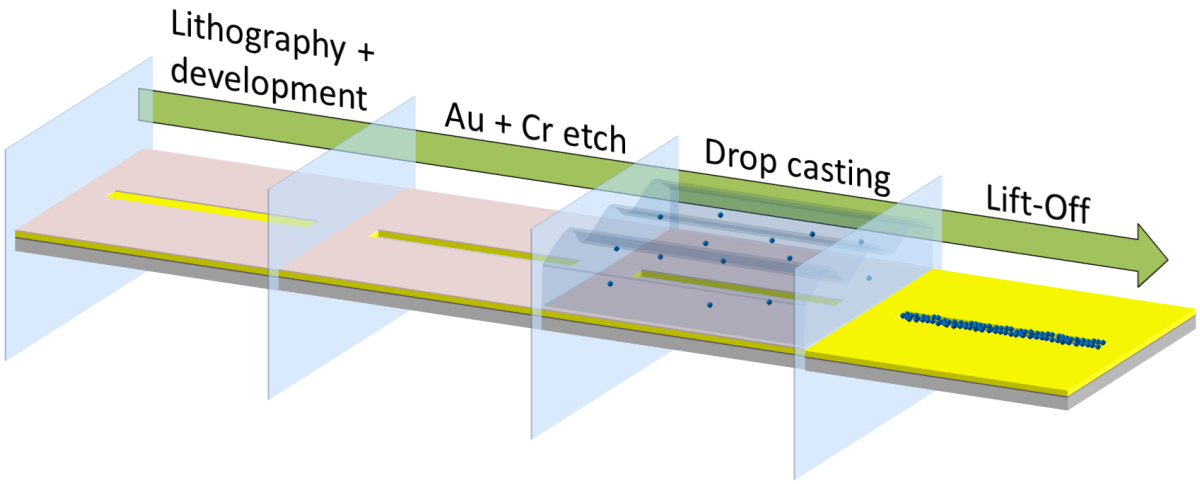


**Figure 5.1:** Schematic of the nanoslit + NCs fabrication protocol.

The fabricated two-dimensional arrays cover an area of 200 x 200 μm$^2$ and are composed of isolated nanoslits (about 700 elements) with 5 μm separation in both their long and short axis directions, $G_x = G_y = 5$ μm. The nanoslits are h = 55-nm deep, i.e. overall thickness of Cr and Au metal layers, and w = 250-nm wide. In the case of CdS NCs, array with different nanoslit length $L$, ranging from 5.5 to 9.5 μm, were fabricated on the same silicon substrate in order to tune their plasmonic resonance in the THz frequency band around the Fröhlich phonon mode of the nanocrystals (7.85 THz). In the case

of PbS NCs instead, nanoslits with length *L* in the range 9 to 12 μm were fabricated, tuning their resonance around the optical phonon frequency of the PbS nanocrystals located at about 6 THz.

A Helios NanoLab 600i scanning electron microscope (SEM) has been used to acquire in tilted view the images reported in Figure 5.2 of L = 8μm nanoslits filled with CdS NCs (Figure 5.2a) and the detail of a single nanoslit (Figure 5.2b). Similar results were obtained with PbS nanocrystals. As it can be seen in the SEM images, the external profile of the nanoslit is irregular along the nanoslit surface. This is an issue of the fabrication protocol, which employs two wet etching steps (Au and Cr etch) that are intrinsically endowed with poor control over etching rate and uniformity over the sample surface. Alternative, but not straightforward, fabrication methods could be therefore applied in future developments of the present work.

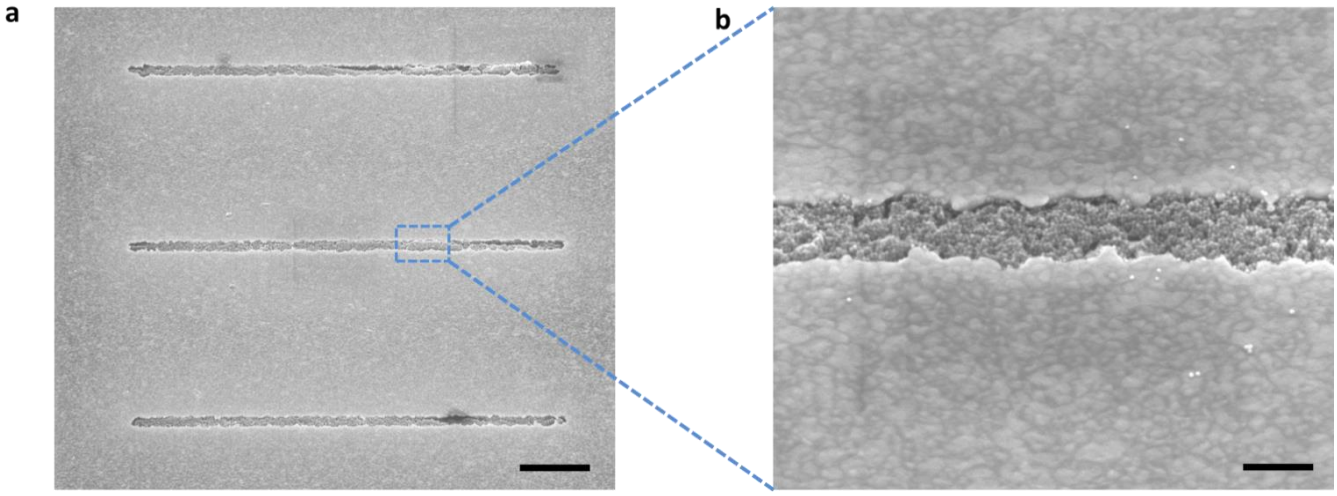


**Figure 5.2: a)** SEM tilted view of L = 8 μm nanoslits filled with CdS NCs; scale bar 2 μm**. b)** Detail of a nanoslit + CdS system; scale bar 250 nm.

In order to estimate the best nanoslit configuration that matches the phonon resonance of the NCs, we have performed electromagnetic simulations using a commercial Finite Element Method-based software: COMSOL Multiphysics, Optics Module, which was also used for the THz nanoantennas. We considered nanoantenna with geometrical parameters corresponding to the fabricated values (see above) and the nanoantenna length was varied in the same range to tune the array resonance peak position. The structure parameters and illumination geometry was kept identical to the one used in Chapter 3, which well reproduces the transmission response of the experimentally measured arrays. Also in this case, the results of the simulations were normalized to the area of the illuminating THz

spot in the experimental measurements (diameter D ≈ 260 μm), which is bigger than the array dimensions (200 x 200 $\mu m^2$). Figure 5.3 shows the relative transmittance of the nanoslit arrays with different slit length as a function of frequency. The array response calculated here demonstrate how the array resonance can be easily tuned across a wide frequency range around the CdS phonon resonance at 7.85 THz (Figure 5.3a) and the PbS phonon resonance at about 6 THz (Figure 5.3b). The best tuned geometries are $L$ = 7.5 μm and $L$ = 9.5 μm nanoslits in the case of CdS and PbS, respectively. The calculated transmittance spectra are normalized to the transmission of a bare Si substrate.

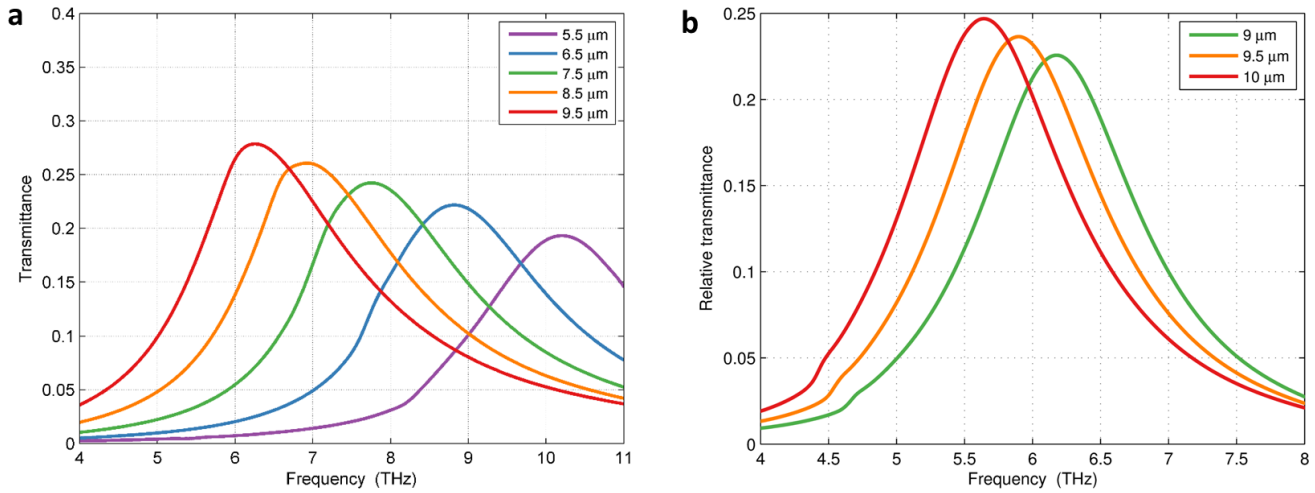


**Figure 5.3: a) - b)** Relative transmittance of nanoslit arrays with varying length $L$ optimized to match the optical phonon resonance of CdS (**a**) and PbS (**b**) nanocrystals.

## 5.2 THz characterization

THz transmission measurements were performed on both kinds of nanoslit + NCs systems orienting the samples in such a way that the long axis of the slits was set parallel to the main polarization axis. Preliminary measurements were done on a PbS film (20 μL drop-casted on a bare silicon substrate) in order to characterize its spectral response. The optical Fröhlich resonance of the PbS NCs was located at 5.8 THz (see Figure 5.4a), thus lying in the spectral range spanned by the plasmon resonance of the fabricated arrays. The transmission of the PbS film was then normalized to a reference spectrum acquired on a bare Si substrate. Comparison with the optical response of CdS NCs (Figure 4.3, Chapter 4), highlights how the PbS NCs feature both a lower absorbance and a higher linewidth than their CdS counterpart, making these NCs not as a good candidate for strong hybridization with the electromagnetic vacuum field in the nanocavities. This is better exemplified by the coupled system

transmittance (see Figure 5.4b), normalized to the one of a bare Si substrate. No clear signature of the appearance of two hybrid polariton bands is in fact clearly visible, differently from the nanoantenna geometry, apart from a small kink in the spectra at about 6.1 THz. This would suggest that the spectral response of the NCs is only slightly perturbed by the presence of the plasmonic nanoslits, therefore hinting for the establishment of a weak coupling regime between the light part and the matter constituents.

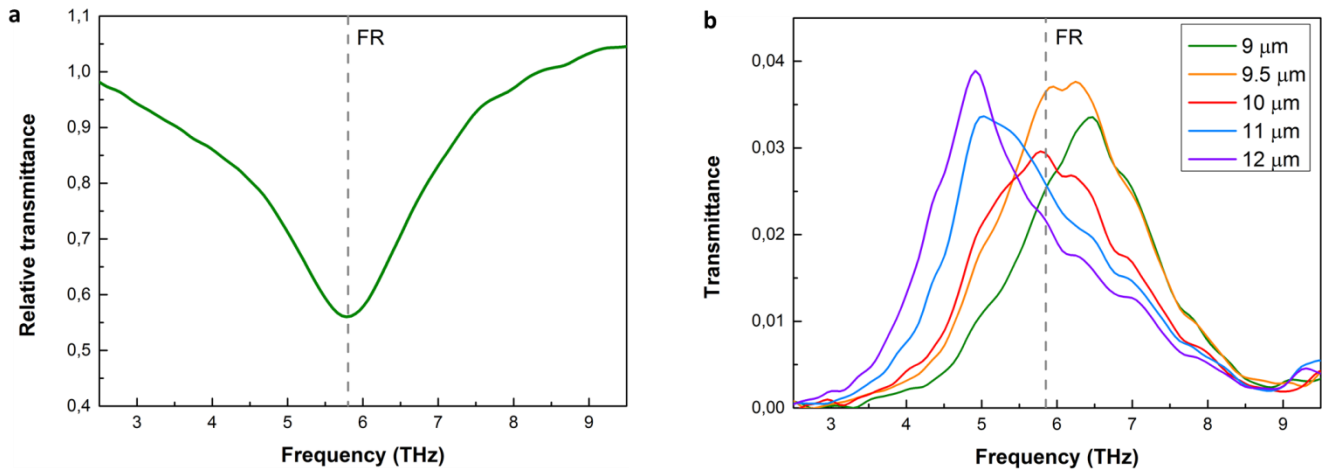


**Figure 5.4: a)** THz transmittance of PbS NCs deposited on a Si substrate. The NC optical response is normalized with respect to the transmission of a bare Si substrate. The vertical dashed line marks the position of the NC Fröhlich resonance. **b)** Transmission response of nanoslit arrays filled with PbS NCs for different slit length *L*. The vertical dashed line marks the position of the NCs phonon.

A different behaviour, instead, was observed with nanoslits filled with CdS NCs. The transmittance of the coupled system depicts two distinct polariton bands at each side of the unperturbed phonon resonance of the CdS NCs (see Figure 5.5a).

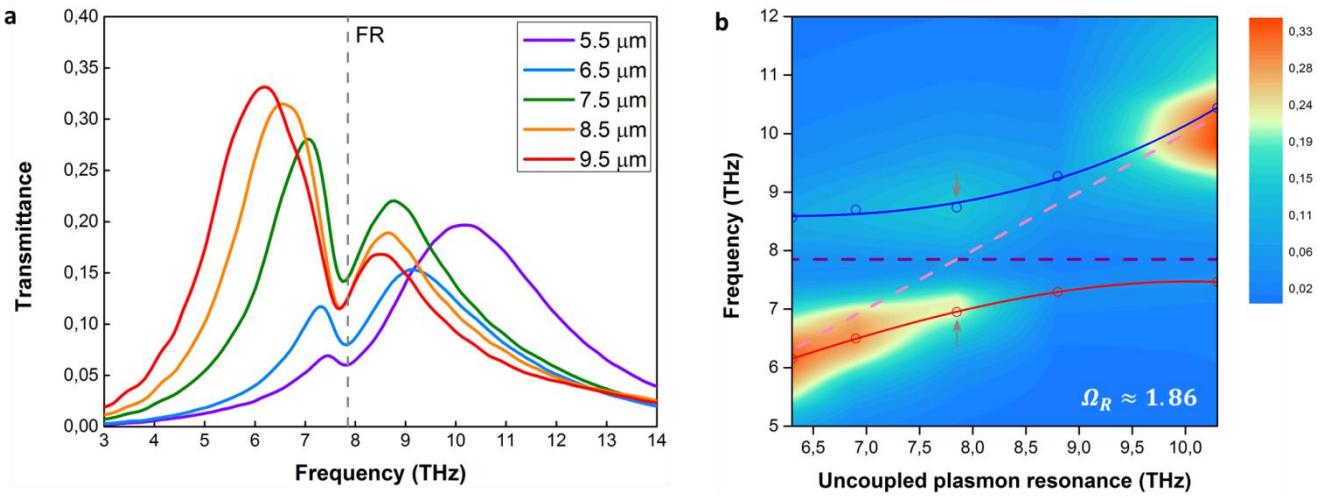


**Figure 5.5: a)** Transmission response of nanoslit arrays filled with PbS NCs for different slit length *L*. The vertical dashed line marks the position of the NCs phonon. **b)** Experimental 2D map of the polariton branches dispersion. The color bar corresponds to the extinction of the arrays. The blue (red) solid lines are the fitted trends of the high-energy (low-energy) polariton branch, while the corresponding open circles represent the measured values.

The spectral position of the hybrid peaks in the transmission spectra allowed us to reconstruct the dispersion of the polariton bands (see Figure 5.5b), which shows the characteristic anti-crossing behaviour of strongly coupled oscillators, with the anti-crossing region located around the optical phonon resonance. As for the nanoantenna case, far from the Fröhlich resonance the two systems behave as uncoupled oscillators, following the spectral response of either the bare antennas (pink diagonal dashed line) or the unperturbed Fröhlich mode of the NCs (purple horizontal dashed line at 7.85 THz). As we approach the resonance matching conditions, the two curves split giving rise to two separated hybrid bands. The Rabi splitting $\Omega_R$, evaluated at the crossing point between the uncoupled plasmon resonance and the phonon mode of the NCs, reached a value of 1.86 THz, which corresponds to 24% of the matter resonance. The perturbation introduced in the coupled system thus represents a significant amount of the constituent transition energies, hinting for the establishment of an ultra-strong coupling regime.

Even though the nanoslit geometry is endowed with a lower field enhancement and bigger mode volumes than its nanoantenna counterpart, we achieved higher Rabi splittings by increasing the concentration of hybridized nano-objects in our plasmonic nanocavities. In future developments, optimization of the plasmonic element is therefore highly demanded for the realization of nanoscale devices with engineered optical properties in the THz spectral range.

Research in the field of strong light-matter interactions is still at an embryonic stage, despite all the fascinating results obtained so far. The fundamental mechanisms are not completely understood and much more has to be done to clarify the basic principles and deepen our comprehension of the quantum nature of such phenomena. Within this context, we think that our contribution would be of primary importance, thanks to the collaboration with partners who are leading personalities in the burgeoning field of quantum optics (Prof. Luca Razzari and Prof. Roberto Morandotti at INRS-EMT, Canada). With our work, we propose an alternative approach to obtain ultra-strong coupling interactions by means of plasmonic nanocavities hybridized with a very small number of emitters. Results are encouraging and we believe that represent a launch pad for the realization of ultralow-power emitting sources at THz frequencies.

## References


[1] Ciuti, C., Bastard, G.., Carusotto, I., "Quantum vacuum properties of the intersubband cavity polariton field," Phys. Rev. B **72**(11), 115303, American Physical Society (2005).

[2] Casanova, J., Romero, G., Lizuain, I., Garcia-Ripoll, J. J.., Solano, E., "Deep Strong Coupling Regime of the Jaynes-Cummings Model," Phys. Rev. Lett. **105**(26), 263603, American Physical Society (2010).

[3] Forn-Díaz, P., Lisenfeld, J., Marcos, D., García-Ripoll, J. J., Solano, E., Harmans, C. J. P. M.., Mooij, J. E., "Observation of the Bloch-Siegert Shift in a Qubit-Oscillator System in the Ultrastrong Coupling Regime," Phys. Rev. Lett. **105**(23), 237001, American Physical Society (2010).

[4] Canaguier-Durand, A., Devaux, E., George, J., Pang, Y., Hutchison, J. A., Schwartz, T., Genet, C., Wilhelms, N., Lehn, J.-M., et al., "Thermodynamics of Molecules Strongly Coupled to the Vacuum Field," Angew. Chemie **125**(40), 10727–10730 (2013).

[5] Baumann, K., Guerlin, C., Brennecke, F.., Esslinger, T., "Dicke quantum phase transition with a superfluid gas in an optical cavity," Nature **464**, 1301, Macmillan Publishers Limited. All rights reserved (2010).

[6] George, J., Wang, S., Chervy, T., Canaguier-Durand, A., Schaeffer, G., Lehn, J.-M., Hutchison, J. A., Genet, C.., Ebbesen, T. W., "Ultra-strong coupling of molecular materials: spectroscopy and dynamics," Faraday Discuss. **178**(0), 281–294, The Royal Society of Chemistry (2015).

[7] Askenazi, B., Vasanelli, A., Delteil, A., Todorov, Y., Andreani, L. C., Beaudoin, G., Sagnes, I.., Sirtori, C., "Ultra-strong light–matter coupling for designer Reststrahlen band," New J. Phys. **16**(4), 43029 (2014).

[8] Schwartz, T., Hutchison, J. A., Léonard, J., Genet, C., Haacke, S.., Ebbesen, T. W., "Polariton Dynamics under Strong Light–Molecule Coupling," ChemPhysChem **14**(1), 125–131, WILEY-VCH Verlag (2013).

[9] Todorov, Y., Andrews, A. M., Colombelli, R., De Liberato, S., Ciuti, C., Klang, P., Strasser, G.., Sirtori, C., "Ultrastrong Light-Matter Coupling Regime with Polariton Dots," Phys. Rev. Lett. **105**(19), 196402, American Physical Society (2010).

[10] Keller, J., Scalari, G., Cibella, S., Maissen, C., Appugliese, F., Giovine, E., Leoni, R., Beck, M.., Faist, J., "Few-Electron Ultrastrong Light-Matter Coupling at 300 GHz with Nanogap Hybrid LC Microcavities," Nano Lett. **17**(12), 7410–7415 (2017).

# Conclusion and outlook

In conclusion, we have shown that the dipole-active phonon resonance of semiconductor polar NCs can be hybridized by the strongly concentrated and enhanced THz vacuum field of a plasmonic nanoantenna cavity, whose resonance can be easily tuned to match the Fröhlich mode of the NCs. Evidence of strong plasmon-phonon coupling can be observed in the far field, by direct THz illumination of an extended array of nanoantennas covered with the NCs. Reconstruction of the hybrid polariton bands features the characteristic anti-crossing behaviour of strongly coupled systems, confirming the numerical simulations performed with a three-coupled oscillator model. Rabi splittings of almost 1 THz, evaluated at the spectral position where the uncoupled plasmon resonance is aligned to the uncoupled phonon mode, have been experimentally measured with only a NC monolayer (80-90 nanocrystals per cavity) deposited on the nanoantennas. Moreover, the predicted power law dependence of the Rabi splitting energy on the square root of the NC concentration has been both numerically and experimentally demonstrated.

A micro-Raman characterization of the surface in "dark" conditions (i.e. with no THz illumination) shows that the hybridization occurs just in the nanocavity regions, confirming the nanoscale nature of the phonon resonance reshaping. Vacuum Rabi splittings exceeding 15% of the uncoupled phonon resonance frequency are found in Raman spectra of cavities containing less than 3 NC layers (about 200 emitters), and are accompanied by a Raman signal enhancement > 100, confirming previous studies.

Further studies employing a nanoslit geometry as plasmonic element have evidenced how the plasmon-phonon interaction can be pushed forward towards the ultra-strong coupling regime. Despite the lower field enhancement and squeezing, THz nanoslits provide a viable tool to greatly increase the concentration of hybridized nanocrystals. THz transmission measurements have shown clear hybridization of the system constituents, with Rabi splittings reaching a significant fraction (25%) of the uncoupled matter resonance. However, many aspects of the physics behind this coupling regime still remain unexplored, both theoretically and experimentally, and further investigation is needed to unveil the quantum nature of such systems. We believe that a comprehensive micro-Raman characterization of the nanoslit-NC design will help further corroborate our findings and pave the way towards future applications in optoelectronic devices. On the one hand, our findings open novel venues for engineering the optical phonon response of nanomaterials, which can have a significant impact for

example in their light-emitting properties or in their electronic transport characteristics, due to the crucial role played by electron-phonon interactions in such systems. On the other hand, nanoscale plasmon-phonon strong coupling can represent an innovative platform for THz science, for the exploration of enhanced and localized nonlinear phenomena as well as for the generation of coherent radiation in this still hardly accessible region of the electromagnetic spectrum. Within this context, the proposed architectures are currently investigated in collaboration with the ultra-fast photonics and THz spectroscopy group at INRS-EMT, Canada (Prof. Luca Razzari and Prof. Roberto Morandotti) and exploiting the amazing facility of ELETTRA, a center of excellence in the field of synchrotron science. Attractive perspectives are expected towards the practical implementation of innovative quantum information systems and/or ultralow-power emitting sources approaching the so-called "thresholdless regime", paving the way for the realization of new generation THz sources.

# Appendix A

## Three-coupled oscillator model

As shown in Chapter 4, due to the presence of the lattice mode at around 9.8 THz, our overall system in THz transmission measurements is better described by a three-coupled oscillator model[1,2]. The following matrix equation can be used to retrieve the characteristic frequency dispersion of the investigated interaction:

$$\begin{pmatrix} \nu_{pl} - \nu & V_{pl-ph} & V_{pl-lat} \\ V_{pl-ph} & \nu_{ph} - \nu & 0 \\ V_{pl-lat} & 0 & \nu_{lat} - \nu \end{pmatrix} \begin{pmatrix} \alpha \\ \beta \\ \gamma \end{pmatrix} = 0 \tag{63}$$

where $\nu_{pl}$, $\nu_{ph}$ and $\nu_{lat}$ are the frequencies of the non-interacting plasmon, phonon and lattice modes, respectively, while ν are the eigenfrequencies of the coupled system. $V_{pl-ph}$ ($V_{pl-lat}$) is the coupling constant between the plasmon and the phonon (lattice) modes. Finally, α, β and γ represents the coefficients of the basis functions of the bare plasmon, phonon and lattice modes, respectively. Diagonalizing this matrix, the dispersion of the hybrid eigenfrequencies can be readily evaluated.

In order to compare the above model to our numerical and experimental results, the uncoupled plasmon resonance frequency needs to be estimated. The resonance wavelength $\lambda_{Res}$ of nanorod-shaped plasmonic nanoantennas typically obeys the following equation[3,4]:

$$\lambda_{Res} \approx 2 n_{eff} L \tag{64}$$

where $n_{eff}$ is the effective refractive index of the nanorod surface mode. While this equation well describes the behaviour of isolated nanoantennas in the THz spectral range, an additional parameter *S* has to be added in the case of an array of interacting antennas:

$$\lambda_{Res} = 2 n_{eff} L + S \tag{65}$$

to also take into account the expected red-shift of the resonance induced by the near-field coupling between the nanostructures[5]. In particular, by fitting the resonance wavelength dependence on the nanoantenna length for the case of bare nanoantenna arrays with the above equation (65) (far from the lattice mode), we then obtain the values $n_{eff}^{0} = 2.375$ and $S = 10.2$ μm (see red circles and related fit in Figure A.1). The uncoupled plasmon resonance frequency in our system can be thus written as:

$$\nu_{pl} = \frac{c}{2n_{eff}L + S} \tag{66}$$

with *c* being the speed of light in vacuum.

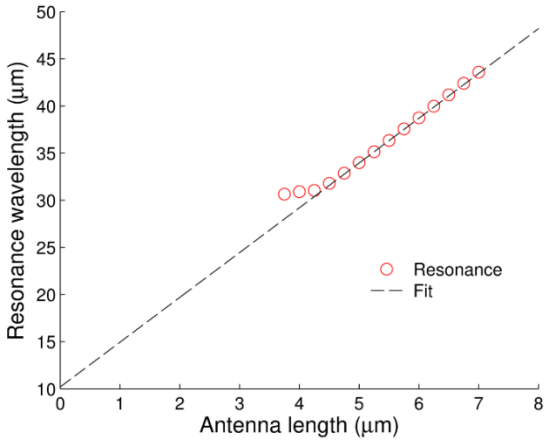


**Figure A.1:** Resonance wavelength as a function of the antenna length for bare arrays.

The above relation (66) has been used to fit the numerical and experimental polariton dispersion curves with the model expressed in Eq. (63). Figure A.2 shows the results of this numerical procedure for the case of a NC monolayer on the nanoantenna arrays.

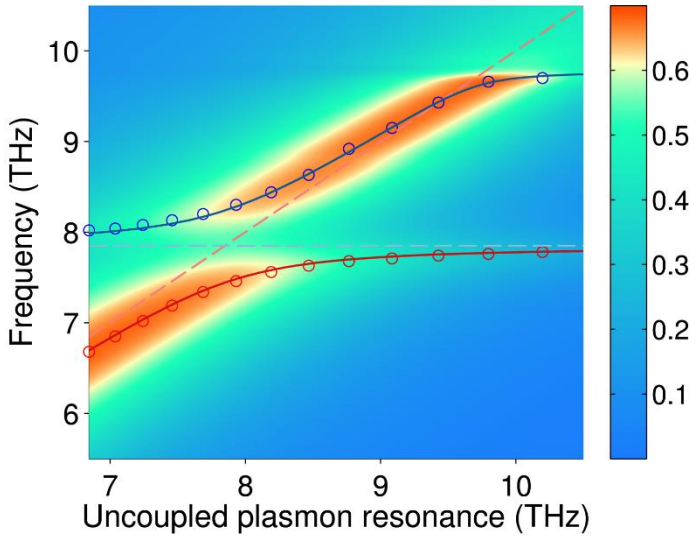


**Figure A.2:** Polariton dispersion fit of the simulation results for a NC monolayer.

From these fits we can also extract the quantities $|\alpha^2|$, $|\beta^2|$ and $|\gamma^2|$, which can be used to estimate the relative contribution of the plasmon, phonon and lattice modes to the overall hybridized state. As can be seen from Figure A.3 below, at the Fröhlich resonance frequency an essentially complete hybridization of the plasmon-phonon modes occurs ($|\alpha^2|$, $|\beta^2| \approx 0.5$), while the contribution of the lattice mode is negligible.

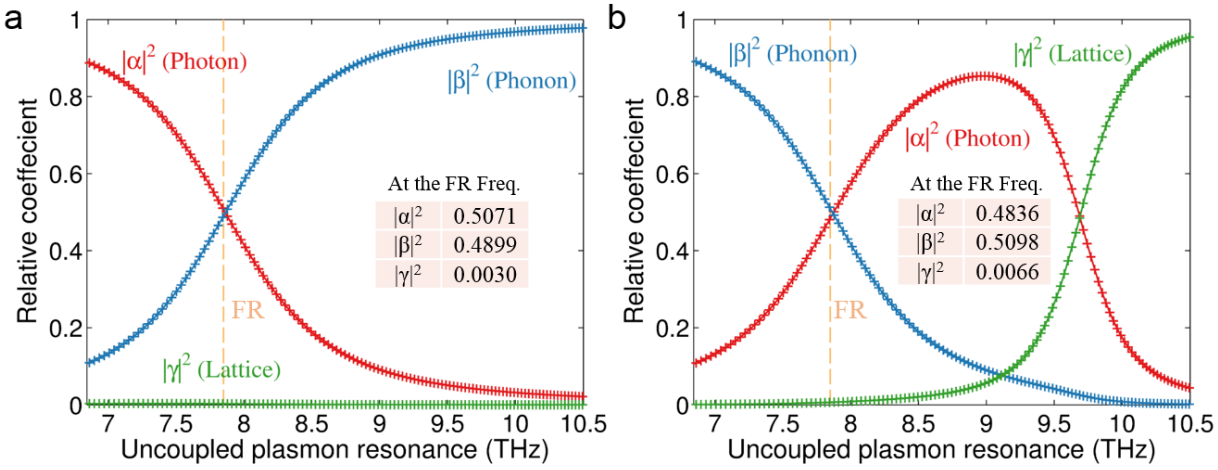


**Figure A.3: a)** Relative coefficients for the low-energy polariton branch, in the case of a NC monolayer. **b)** Same as in (**a**), for the high-energy polariton branch.

Table 1 (simulations) and Table 2 (experiments) below summarize all the parameters used in the fitting procedure and also include the root-mean-square error (RMSE) analysis for the two polariton branches:

$RMSE = \sqrt{\frac{1}{m}\sum_{j=1}^{m}(y_j - \hat{y}_j)}$ where $y_j$ are the analytical model estimates for the polariton branch positions and $\hat{y}_j$ the $m$ experimental or simulation points. In both simulations and experiments, and for the different number of NC layers, the following parameters were kept constant in the fitting procedure: $\nu_{ph} = 7.85$ THz, $\nu_{lat} = 9.78$ THz, $S = 10.2$ µm, $V_{pl-lat} = 0.18$ THz. The plasmon-phonon coupling constant was considered to obey the relation[6]:

$$V_{pl-ph} = V_{pl-ph}^{1}\sqrt{N} \tag{67}$$

where $V_{pl-ph}^{1}$ is the value of this coupling parameter for a NC monolayer and $N$ is the number of layers considered. Interestingly, we found that for the best fit of both the experimental and numerical data, the effective refractive index needs to be slightly incremented with increasing NC layers, according to the empirical rule: $n_{eff} = \gamma_{eff}N + n_{eff}^{0}$, with $\gamma_{eff} = 0.025$. This behaviour is consistent with the increase in the average permittivity around the nanoantennas induced by the presence of the NC layers. For both the experimental and simulation polariton traces, the *RMSE* values associated with the fitting curves are of the order of some tens of GHz, well below the Rabi splitting values (≥ 800 GHz) extracted from our THz response data in the case of 1 NC layer.

| | 1 layer | 1.5 layers | 2 layers | 2.5 layers | 3 layers | Units |
|---|---|---|---|---|---|---|
| $V_{pl\text{-}ph}$ | 0.40 | 0.49 | 0.57 | 0.63 | 0.69 | THz |
| $V_{pl\text{-}lat}$ | 0.18 | 0.18 | 0.18 | 0.18 | 0.18 | THz |
| $\nu_{ph}$ | 7.85 | 7.85 | 7.85 | 7.85 | 7.85 | THz |
| $\nu_{lat}$ | 9.78 | 9.78 | 9.78 | 9.78 | 9.78 | THz |
| $n_{eff}$ | 2.400 | 2.413 | 2.425 | 2.438 | 2.450 | / |
| $S$ | 10.2 | 10.2 | 10.2 | 10.2 | 10.2 | µm |
| *RMSE* ($\nu_+$) | 0.025 | 0.025 | 0.019 | 0.020 | 0.024 | THz |
| *RMSE* ($\nu_-$) | 0.016 | 0.009 | 0.004 | 0.009 | 0.018 | THz |

**Table 1:** Fitted coefficients for the simulated polariton traces.

| | 1 layer | ~1.5 layers | ~2 layers | Units |
|---|---|---|---|---|
| $V_{pl\text{-}ph}$ | 0.40 | 0.49 | 0.57 | THz |
| $V_{pl\text{-}lat}$ | 0.18 | 0.18 | 0.18 | THz |
| $\nu_{ph}$ | 7.85 | 7.85 | 7.85 | THz |
| $\nu_{lat}$ | 9.78 | 9.78 | 9.78 | THz |
| $n_{eff}$ | 2.400 | 2.413 | 2.425 | / |

| | | | | |
|---|---|---|---|---|
| $S$ | 10.2 | 10.2 | 10.2 | μm |
| $RMSE\ (\nu_+)$ | 0.085 | 0.035 | 0.053 | THz |
| $RMSE\ (\nu_-)$ | 0.065 | 0.049 | 0.069 | THz |

**Table 2:** Fitted coefficients for the experimental polariton traces.

## References


[1] Lidzey, D. G., Bradley, D. D. C., Armitage, A., Walker, S.., Skolnick, M. S., "Photon-Mediated Hybridization of Frenkel Excitons in Organic Semiconductor Microcavities," Science (80-. ). **288**(5471), 1620 LP-1623 (2000).

[2] Armitage, A., Skolnick, M. S., Kavokin, A. V., Whittaker, D. M., Astratov, V. N., Gehring, G. A.., Roberts, J. S., "Polariton-induced optical asymmetry in semiconductor microcavities," Phys. Rev. B **58**(23), 15367–15370, American Physical Society (1998).

[3] Cubukcu, E.., Capasso, F., "Optical nanorod antennas as dispersive one-dimensional Fabry–Pérot resonators for surface plasmons," Appl. Phys. Lett. **95**(20), 201101, American Institute of Physics (2009).

[4] Razzari, L., Toma, A., Clerici, M., Shalaby, M., Das, G., Liberale, C., Chirumamilla, M., Zaccaria, R. P., De Angelis, F., et al., "Terahertz Dipole Nanoantenna Arrays: Resonance Characteristics," Plasmonics **8**(1), 133–138 (2013).

[5] Fischer, H.., Martin, O. J. F., "Engineering the optical response of plasmonic nanoantennas," Opt. Express **16**(12), 9144–9154, OSA (2008).

[6] Yamamoto, Y., Tassone, T.., Cao, H., Semiconductor Cavity Quantum Electrodynamics, Springer T, Springer US (2000).

# Acknowledgments

As a “scientist” or whatever I like to call myself today, this is the toughest part of the PhD thesis to be produced. I could just skip it, however it would be pretty much unfair to the people that have helped me before and during this 3-years journey. I would anyway stick to a scientific approach and, for simplicity, divide people into two categories.

First of all, I want to thank my colleague, Xin Jin, who is working from the other side of the world, in Montreal. He will be in the same situation as myself in a few months (good luck if you happen to read my thesis beforehand). He has developed all the theoretical model of our system and has performed an awful amount of numerical simulations, in order to find the best working configuration and confirm the experimental results. Many thanks also to his supervisor, Prof. Luca Razzari, who encouraged all the project components with enlightening discussions.
I am grateful to “Gabri”, a former Post-Doc of our group who has helped me days and nights with our beautiful and entertaining Raman measurements: I believe that on the market does not exist a data storage device that could contain the tons of kB acquired on this setup. Moreover, I want to thank of course the Plasmonic group leader, Dr. Francesco De Angelis, for giving me the possibility to work in his facilities. Concerning the scientific contribution, last, but not least, my supervisor Dr. Andrea Toma, who has actively and constantly helped me throughout my PhD with discussions, suggestions and moral support.
A special mention to the colleagues of the Plasmon group and to the Lab technicians Eli, Marco Leo and Fabio (also Bosca) who conceded me to work in a “clean”, funny and cosy environment, thus allowing a profitable research to be pursued.

I am grateful to my family and especially to my parents: I would not have reached this milestone if it wasn’t for their support, both economical and emotional.
Many thanks to the IIT football team for the many triumphs at the “thief” San Biagio, in particular to Cava (for the defeats), Zambo, Cassa, Schip, Mura, Capa, Albi, Ponze and Bruchi (wherever he is now). Irreplaceable football mates.

As last, many many thanks to my girlfriend Chiara who has supported and sustained me for all these years. I bet she is now as expert as I am about the thesis topic, having listened to me complaining during the harsh moments.

Thanks for all your encouragement!